THE UNIVERSITY *of* EDINBURGH

This thesis has been submitted in fulfilment of the requirements for a postgraduate degree (e.g. PhD, MPhil, DClinPsychol) at the University of Edinburgh. Please note the following terms and conditions of use:

- This work is protected by copyright and other intellectual property rights, which are retained by the thesis author, unless otherwise stated.
- A copy can be downloaded for personal non-commercial research or study, without prior permission or charge.
- This thesis cannot be reproduced or quoted extensively from without first obtaining permission in writing from the author.
- The content must not be changed in any way or sold commercially in any format or medium without the formal permission of the author.
- When referring to this work, full bibliographic details including the author, title, awarding institution and date of the thesis must be given.

Quantitative Measurement of Intracellular Redox Potential Using SERS Nanosensors

THE UNIVERSITY *of* EDINBURGH

Jing Jiang

Thesis presented for the degree of Doctor of Philosophy,

The University of Edinburgh

April 2015

Supervisor: Dr. Colin J. Campbell

Declaration of Authorship

I declare that this thesis is my own composition; that the work which is described has been carried out by me, unless otherwise stated; and that it has not been submitted in any previous application for a higher degree.

This thesis describes the results of research carried out in the School of Chemistry, University of Edinburgh, under the supervision of Dr. Colin J. Campbell.

Jing Jiang

University of Edinburgh

April 2015

Signed: _____

Date: _____

Acknowledgements

Firstly I would like to thank my supervisor, Dr. Colin Campbell, one of the best people I've ever met. I was lucky enough to be offered a place in School of Chemistry, the University of Edinburgh and had the privilege to work with Colin. I wish to express my sincere thanks for his constant guidance and encouragement throughout the course of my research. His insight, enthusiasm and expertise in the field of chemistry and also biology have been a constant source of inspiration. From the Campbell group, I extend my thanks to every group member (Kate, Lauren, Anna-Maria, Sophie, Patrick, Vicky, Hannah, Lina and Sarah) for lending me so much help and making me feel not a foreigner. Particular appreciation goes to Kate, who offered a lot of assistance to me throughout all the past three years.

I want to specially thank my second supervisor, Prof. Mark Bradley and Dr. Jeff Walton for their outstanding input in the synthetic work. Mark was a nice man who shared his useful expertise in biochemistry. I am also grateful to Professor Eleanor Campbell and her group for allowing me to use their instruments and providing assistance. All the support staff in the School of Chemistry must be acknowledged for their wonderful work.

During the study, many amazing friends have impressed and influenced me surprisingly. A big "thank you" goes to Damion, Charlotte, Richard, Andrew Piper and Justin for creating such a wonderful and harmonious office. In addition, Menglu, Xun, Bo and Chun must also be mentioned for making my life so colourful.

Finally, I would like to thank my parents and all my family. Without their support, I couldn't manage to study abroad. This work is dedicated to them.

Abstract

Intracellular redox potential is a delicately balanced property in cells. It plays an important role in the regulation of cellular processes and dysfunction of the redox state is believed to get involved in initiation of many kinds of diseases. However, lack of suitable techniques for quantitatively monitoring the redox potential in cells with a wide range is a significant challenge.

My project aims to develop SERS nanosensors for measuring intracellular redox state quantitatively and applying them to quantify hypoxia, which is generally described by the cell having a reducing environment and defined as a form of "reductive stress". Four redox active probe molecules have been synthesised and characterised. Their Raman spectra all change as a function of local redox potential. Since these probe molecules can be assembled on gold nanoshells which are able to enhance the Raman Effect significantly, we can calculate the redox potential from simple optical SERS measurements.

Transmission Electron Microscopy was used to investigate the cellular delivery of nanosensors. TEM images confirmed that either single nanosensor or small aggregates can be taken up controllably by cells and translocated in the cytoplasm. The introduction of nanosensors was also found not to be toxic to the cells.

The nanosensor has been used to monitor the redox potential in resting cells as well as the redox changes when cells responded to pharmacologically induced hypoxia and oxidative stress. These measurements demonstrated that the SERS based nanosensor developed is able to monitor the intracellular redox change in a reversible, non-invasive way and respond to cellular hypoxia quantitatively.

Contents

List of Equations

List of Figures

List of Schemes

List of Tables

List of Acrynoms

AA Amino acid

ADP Adenosine diphosphate

AQ N-[2-({2-[(9,10-dioxo-9,10-dihydroanthracen-2-yl)formamido]ethyl}disulfanyl)ethyl]-9,10-dioxo-9,10-dihydroanthracene-2-carboxamide

ATP Adenosine triphosphate

BCA Bicinchoninic acid

BCECF, AM 2',7'-Bis-(2-Carboxyethyl)-5-(and-6)-Carboxyfluorescein, Acetoxymethyl Ester

BMES Bis(2-mecaptoethyl)sulfone

BSA Bovine serum albumin

CAT Catalase

CoA Acetyl coenzyme A

CS Calf serum

CV Cyclic voltammogram

DCFDA dichlorofluorescin diacetate

DCFH dichlorofluorescin

DCM Dichloromethane

DFT Density functional theory

DIC *N,N′*-Diisopropylcarbodiimide

DMEM Dulbecco's modified Eagle's medium

DMF Dimethylformamide

DMSO Dimethyl sulfoxide

DNA Deoxyribonucleic acid

DTNB 5,5'-dithio-bis (2-nitrobenzoic acid)

EDTA ethylenediaminetetraacetic

ELSD Evaporate light-scattering detector

EM Electromagnetic enhancement

ER Endoplasmic reticulum

ETC Electron transfer chain

GFP Green fluorescent protein

GNP Gold nanoparticles

GR Glutathione reductase

GSH Glutathione

GSSG Glutathione disulfide

HIF Hypoxia-inducible factors

HPLC High-performance liquid chromatography

HQ 2-Mercapto-benzene-1,4-diol

HRE Hypoxia response elements

HRP horseradish peroxidase

IR Infrared

IRP Intracellular redox potential

LDHA Lactate dehydrogenase A

LSP Localised surface plasmons

M2VP 1-methyl-2-vinyl-pyridinium trifluoromethane sulfonate

MTT 3-(4,5-dimethylthiazol-2-yl)-2,5-diphenyltetrazolium bromide

NADH Nicotinamide adenine dinucleotide

NADPH Nicotinamide adenine dinucleotide phosphate

NC Nanocolloids

NEM *N*-ethylmaleimide

NHE Normal hydrogen electrode

NNQ 2-chloro-3-{[2-({2-[(3-chloro-8-nitro-1,4-dioxo-1,4-dihydronaphthalen-2-yl)amino]ethyl}disulfanyl)ethyl]amino}-5-nitro-1,4-dihydronaphthalene-1,4-dione

NOS NO synthase

NQ ,8-diaza-4,5-dithia-1,8-di(2-chloro-[1,4]-naphthoquinone-3-yl)octane

NR Nanorods

NS Nanoshells

ODD Oxygen-dependent degradation domain

PBS Phosphate buffered saline

PDH Pyruvate dehydrogenase

PDK1 Pyruvate dehydrogenase kinase 1

PHD Prolyl hydroxylase domain

pVHL von Hippel-Lindau protein

RNS Reactive nitrogen species

roGFP Redox active green fluorescent protein

ROS Reactive oxygen species

SAQ N-(2-{[2-(9,10-dioxo-9,10-dihydroanthracene-2-sulfonamido)ethyl]disulfanyl}ethyl)-9,10-dioxo-9,10-dihydroanthracene-2-sulfonamide

SBTPP 4-sulfanylbutyltriphenylphosphanium bromide

SERS Surface enhance Raman spectroscopy

SNQ 6,7-dichloro-N-(2-{[2-(6,7-dichloro-5,8-dioxo-5,8-dihydronaphthalene-2-sulfonamido)ethyl]disulfanyl}ethyl)-5,8-dioxo-5,8-dihydronaphthalene-2-sulfonamide

SOD Superoxide dismutase

TCA Tricarboxylic acid

TEM Transmission electron spectroscopy

TLC Thin layer chromatography

TNB 5-thio-2-nitrobenzoic acid

TPP Triphenylphosphonium bromide

Trx Thioredoxin

TrxR Thioredoxin reductase

Chapter 1 Introduction

1.1 General Overview

Redox potential is a measure of how oxidative or how reductive an environment is. In cells, it is deliberately balanced and plays an important role in the progression of many biological progresses via modulation of the oxidation state of proteins.[1–7] Although redox state is crucial in regulating cellular processes and initiating diseases[8–10], the exact role of redox state change or regulation in each of these processes is not very well understood. As such, there is a strong need to develop a universal tool for quantifying the intracellular redox potential, which is supposed to include a series of technical features as described below. It should be:

i) not disruptive to cellular homeostasis

   Application of the measuring system should not induce either any perturbation to the cellular redox environment or any toxicity to cells.

ii) capable of recording redox potential in live cells in a reversible and quantitative way

   A quantitative technique is a big advantage in improving the understanding of intracellular redox potential and its role in cellular metabolism. Current qualitative techniques, such as oxidative stress or hypoxia assays, are only able to report on the redox state rather than indicate any details or any specific value of the redox potential in cells. Reversibility is another huge advantage that facilitates the study of intracellular redox response when exposed to various environment in real time.

iii) able to cover a wide window ranging from cellular hypoxia to oxidative stress.

The established technique in our group suffices to quantitatively record over a redox window covering cellular normoxia as well as supraphysiological oxidative stress. However, coverage of wider ranges is required especially the hypoxic range, which is widely reported to be linked with cancer.

The work described in this thesis covers the development of SERS-based nanosensors which are capable of quantifying intracellular redox potentials reversibly without disrupting cellular homeostasis. These nanosensors were also demonstrated to monitor the cellular hypoxia quantitatively and accurately.

1.2 The role of IRP in cells

1.2.1 The regulating role of IRP in healthy cells

Redox state is important in a number of cellular processes including: life cycle, gene expression and cell death.[4] The mammalian cell cycle has five distinct phases; quiescence (G0), gap phase 1 (G1), synthesis phase (S), gap phase 2 (G2), and mitosis (M), all of which are influenced by cellular redox status. Evidence suggests that the cell cycle is tightly associated with the redox change in cells[11-14].

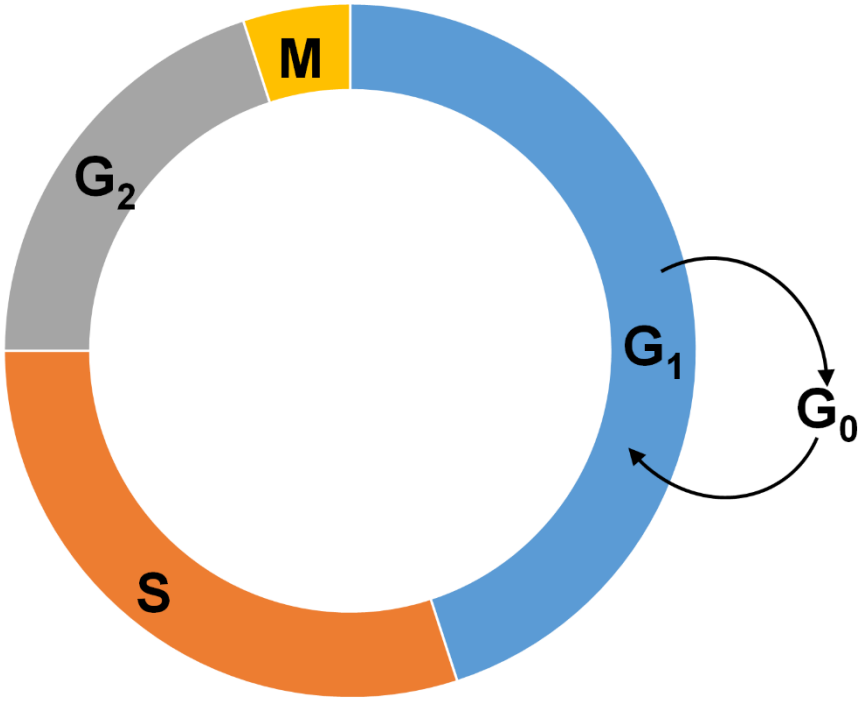

Figure 1.1 Scheme of the cell cycle: quiescence (G0), gap phase 1 (G1), synthesis phase (S), gap phase 2 (G2), and mitosis (M).

Figure 1.2 depicts the changing redox environment of a cell throughout different cellular biological stages. Schafer et al.[11] postulate that during proliferation IRP (determined by the ratio of GSH/GSSG) has the most negative value and the pathways driving proliferation are activated.[11] When IRP becomes more positive, cells tend to be more differentiative while proliferation diminishes. The more positive IRP becomes, the more differentiation switches are turned on until they reach a maximum where nearly all cells are differentiating. While cells undergo differentiation, proliferation switches are turned down and finally turned off. Cells that are not terminally differentiated could undergo proliferation with an appropriate signal and associated redox environment. If IRP becomes too positive, then death signals are activated and apoptosis is initiated. This mechanism provides for the orderly removal of cells that have lost their ability to control their redox environment

and therefore are not functioning normally. It should also coincide with signalling pathways to purposely dispose of unneeded cells. Extremely high values of IRP, resulting from severe oxidative stress, result in necrosis as a path to cell death.[11]

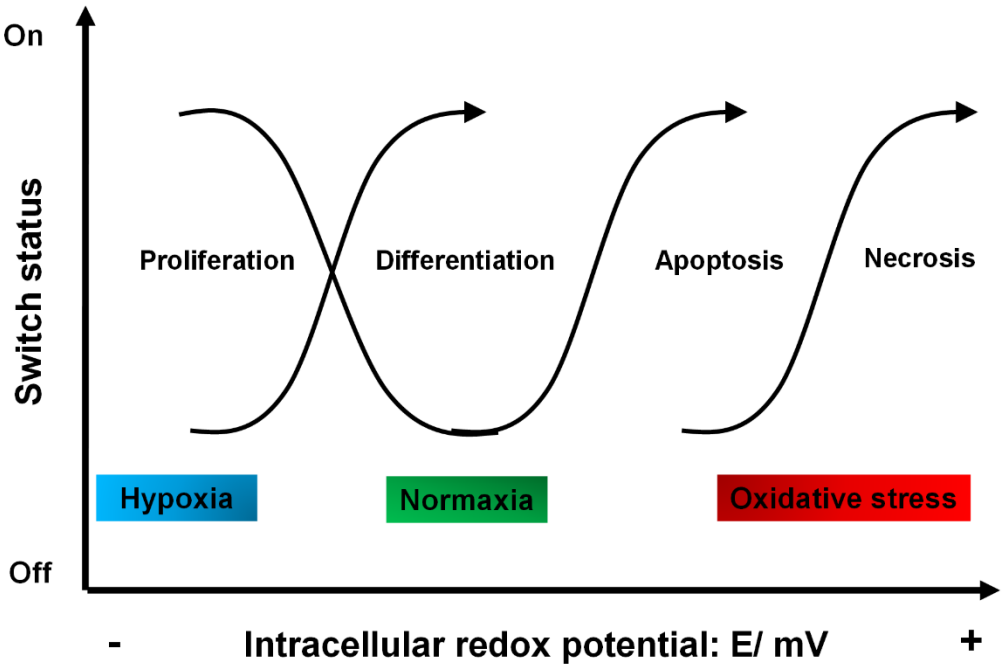

Figure 1.2 the IRP changes throughout the different cellular biological stages (adapted from Ref. *15*)

1.2.2 Dysregulation of IRP

Under normal physiological conditions, the intracellular redox homeostasis is deliberately maintained through the production of oxidants and their removal by antioxidant systems. Normally, redox homeostasis ensures that cells respond to stressors such as oxidative or reductive stress efficiently but when the balance is disturbed, oxidative stress or hypoxia occurs. Mounting evidence has demonstrated

that the IRP is dysregulated in a number of diseases including cardiovascular disorders, neurodegenerative diseases, and cancer. Here we focus on the importance of cellular reductive disorder, which has been considered to be an important factor in driving malignancy and resistance to therapy in tumours.[9,12–17]

Hypoxia is defined as a decrease in the oxygen supply to a level insufficient to maintain cellular function. At the cellular level, it is considered as a disruption of the intracellular redox homeostasis which directs the IRP towards a state that is more reducing than the normal physiological condition. When hypoxia occurs, cells trigger a multitude of adaptive responses in order to survive and maintain oxygen homeostasis.[15,18–21] The essential step for these responses is activation and stabilisation of the hypoxia-inducible factors (HIFs), which are a group of transcription factors. The HIF family comprises three members, HIF-1, HIF-2 and HIF-3, but only HIF-1 is ubiquitously expressed in all kinds of cells. HIF-1 is tightly regulated. Under normoxia, the α subunit of HIF-1 (HIF-1α) is rapidly hydroxylated by the prolyl hydroxylase domain (PHD) at two proline residues located in the oxygen-dependent degradation domain (ODD). Hydroxylated proline serves as a binding site for the von Hippel-Lindau protein (pVHL). The pVHL tagged HIF-1α is targeted for proteasomal degradation. Thus the transcriptional activity of HIF-1 is repressed. However, when cells are exposed to hypoxia, PHD become inactive, resulting in the stabilisation of HIF-1α. The stabilised HIF-1α can bind to the β subunit to form the transcriptionally active HIF-1 complex. The heterodimer is then translocated to the nucleus and binds to DNA at hypoxia response elements (HRE).[22–25]

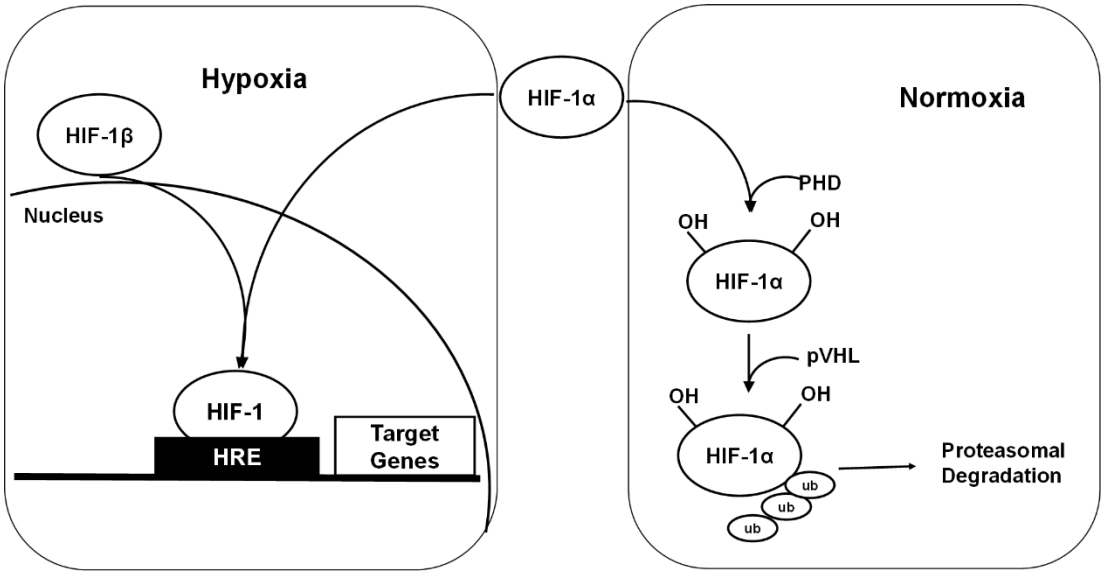

Figure 1.3 Scheme of HIF-1 activated by Hypoxia.

Once these HIF-regulated gene expressions are activated, a series of biological process are triggered to promote cellular living in hypoxic conditions. Cellular respiration is shifted to glycolysis under hypoxia, which results in the suppression of cellular respiratory rate as well as the nicotinamide adenine dinucleotide (NADH) supply to mitochondria.[15,26] Compared to oxidative phosphorylation, glycolysis leads to higher generation (Figure 1.4) and less consumption of NAD(P)H as mitochondrial function is decreased. Hypoxia also diminishes the activity of the electron transport chain (ETC) and cellular ATP utilisation.[21,27,28] As a consequence of these metabolic shifts, it is expected to see the IRP becoming more reducing affected by both increasing NAD(P)H and decreasing ROS under hypoxia. This hypothesis has been confirmed by various groups that showed lower GSSG levels, higher GSH levels, a higher GSH/GSSG ratio and less hydrogen peroxide generation under hypoxia vs. normoxia.[29–31] However, controversial results have also been reported that cellular ROS were increased when cells were exposed to hypoxia.[15,29,32,33] Considering that IRP is a global property regulated by various redox

couples and enzymes, it is not sufficient to report on the cellular redox state by only taking into account a single redox regulator, such as ROS, or even a limited number of redox substances.

Over the last decade, numerous studies have indicated that micro-environmental hypoxia is a hallmark of tumour progression.[34–37] Tumour vessels are structurally and functionally abnormal, which results in a severely insufficient oxygen supply to tumour tissues. Therefore, hypoxic areas are present in even highly vascularised cancers. HIF is also overexpressed and stabilised at a high level in common cancer cells. The activated HIF pathway enhances neovascularisation, which supplies sufficient amounts of oxygen and nutrients to cancer cells for propagation and metastasis.[38,39] Moreover, by induction of glycolytic enzymes involved in glucose uptake, HIF also allows tumour cells to maintain energy production by glycolysis and survive through a limited oxygen supply.[13] Other than playing a critical role in the tumour progression, hypoxia is also an important indicator of therapeutic response to radiation and chemotherapy. As radiotherapy requires oxidising to induce DNA damage and kill cells, tumour tissues, with a reducing redox environment, are resistant to radiation treatment. Furthermore, hypoxia can also decrease the effectiveness of chemotherapy.[40] In terms of the great importance of cellular hypoxia, it is strongly necessary to build a comprehensive, quantitative, real-time measuring platform for probing the IRP in cellular hypoxia. A deep and thorough understanding of IRP in hypoxic cells would facilitate the research of unravelling cancer mechanism as well as the drug design. For example, in terms of the IRP difference between hypoxic and normoxic cells, a nontoxic prodrug, which is able to be converted to a toxic drug in reducing environment through a reduction reaction, can be constructed to target and only work in the hypoxic tumour tissues.[12]

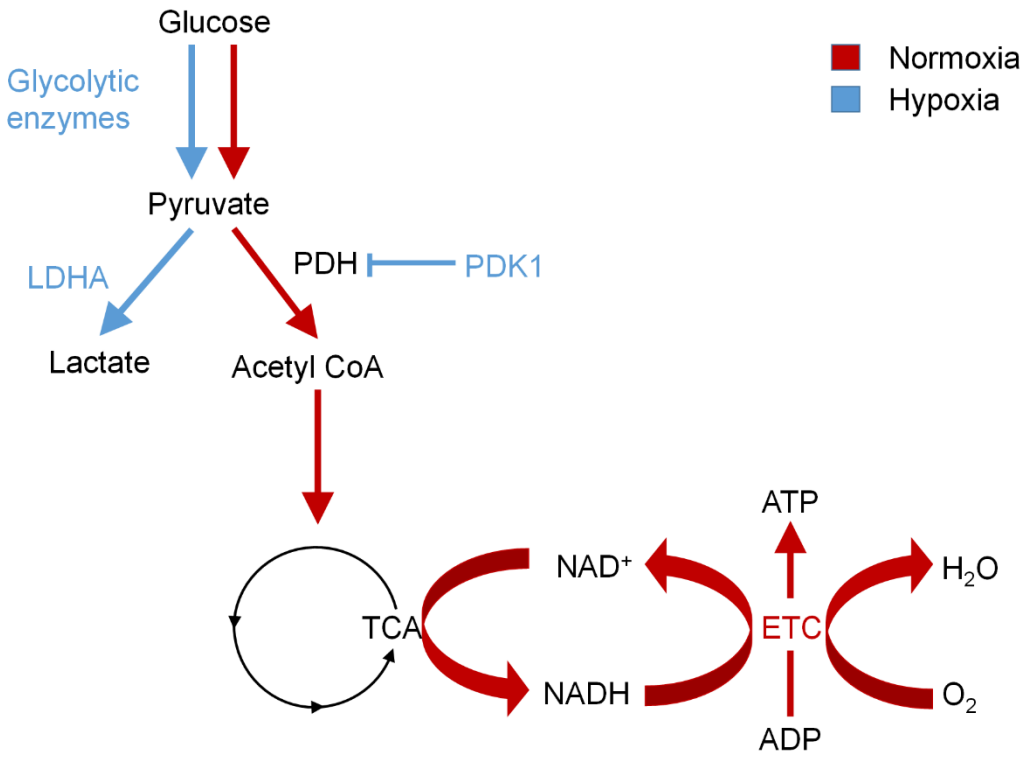

Figure 1.4 Regulation of cellular respiration from oxidative phosphorylation to glycolysis in response to hypoxia. Through glycolytic enzymes, glucose is converted to pyruvate. Under normoxia, pyruvate dehydrogenase (PDH) transfers pyruvate to acetyl coenzyme A (CoA). Via mitochondrial tricarboxylic acid (TCA) cycle and ETC, acetyl CoA is oxidised and these electrons are transferred to oxygen to form water. Alongside this process, ATP is also generated. While under hypoxia, PDH is inactivated by pyruvate dehydrogenase kinase 1 (PDK1) and pyruvate is only converted to lactate by lactate dehydrogenase A (LDHA). (adapted from Ref. *41*)

1.3 Regulation of Intracellular Redox Potential

The redox potential, or more accurately the reduction potential, of a compound refers to its tendency to acquire electrons and be hereby reduced. By knowing the concentration of the reduced and oxidised species of a given redox couple, their redox potential can be determined by the famous Nernst Equation (Equation 1.1).

$$E = E^{\theta} + \frac{RT}{nF} \ln \frac{[Ox]}{[Red]}$$

Equation 1.1: Nernst Equation. E = potential (V), E^{θ} = standard reduction potential (V), R = universal gas constant, T = temperature (K), F = Faraday's constant, n = number of electrons involved in the reaction, [Ox] = concentration of oxidised species, [Red] = concentration of reduced species.

Biological systems are filled with molecules that are paired in oxidation-reduction reactions. Each such pair forms a specific redox couple at a concentration ratio that determines its own redox potential. If the whole intracellular redox state were in equilibrium, the concentrations of each redox couple would reach a balanced ratio which would cause every couple to have the equilibrating redox potential. However, the ideal equilibrium is not reached in cells and weak link among different redox couples results in the establishment of different redox states of couples coexisting in the cell. As a consequence, only measuring the ratio or the redox potential of a single redox couple doesn't suffice to reflect the overall redox environment of the cell.[41] The intracellular redox potential is a balanced property which is delicately regulated by the production of oxidants, including reactive oxygen species (ROS) and reactive

nitrogen species (RNS), and their removal by antioxidant system involving glutathione (GSH), thioredoxin, NADPH and some antioxidant enzymes.

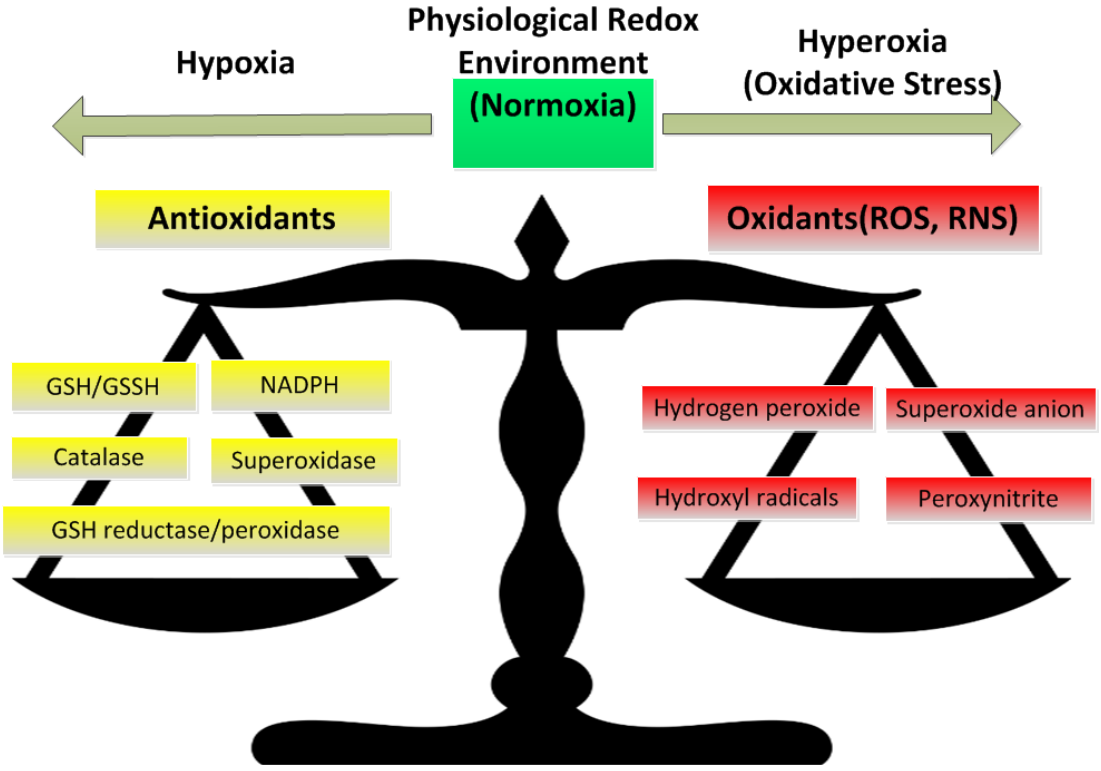

Figure 1.5 The balanced regulation of IRP by oxidants and detoxifying antioxidants.

1.3.1 ROS and RNS

Reactive oxygen species (ROS) are generally referred to as partially reduced metabolites of O_2 due to their higher reactivities relative to molecular O_2, including superoxide anion ($O_2^{-}\cdot$), hydrogen peroxide (H_2O_2) and the hydroxyl radical ($OH\cdot$).[5,11]

Cellular production of ROS mainly results from electron-transfer reactions in the mitochondria. The mitochondrial ETC is not 100% efficient and ~1-2% of total O_2

consumption accounts for the generation of ROS.[42] A single-electron reduction of O_2 results in the formation of $O_2^-\cdot$, which is considered one of the most hazardous oxidants.[43] In aqueous solution, $O_2^-\cdot$ is short-lived based on the rapid dismutation of $O_2^-\cdot$ to H_2O_2 with an overall reaction rate constant of $5 \times 10^5\ M^{-1} \cdot s^{-1}$ at pH 7.0. Superoxide dismutase (SOD) can speed up this reaction almost 10^4-fold.[43] Due to high concentrations of intramitochondrial SOD[44], $O_2^-\cdot$ is maintained at very low steady-state level which can protect the mitochondrial membrane from damage by oxidation.[5,45] Unlike $O_2^-\cdot$, H_2O_2 is not a free radical and is much more stable in aqueous solution. It is also able to diffuse across biological membranes whilst $O_2^-\cdot$ is membrane impermeant. Thus H_2O_2 can escape from the mitochondria into the cytoplasm.[45] With a relatively high concentration of 10^{-7} M and a half-life of 10^{-5} s, H_2O_2 is by far the most abundant and stable ROS in the cellular environment.[5] Aided by catalase (CAT), H_2O_2 can be decomposed to water and molecular oxygen. However, in the presence of transition metals such as iron or copper, H_2O_2 can be converted to the indiscriminately reactive and toxic hydroxyl radical ($OH\cdot$) by Fenton chemistry.[46]

Other than the mitochondria, the endoplasmic reticulum (ER) and peroxisomes contribute to the production of cellular ROS, especially H_2O_2.[47] Autooxidation of small molecules such as dopamine, epinephrine, flavins and hydroquinones can also be an important source of intracellular ROS.[48] In addition, NADPH oxidase also contributes to the production of intracellular ROS.[49]

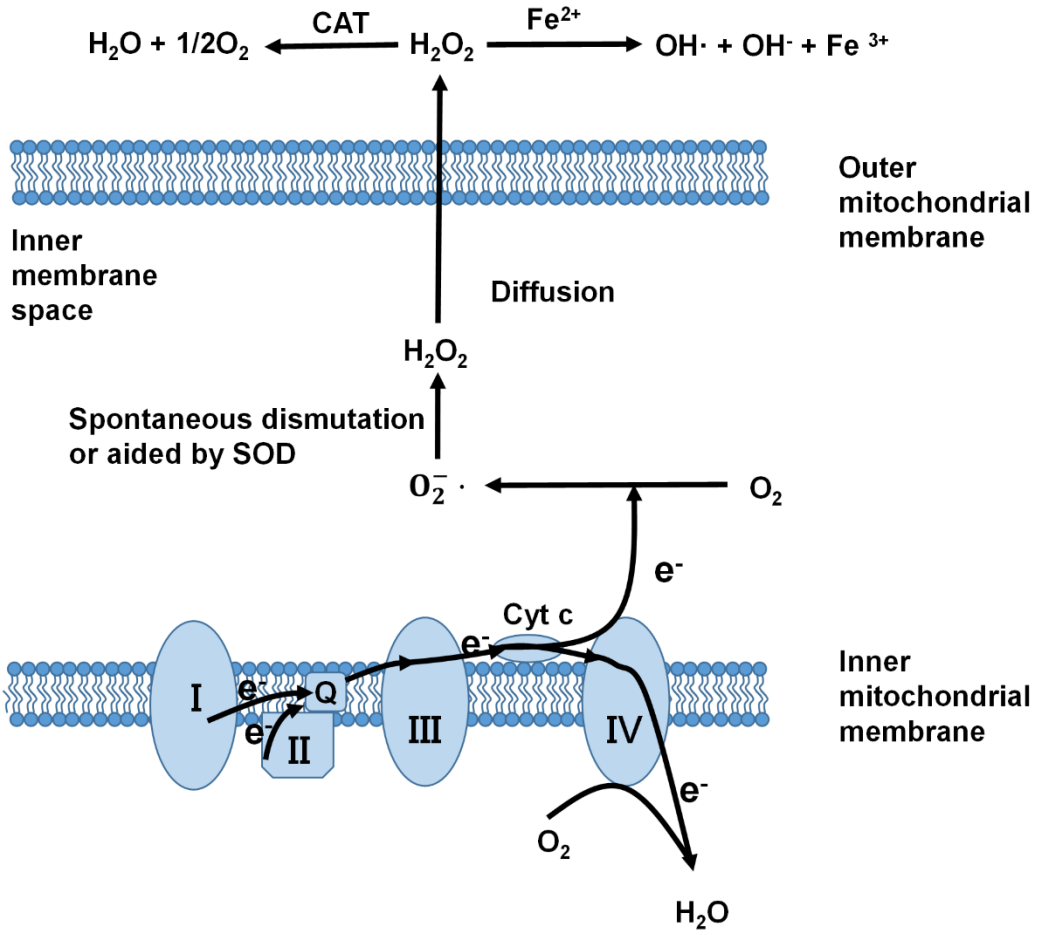

Figure 1.6 Generation of ROS from the mitochondria. ETC occurs on the inner mitochondrial membrane. Electron leakage can cause the partial reduction of O_2 to form $O_2^-\cdot$, which then can be converted to H_2O_2 via spontaneous dismutation or with the help of SOD. H_2O_2 is capable of translocating to the cytoplasm and is converted to water and oxygen or to highly reactive OH ·through Fenton chemistry.

RNS are another group of intracellular oxidants including various nitric oxide-derived compounds, such as the nitroxyl anion (NO^-), nitric oxide (NO ·), the nitrosonium cation (NO^+) and peroxynitrite ($OONO^-$).[50] NO · is the major RNS species produced in cells by NO synthases (NOS) from L-arginine and oxygen. It is also a ubiquitous intracellular signalling molecule able to regulate neural and cardiovascular activities. However, as a result of its high reactivity with $O_2^-\cdot$, NO ·and $O_2^-\cdot$ can combine by an enzyme-independent mechanism to form $OONO^-$,

a deleterious oxidant that reacts with most biological molecules, causing cell damage.[50]

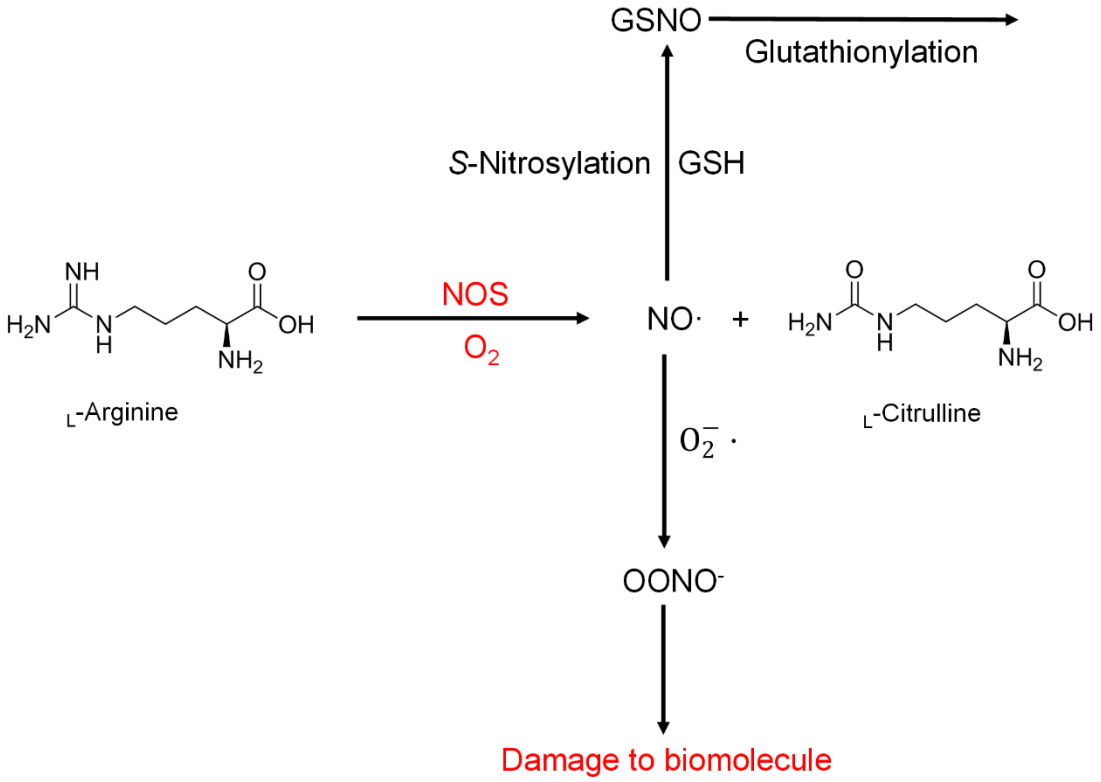

Figure 1.7 NO · is synthesised from L-Arginine catalysed by NOS. NO · can react reversibly with GSH to form GSNO which mediates posttranslational modifications as well as serves to store, transport and deliver NO ·. NO · can also be converted to $OONO^-$, which is harmful to cellular biomolecules.

ROS have gained increasing attention due to their signalling role in cellular metabolism. The signalling mechanism can be generally divided into two actions: 1) altering the intracellular redox state and 2) modifying proteins by oxidation. The role of ROS in altering the IRP is easy to understand since ROS are a group of oxidants which can react with reductants, regulating the redox environment towards the oxidising direction. Therefore, in this section we will focus on the oxidative

modification of proteins by ROS.

Generally, protein structure and its function can be adjusted by ROS through the modification of critical amino acid residues, induction of protein dimerisation, and interaction with Fe-S moieties or other metal complexes (for examples see Figure 1.8).

1）Oxidative modification of critical amino acids

Cysteine residues are the best-described amino acid to be involved in the ROS signalling pathway. The sulfhydryl group (-SH) of a cysteine residue can be oxidised by ROS to form sulfenic acid (-SOH), sulfinic acid ($-SO_2H$), sulfonic acid ($-SO_3H$) or even S-glutathionylated (-SSG) derivatives. If there are two or more cysteine residues in the same protein molecule, intramolecular sulfide bond(s) can be also formed. Such structural changes can lead to the alteration of the function of an enzyme or the activity of a transcription factor.[51,52]

2）Dimerisation of proteins

Intermolecular sulfide bonds can be also formed as bridges by the oxidation of cysteine residues from two identical or different proteins. Tyrosine residues have also been found to be able to be involved in the dimerisation or even polymerisation of proteins.[53,54]

3）Oxidation of metal complexes

Metalloenzymes are very common in biological systems and serve as important targets of ROS. Iron regulatory proteins are very sensitive to oxidation.[55]

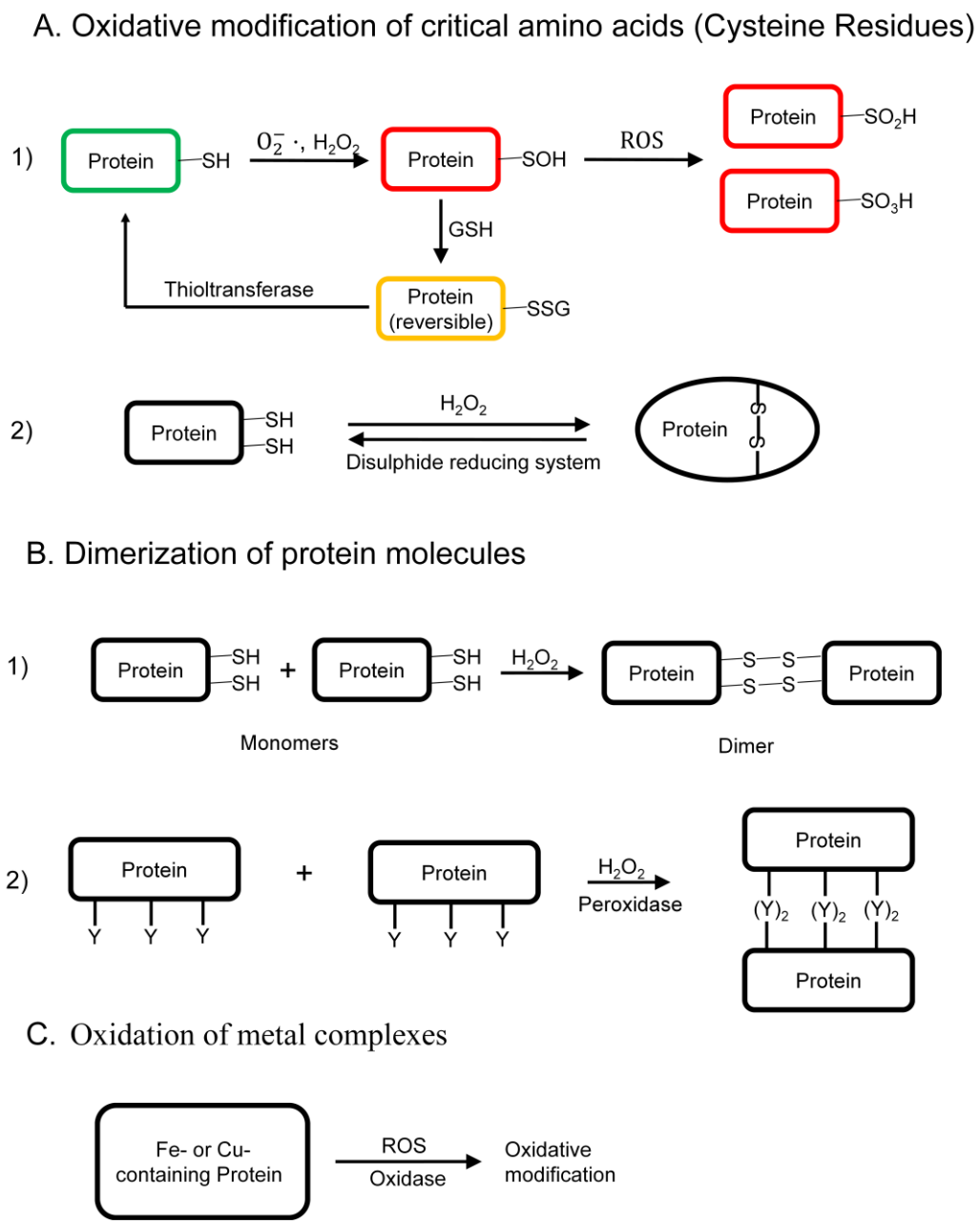

Figure 1.8 Oxidative modifications of proteins by ROS. A1): the sulfhydryl group (-SH) of protein molecules can be oxidised by H_2O_2 or $O_2^- \cdot$ to generate a series of oxidised derivatives. Through S-glutathionylation and aided by thioltransferase, the modified sulfenic derivative can be converted back to the active protein; A2) formation of intramolecular sulfides by H_2O_2 can adjust or activate the function of proteins; B1) Intermolecular sulfide bridge can be formed to yield the dimerisation of proteins; B2) H_2O_2 or peroxidase-catalysed

formation of dityrosine can also provide a way to dimerise or even polymerise proteins; C transitional metal-containing proteins are commonly ROS targets.

ROS play an important role in the intracellular signalling pathway, however, if the production of ROS overbalances the scavenging ability of antioxidant systems or a disorder occurs in the antioxidant systems, oxidative stress then happens. The ROS produced during oxidative stress can cause severe damage to biomolecules, such as lipids, proteins and DNA. Extremely oxidative stress could lead to necrosis.

1.3.2 Antioxidant System

To help eliminate the potentially harmful effect of ROS and also equilibrate the intracellular redox environment, cells have developed sophisticated antioxidant defence systems. It is very important to maintain the normal and proper cellular functions and metabolism.

1.3.2.1 Glutathione (GSH)

Glutathione (L-γ-glutamyl-L-cysteinyl-glycine) is a tripeptide, a non-protein sulfhydryl molecule present in both prokaryotes and eukaryotes and is the principal non-protein thiol component of the antioxidant defence system in living cells.[56] It is naturally synthesised from L-cysteine, L-glutamic acid and glycine in the body. It is mostly found in its reduced form and considered the major thiol "redox buffer", with an overall cytosolic concentration ranging from 1 – 11 mM.[11]

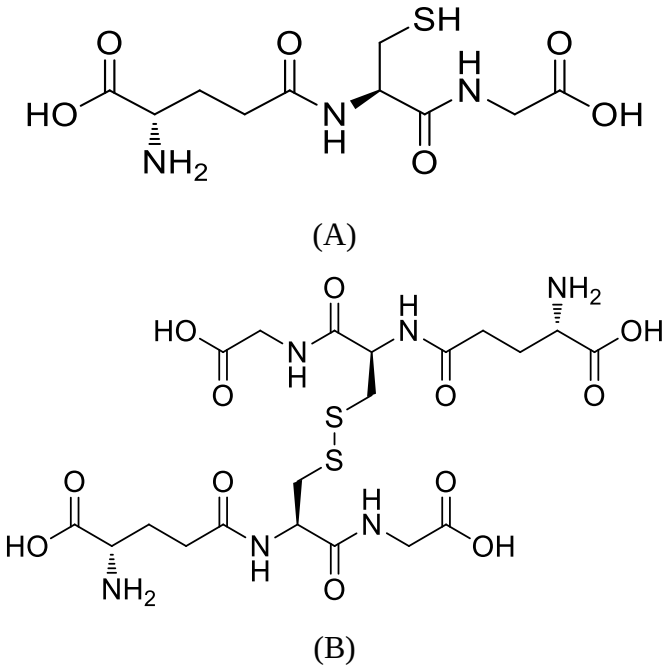

(A)

(B)

Figure 1.9 Structures of GSH (A) and GSSG (B)

The major role of GSH is to neutralise the ROS generated and protect cells from their damaging effects. As an electron donor, GSH reacts spontaneously with a number of ROS as well as other cytotoxic products including OH · and ONOO-. However, hydroperoxide compounds can be only eliminated through enzymatic catalysis by glutathione peroxidase. Glutathione also modifies protein sulfhydryl groups by a number of reactions including reduction of protein sulfenic acids, formation of protein mixed sulfides and their subsequent reduction, thus regulating cellular metabolism.[57] Other than scavenging ROS, GSH also assists in the removal of harmful toxins such as electrophilic compounds, mediated by glutathione S-transferase. The oxidised form of the redox couple, GSSG, can be reduced back to GSH by glutathione reductase, with NADPH as the reductant, and also by the thioredoxin or glutaredoxin systems.[43,48,58,59]

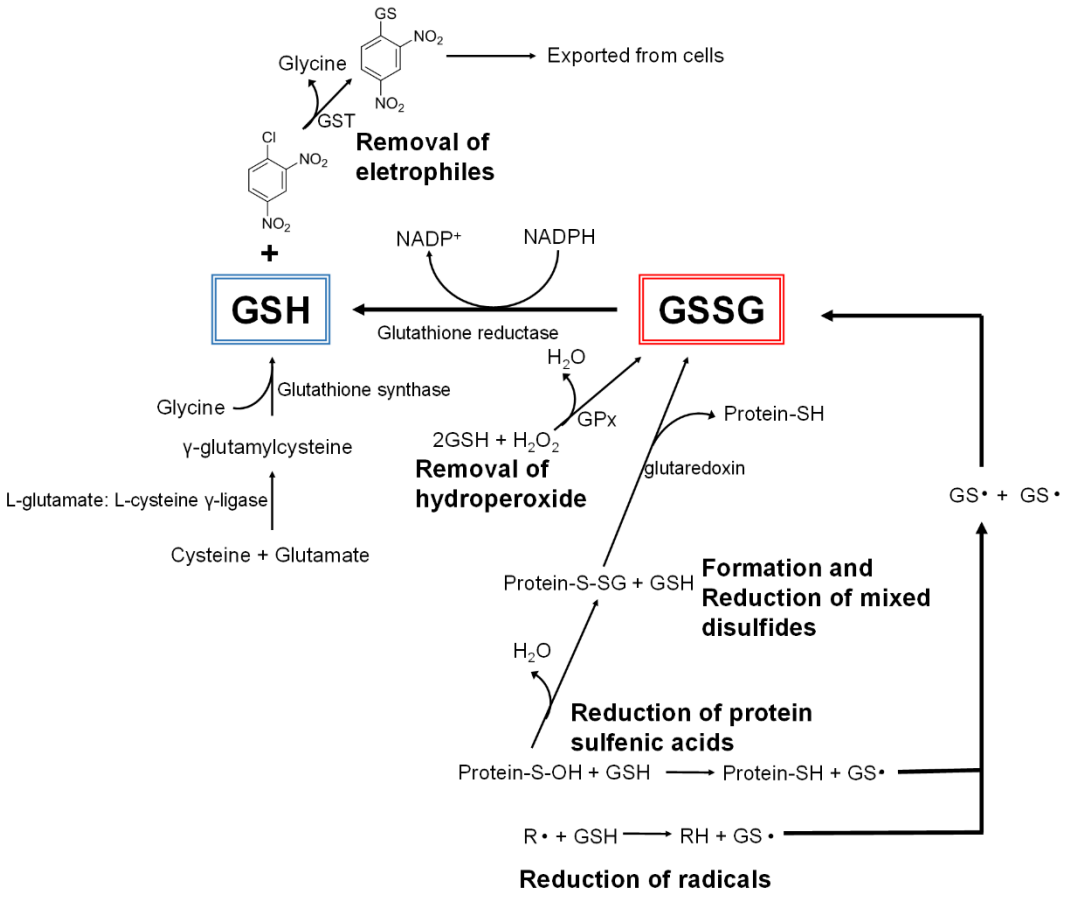

Figure 1.10 Synthesis and metabolism of GSH in cells. (adapted from Ref. *57*)

1.3.2.2 Thioredoxin

Thioredoxin is a class of small proteins which are ubiquitous in all organisms. Thioredoxin serves as a general oxidoreductase to maintain the intracellular protein sulfides mostly reduced by cysteine thiol-disulfide exchange reaction.[11] The dithiols of thioredoxin acts as the hydrogen donor as well as the electron donor for ribonucleotide reductase, which plays a key role in the DNA synthesis.[60] Thioredoxin also enables the refolding of sulfide-containing proteins and regulates the activity of some transcription factors.[60,61]

Unlike GSH which forms an intermolecular sulfide when oxidised, an intra-molecular sulfide bond is formed in thioredoxin molecule. This sulfide bond can be reduced back to a thiol aided by the thioredoxin reductase (TrxR) with NADPH as the electron donor.[62,63]

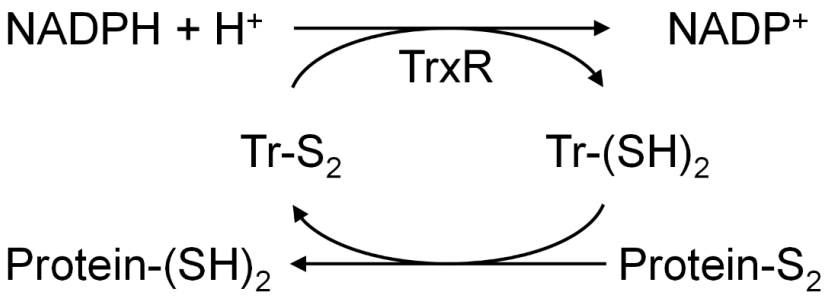

Figure 1.11 Scheme of oxidoreductase activities of the thioredoxin system. The figure schematically depicts the reduction of the active site disulfide in oxidised thioredoxin, Trx-S_2, to a dithiol in reduced thioredoxin, Trx-$(SH)_2$, by thioredoxin reductase (TrxR) and NADPH. Trx-$(SH)_2$ reduces protein disulfides through its general oxidoreductase activity, generating Trx-S_2.

1.3.2.3 Nicotinamide adenine dinucleotide phosphate ($NADP^+$)

NADPH, the reduced form of $NADP^+$, is the major electron source for reductive biosyntheisis.[11] It is mainly generated in the oxidative phase of the pentose phosphate pathway. NADPH can provide two electrons when being oxidised to $NADP^+$.[60]As stated above, as the ultimate reducing equivalents, NADPH allows the reduction of GSSG and Trx-S_2, maintaining the redox balance in cells.[60] Additionally, NADPH is also used for anabolic pathways and provides free radicals in immune cells to remove pathogens in a process named the respiratory burst by NADPH oxidases.[64]

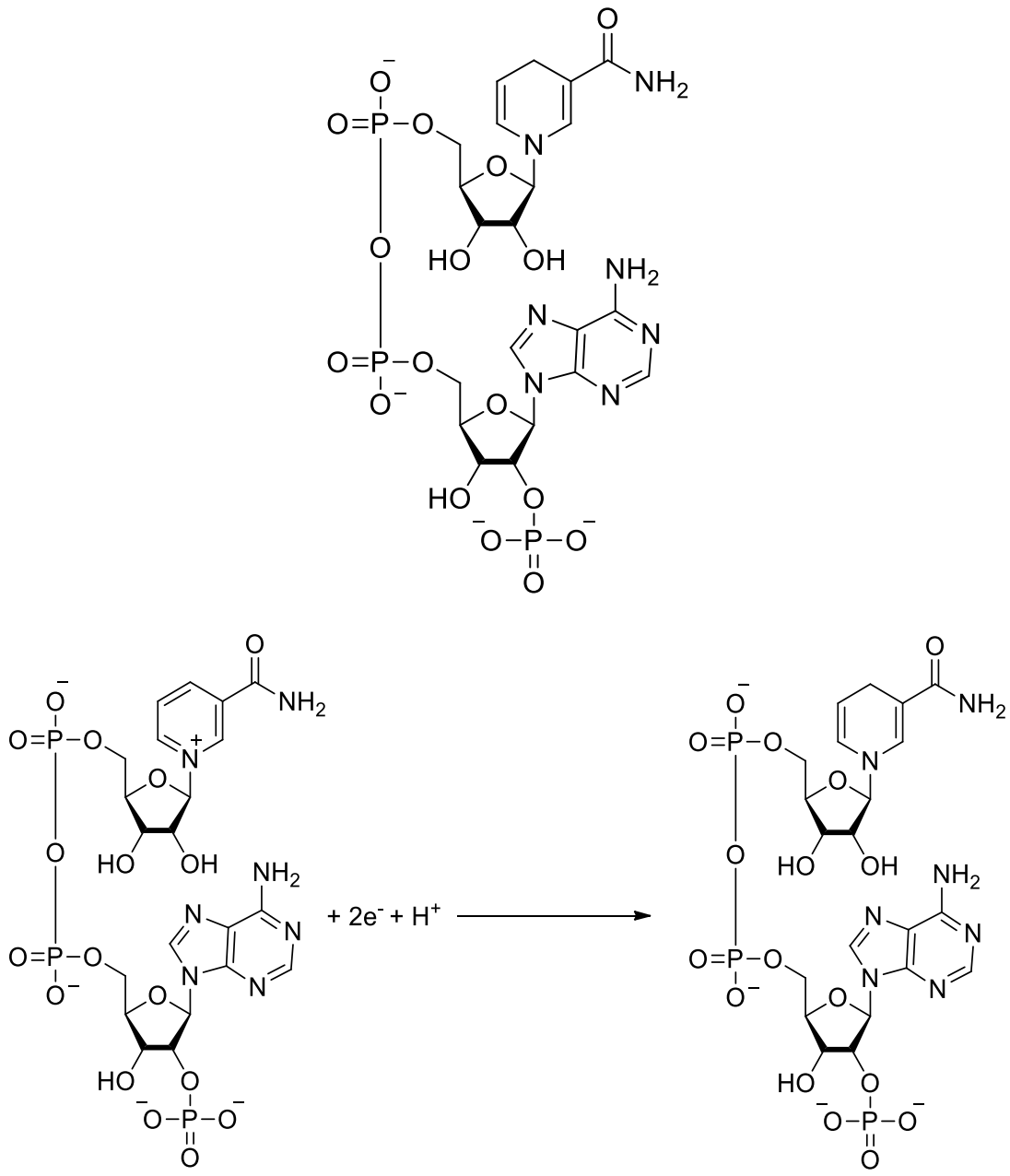

Figure 1.12 Structure of NADPH and its reduction from $NADP^+$

1.3.2.4 Enzymatic antioxidants

In addition to the redox active molecules, enzymes are also key players in regulating the intracellular redox state. Enzymes are proteins that catalyse biological processes.

In cells, enzymes can clear ROS by catalysis or cooperate with antioxidant species like GSH and NADPH, as well as thioredoxin, to protect cells from the harmful effects of ROS.[11]

Superoxide is detoxified by superoxide dismutase (SOD) to generate H_2O_2 and molecular oxygen (Figure 1.13). Three isomers have been identified, cytosolic Cu/Zn SOD (SOD1), mitochondrial Mn-SOD (SOD2) and extracellular SOD (SOD3), which play their roles in different compartments.[44]

$$2O_2^- + 2H^+ \xrightarrow{SOD} H_2O_2 + O_2$$

Figure 1.13 Dismutation of O_2^- by SOD

The heme-containing metalloenzyme catalase (CAT) is expressed in peroxisomes, the nucleus, mitochondria and cytoplasm and is responsible for decomposing H_2O_2 into water and oxygen (Figure 1.14).[1]

$$2H_2O_2 \xrightarrow{CAT} 2H_2O + O_2$$

Figure 1.14 Dismutation of H_2O_2 by CAT

Similar to CAT, the selenoprotein glutathione peroxidase found both intra- and extra-cellularly, catalyses the conversion of H_2O_2 into water using the thiol-glutathione. Glutathione peroxidase also has a high affinity for lipid peroxides, detoxifying them to their equivalent alcohols. Besides the glutathione system,

thioredoxin peroxidases are also key regulators of cellular thiol/disulfide level. Their detoxification of H_2O_2 plays important roles in preventing lipid peroxide formation and regulating the cellular redox status.[1,65]

1.3.2.5 Other antioxidants

Vitamin C (ascorbate) is a direct antioxidant. Ascorbic acid shows an ability to decrease endogenous oxidative damage to DNA.[66] The lipoproteins modified by the dehydroascorbate also shows an increase in resistance to metal ion-induced oxidation. However, ascorbate can be pro-oxidative in the presence of transition metals, by converting ferric ions to ferrous ions, thereby catalysing the Fenton reaction.[67]

Vitamin E is another kind of natural antioxidant which can inhibit NADPH oxidase-mediated generation of superoxide anion. Since Vitamin E is lipid-soluble and thus able to protect membranes against oxidative stress.[68]

1.4 Current techniques

Currently, there are a few tools which can be used to detect IRP, including the GSH-recycling assay[69], redox-active green fluorescent proteins (roGFP)[70,71] and oxidative stress and hypoxia markers[72–74]. While each of them has its merits, none of them is able to meet the requirements as an ideal IRP-measuring platform.

1.4.1 GSH-Recycling Assay

In 1969, a quantitative enzymatic assay of cellular glutathione was developed by Tietze[69]. The assay method involves two major components: the GSH assay and the GSSG assay.

GSH assay: The assay is based on the reaction of GSH with DTNB (5,5'-dithio-bis (2-nitrobenzoic acid)) (also known as Ellman's reagent) that produces the TNB chromophore, which has a maximal absorbance at 412 nm, and oxidised glutathione–TNB adduct (GS–TNB). The rate of formation of TNB, measured at 412 nm, is proportional to the concentration of GSH. The concentration of an unknown sample is generally obtained from the calibration curve generated from several standards of GSH.

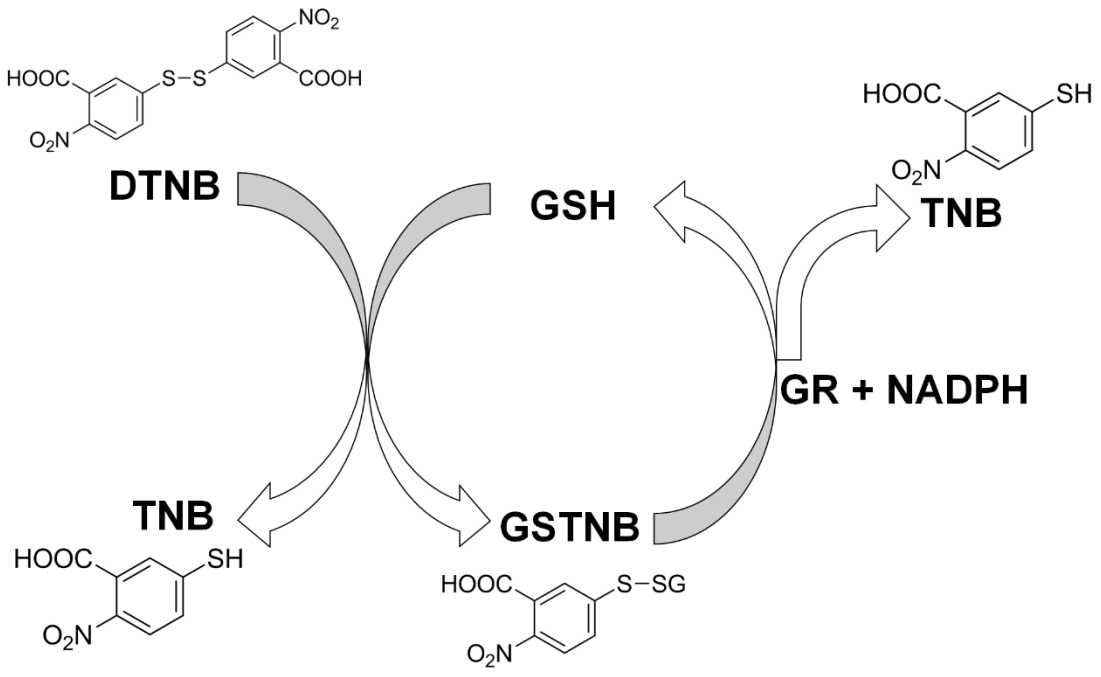

Figure 1.15 Schematic of GSH assay. Thiol groups of GSH, including those formed by the reduction of GSSG, can react with DTNB to produce GSTNB and TNB. The resultant

GSTNB is then reduced back to GSH and TNB by GR in the presence of NADPH. TNB has a maximal absorbance at 412 nm and the formation rate of TNB is proportional to the sample GSH concentration.

GSSG assay: The GSSG concentration is much less than that of GSH in cells, and GSH also tends to form GSSG by oxidation. Therefore, GSSG must be measured immediately to avoid oxidation from GSH to GSSH, which could alter the ratio of GSH to GSSG. Initially, *N*-ethylmaleimide (NEM) was used by Tietze as a marking agent for GSH. However, the NEM could potentially inhibit GR and it is essential to remove excess NEM before subsequent processing. For this reason, NEM has now been replaced with 1-methyl-2-vinyl-pyridinium trifluoromethane sulfonate (M2VP), or 1-methyl-2-vinyl-pyridinium trifluoromethane sulfonate (M4VP) as derivatisation agents, which makes this assay quicker and more accurate.[75]

Once the total concentrations of both GSH and GSSG are determined, the concentrations of cellular GSH and GSSG, respectively, can be obtained. By inserting these two concentrations into the Nernst equation, the IRP can be estimated.

The GSH-recycling assay is still currently widely used in terms of its ease to carry out. However, it has some distinctive drawbacks. First of all, the assay method requires the lysis of sample cells. It cannot be used for recording the redox potential in live cells. Secondly, as thousands of cells are harvested for the quantification of GSH and GSSG, it only represents the average redox state of the cell population and it is impossible to detect the redox environment in a single cell. Moreover, the assay is also prone to inaccuracy caused by the oxidation of GSH to GSSG by air.[75]

1.4.2 Redox Active Green Fluorescent Proteins (roGFP)

The green fluorescent protein (GFP) is a protein composed of 238 amino acid residues that exhibits bright green fluorescence when excited by light in the blue to ultraviolet range. It was first isolated from the jellyfish *Aequorea Victoria* and has been widely utilised in cell biology and fluorescence imaging.[76]

In 2004, redox active GFPs were reported that allow real-time visualisation of the intracellular oxidation state.[70] The roGFPs are modified with two surface-exposed cysteines, which are sensitive to the redox environment. Formation of the sulfide between the cysteine residues leads to the increase of the excitation spectrum peak near 400nm at the expense of the peak near 490 nm.[71]

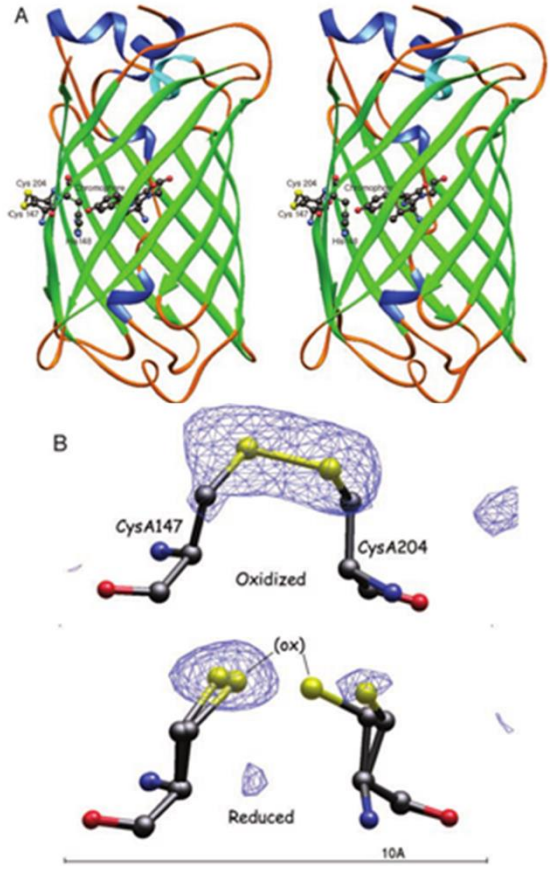

Figure 1.16 (A) Crystal structures of the β-barrell secondary structure of roGFP (B) the formation of the disulfide bond between the two cysteine residues. (Figure from *Ref. 72*)

The ratio of the fluorescence intensity of excitation at around 400 nm and 490 nm reflects the ratio of the oxidised species of the engineered cysteine residues. Thus this ratio can be inserted into the Nernst equation to obtain the redox potential values.

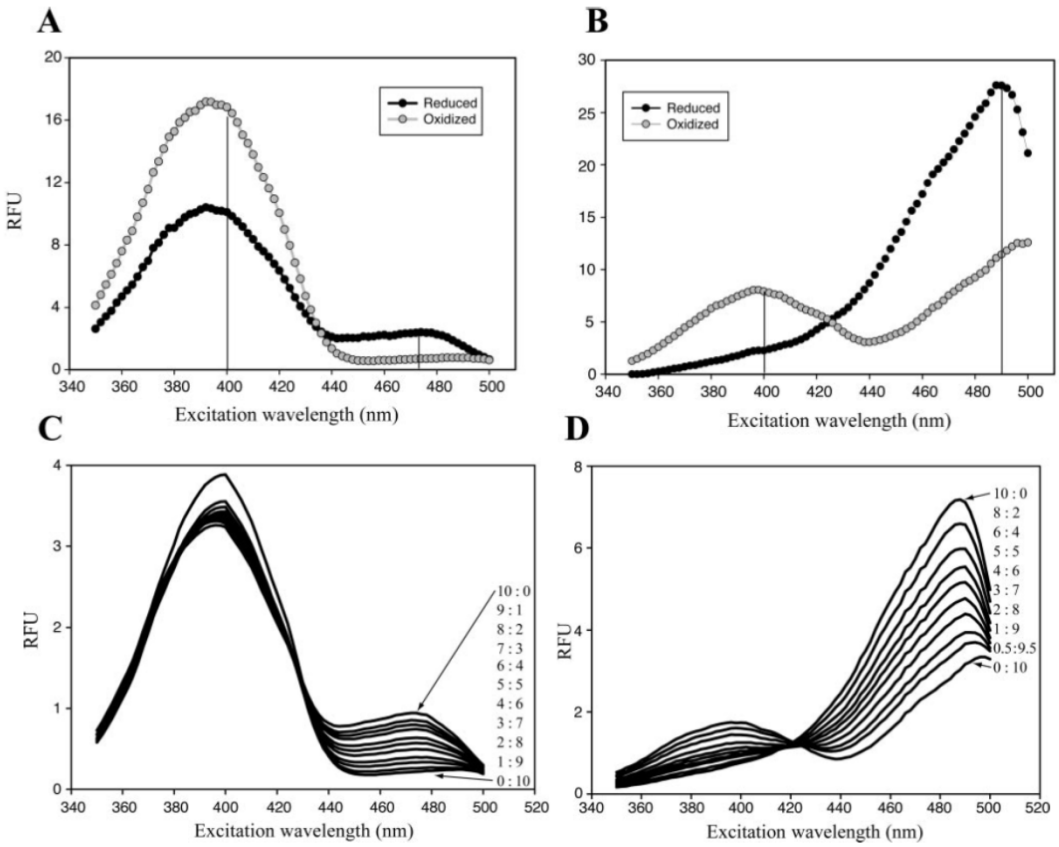

Figure 1.17 (A) Excitation spectra of fully oxidised and reduced roGFP1, (B) Excitation spectra of fully oxidised and reduced roGFP2. Emission was recorded at 515 nm, (C) Titration of roGFP1 (1 µM) with dihydrolipoate + lipoate buffers (total 10 mM), (D) Titration of roGFP2 (1 µM) with reduced + oxidised Bis(2-mecaptoethyl)sulfone (BMES) (total 10 mM) (Figure from *Ref. 71*).

roGFPs are currently considered the gold standard tool to monitor IRP. Because roGFPs are genetically encoded, the measurements do not require cell lysis and can be carried out reversibly and in real time. However, they still have some distinct limitations. roGFPs are only linked to the GSH/GSSG redox couple. Although GSH/GSSG is the dominant redox system in cells, many other redox-regulating compounds also account for the overall IRP as explained previously. What is more, these various redox couples in the cell are not in equilibrium with each other,[56]

therefore measurements made by roGFPs are not able to reflect the whole intracellular redox environment. In addition, in terms of the difficulty to modify protein structures, protein engineering offers little scope for expanding the measuring window to wider ranges.

1.4.3 Fluorescent Probes of Oxidative Stress and Hypoxia

In addition to those techniques trying to quantify the redox state in cells, many qualitative probes have also been developed. Among those probes, dichlorofluorescin diacetate (DCFDA) is the most popular used to detect intracellular peroxides. DCFDA can enter cells and accumulate in the cytosol.[72] Aided by non-specific esterase, DCFCA is deacetylated to dichlorofluorescin (DCFH), which is not fluorescent. However, after reacting with reactive oxygen (or nitrogen) species, DCFH can be converted into the fluorescent DCF, which can be easily be visualised at around 525 nm with excitation at 488 nm. DCFH can also respond to heme proteins such as horseradish peroxidase (HRP) and myeloperoxidase in the presence of H_2O_2 to produce the radical intermediate.[73]

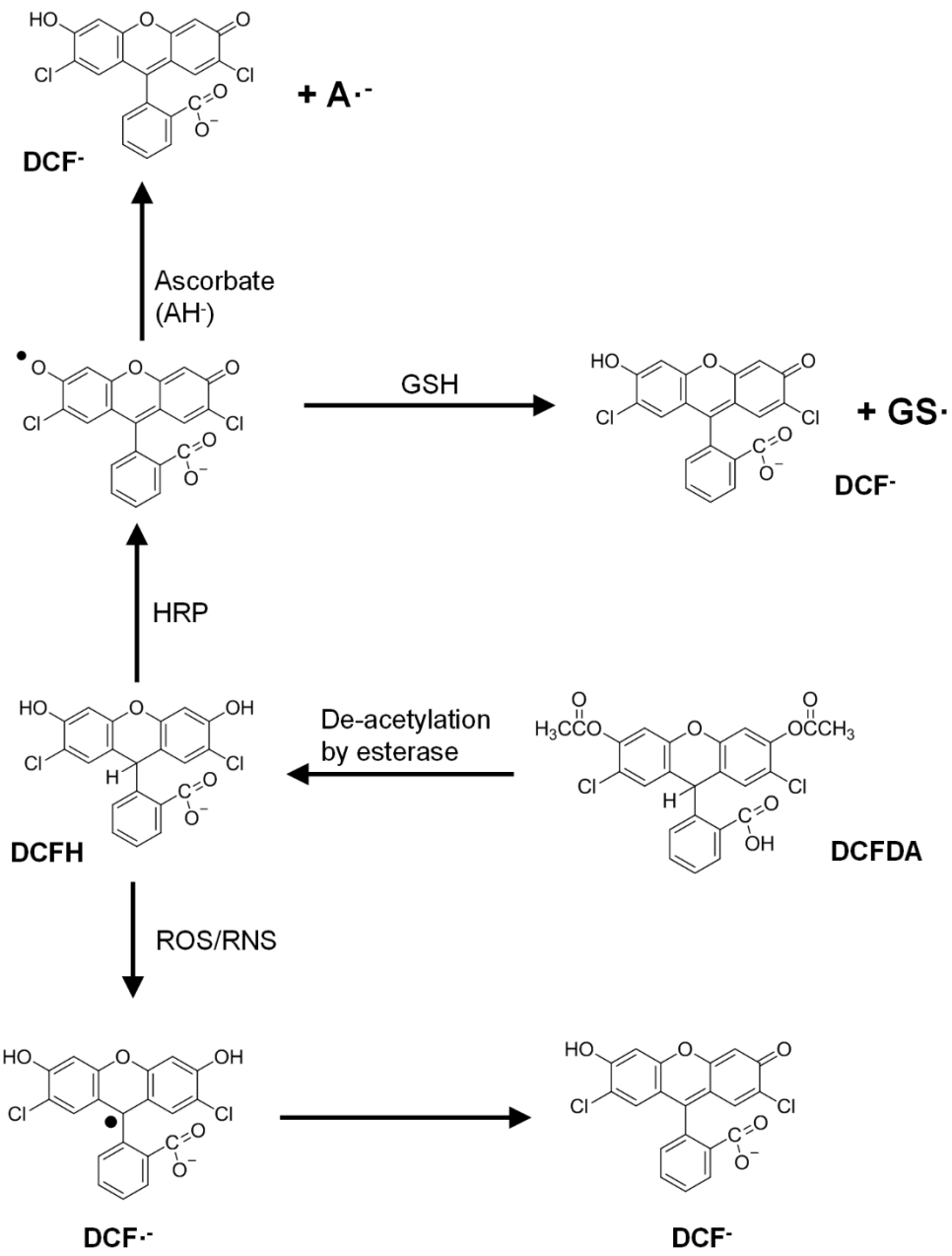

Figure 1.18 Conversion of DCFDA to fluorescent DCF in cells. DCFDA is firstly hydrolysed by non-specific esterase to form DCFH. DCFH can then be oxidised by ROS/RNS to yield the fluorescent DCF via an intermediate radical. Peroxidase can also convert DFDH to a phenoxyl radical, which can be reduced by Ascorbate or GSH to also generate the final fluorescent DCF.

Other than investigating the oxidative stress, fluorescent probes are also available for the detection of hypoxia. For example, pimonidazole-based probes have been very well established for the study of hypoxia.[77] However, although most of these probes are easy to use, they merely can be used to give an answer of yes or no concerning hypoxia but are unable to accurately quantify the degree of change in redox potential. Thus it is not sufficient to employ them for the further detailed study of redox regulation in cells.

1.5 An Alternative Approach to Intracellular Redox Monitoring

Dr. Colin Campbell's group has established a novel system to quantitatively measure and monitor the redox potential in live cells, using nanosensors based on Surface Enhanced Raman Spectroscopy (SERS).[78] Although fluorescence has been the dominant technique in the molecular imaging of live cells, it is worthwhile to note that it does have some shortcomings including photo-bleaching, cellular background interference, and cytotoxicity. The background fluorescence from cells, especially, is a significant issue which can cause inevitable errors in measurements. SERS offers a reliable and attractive alternative to fluorescence in cellular imaging.

1.5.1 Raman spectroscopy

Raman spectroscopy is a structural characterisation technique that relies on inelastic scattering of monochromatic light, which is known as Raman scattering. It was first observed in 1928 by two Indian scientists, C.V. Raman and K.S. Krishnan.[79]

Generally, the incident light acts as an electric field which disturbs the molecular

electronic charge distribution of the sample and thereby induces a dipole moment even in the case of a nonpolar molecular system. The induced dipole moment is proportional to the electric field applied to the molecules and the molecular polarisability.[80] The sum of the induced dipole moment constitutes the source for secondary electric field irradiated by the molecules. The secondary field just represents the scattered light. All the scattering processes are generated from the interaction between the incident photons and the molecular electronic system. The majority of the scattered photons oscillate at the same frequency as the incident light. This type of scattering is known as elastic or Rayleigh scattering and does not contain any information on the molecular structure. A small fraction (approximately 1 in 10 million) of the scattered photons oscillate at a different frequency from the original incident light. This is inelastic or Raman scattering, which consists of two scattering modes, Stokes and anti-Stokes scattering. Stokes scattering is the strongest form of Raman scattering which unravels the information of molecular structure. The emission of Stokes scattered photons is red-shifted with respect to the incident light, while anti-Stokes scattered photons are emitted with higher energy than the incident photons (blue-shifted).[81]

In Raman spectroscopy, the shift in vibrational frequency of the scattered photons compared to the incident photons is measured and reported on.[81]

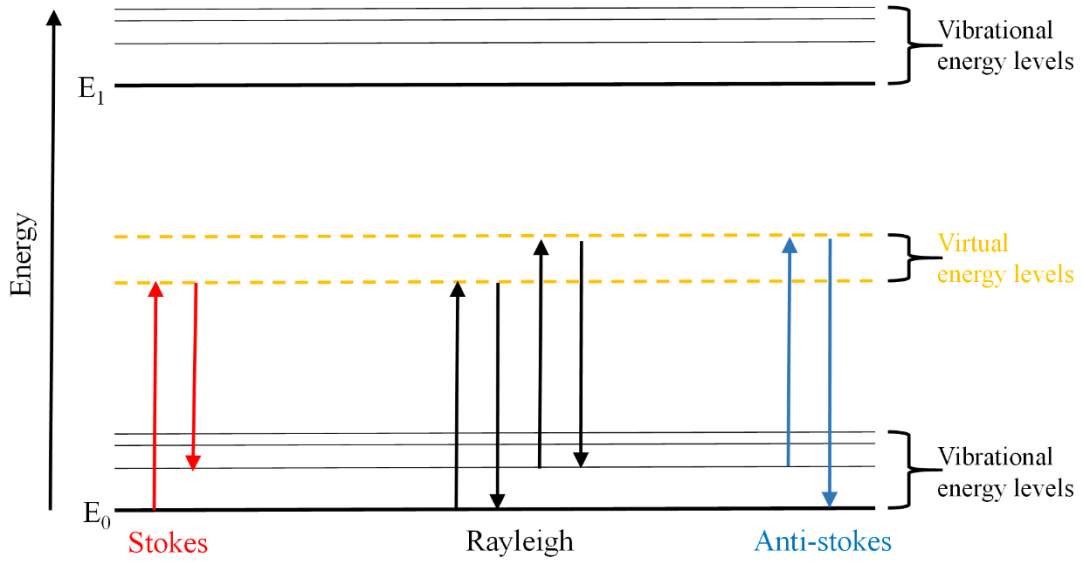

Figure 1.19 Diagram showing the energy level of the Rayleigh and Raman scattering processes

Raman spectroscopy is similar to infrared (IR) spectroscopy but analytes which are Raman active must undergo a change in polarisability. Thus symmetric vibrations are strongest in Raman spectroscopy rather than the asymmetric vibrations in infrared. It has a series of advantages over IR, for example, Raman spectroscopy doesn't require complex sample preparation and the measurement can be taken in seconds. Furthermore Raman spectroscopy is relatively insensitive to water, making it ideal for biological analyses.

However, the main disadvantage of Raman spectroscopy is that the Raman effect is very weak. Most of the scattered photons are elastically scattered which are not able to reveal molecular information. Fortunately, the effect can strengthened by SERS.

1.5.2 Surface Enhanced Raman Spectroscopy

Since SERS was first observed for pyridine adsorbed on a silver electrode in an electrochemical cell by Fleischmann and co-workers in 1974[82], it has been growing into a widely used analytical tool especially in biochemical analysis. SERS is a surface-sensitive technique which requires analytes to be in close proximity to a metal surface. An increase of up to 15 orders of magnitude of the Raman effect has been reported by adsorbing the analyte molecules on noble metal nanoparticles with strong surface curvature and roughness.[83]

The Raman intensity is proportional to the square of the molecular polarisatility and the intensity of the electromagnetic field. Thus this results in two complementary and multiplicative enhancement mechanisms, which are the electromagnetic mechanism (EM) for the electromagnetic field intensity and chemical enhancement mechanism for the molecular polarisatility. However the interplay of these two mechanisms, discussed below, is still under debate.[84]

1.5.2.1 Electromagnetic enhancement (EM)

EM accounts for enhancement factors of up to 10^{11}. This enhancement results from the excitation of localised surface plasmons (LSP) of the metal nanoparticles Excitation of LSPs causes a strong electromagnetic field within a range of a few nanometres from the surface of the nanoparticle. Therefore the electric field experienced by analyte molecules can be intensively amplified by the excited LSP. As stated above, the Raman intensity is proportional to square of the electromagnetic field applied to the analyte molecules. The LSP induced electric field strongly enhances the Raman intensity of molecules attached to the surface of metal

nanoparticles.[83–85]

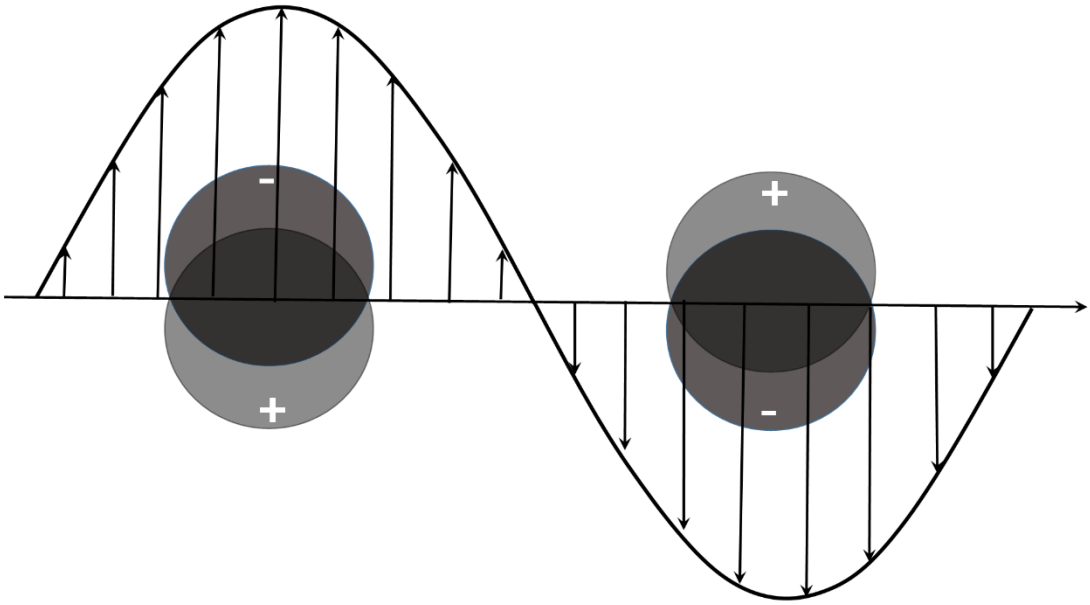

Figure 1.20 Excitation of a localised surface plasmon in a metal nanoparticle. Arrows indicate the electric field (adapted from *Ref. 81*).

1.5.2.2 Chemical enhancement

On the other hand, chemical enhancement also contributes to the amplification of the Raman effect by the chemisorption of a molecule on the metal surface. The formation of a surface complex between the molecule and the metal surface allows for resonant excitation of an electronically excited charge-transfer state, either transferring charge from the conduction band of the metal to the unoccupied molecular orbitals or vice versa. The charge transfer, as a consequence, increases the polarisability of the molecules.[83–85]

1.5.3 SERS-Based nanosensor for monitoring intracellular redox potential[78]

In the case of SERS for IRP monitoring, gold nanoshells (NS), consisting of a silica core coated in a thin layer of gold, have been used to enhance Raman signals. In this project, gold NS were products of Nanospectra Biosciences. Generally, the synthesis of gold nanoshells involves synthesis of cores and shells separately. The silica core particles with narrow size distribution can be synthesized using protocols developed by Stober.[86] The surface of the core particles, in this case which is silica, can be then modified with bifunctional organic molecules to enhance the coverage of gold shell layers. The final step is to coat the core particle with a controlled thickness of gold by the reduction of $HAuCl_4$ solution.[87] The use of gold here has many advantages: gold is biocompatible[88], SERS is immune to photo bleaching[89] and gold has tunable plasmon resonance in the near IR region.[90]

Two probe molecules:
1,8-diaza-4,5-dithia-1,8-di(2-chloro-[1,4]-naphthoquinone-3-yl)octane (NQ) and 2-Mercapto-benzene-1,4-diol (HQ) have been synthesised previously. Both contain a free thiol or sulfide as these moieties have an extremely high affinity with gold surfaces, which enables their chemisorption onto the NS, and the quinone moieties can undergo reversible $2e^-$, $2H^+$ redox reactions, which result in a change in their structure and SERS fingerprint with varying potentials.[78]

Figure 1.21 presents SERS spectra for NQ-NS and HQ-NS at different potentials and their oxidised/reduced reaction schemes, along with their half-wave potentials. The spectral changes at different potentials can be clearly seen. In these experiments, the potential was varied using a potentiostat to ascertain whether the differences in the

SERS spectra were directly linked to the changing potentials. When the normalised intensity of the potential-dependent peak is plotted against the potential, the midpoint potential correlates well with the half-wave potential measured by cyclic voltammetry. Consequently, SERS spectra collected from the nanosensors inside the cells can be used to report on the intracellular redox potential based on calibration curves built from the potential-dependent spectral changes.

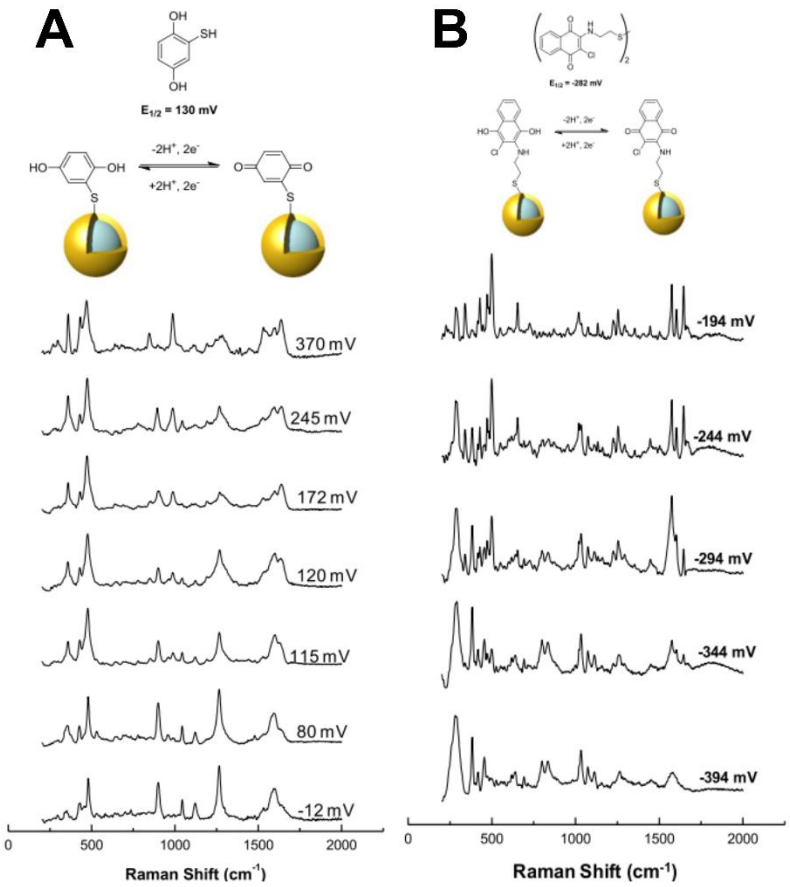

Figure 1.21 Chemical structures, half-wave potentials, redox reaction schemes and potential-dependent SERS spectra of the probe molecules. A: HQ B: NQ[78]

The successful establishment of a SERS-based nanosensing system provides a novel access to probing the IRP in live cells in a reversible and accurate way. However, it is

worth noting that the coverage windows of the two established probes are limited. HNQ is only useful for supraphysiological oxidative stress while NQ only covers a range within normal physiological redox potentials. A potential gap between the two probes needs to be filled and there is also a need to extend the technique to quantify cellular hypoxia.

1.6 Project Aim

The main aims of my project were:

i) To synthesise and characterise nanosensors for expanding the measuring range

In terms of the ease with which to modify the structure of the organic probe molecules and thus tune their half-wave potentials, quinone derivatives with various modifications have significant potential to broaden the coverage window and thus mature the nanosensing device.

ii) To screen the delivery of nanosensors into cells

Previous research in our group has demonstrated nanosensors can be delivered into the cytosol without inducing cytotoxicity. However, it was still necessary to ensure that different modifications of the nanoparticle surfaces would not produce any toxic effects to cells. In addition, targeted delivery to mitochondria was also investigated.

iii) To apply the nanosensors in monitoring IRP associated with cellular hypoxia

Cellular hypoxia is the reductive disorder in cells. The lack of quantitative measurement of cellular hypoxia hampers the comprehensive study of it. SERS-based nanosensors with an ability to quantify cellular hypoxia could greatly facilitate its understanding. This was the ultimate goal of my project.

Chapter 2 Materials and methods

All chemicals and reagents, unless stated otherwise, were purchased from Sigma Aldrich and used without further purification. Solvents were purchased from Fisher Scientific

2.1 Synthetic work

2.1.1 Probe Molecule Synthesis

All melting points were measured with a Gallenkamp capillary tube melting point apparatus.

Analytical thin layer chromatography (TLC) was performed on silica TLC plates (0.25 mm thickness). Dry-flash column chromatography was performed on silica gel (grade 60, 230-400 mesh, 60Å). TLC plates and silica gel were purchased from Merck。

2.1.1.1 N-[2-({2-[(9,10-dioxo-9,10-dihydroanthracen-2-yl)formamido]ethyl}disulfanyl)ethyl]-9,10-dioxo-9,10-dihydroanthracene-2-carboxamide (AQ)

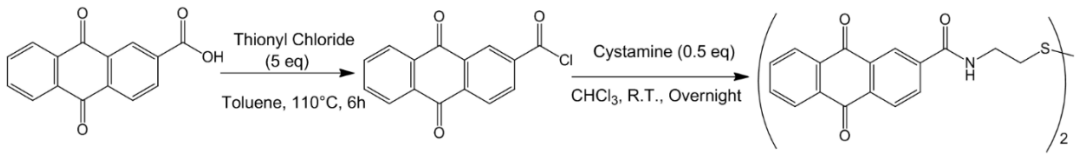

Scheme 2.1 Synthetic scheme for AQ.

Thionyl chloride (4.5 ml, 30mmol) was added to a solution of 9.10-anthraquinone-2-carboxylic acid (100mg, 0.397mmol) in toluene (25ml) and heated for 6hours at 110℃. The solvent was removed *in vacuo.* Then the solid was re-dissolved in toluene (3 mL) and the solvent was removed *in vacuo* again to get rid of the trace thionyl chloride. The resultant solid was dissolved in chloroform (3 mL) and added to a solution of cystamine 2HCL (100.12 mg, 0.45 mmol) in chloroform (30mL) with a few drops of triethylamine. The resulting solution was stirred for 11 hours at room temperature and pressure. The solvent was removed *in vacuo*. The products were exatracted using chloroform (230mL), washed three times with water and dried over Na_2SO_4. The solvent was removed under reduced pressure. Then the resulting solid was added to hexane (150 mL), heated for half an hour to remove the impurities and filtered off. 146 mg of AQ were synthesised in 84% yield according to the procedure outlined by Nagata *et al*[91]: mp 219-222 ℃; ^{1}H NMR (500 MHz, $CDCl_3$) δH 3.12-3.16 (t, J 6.3, 4H), 3.92-3.96 (q, J 6.3, 4H), 7.40 (b s, 2H), 7.78-7.82 (m, 4H), 8.22-8.37 (m, 8H), 8.62 (s, 2H); ^{13}C NMR (500 MHz, $CDCl_3$) δC 37.98, 39.90, 125.29, 127.33, 127.36, 127.87, 133.24, 133.34, 134.34, 134.41, 135.16, 139.16, 166.27, 182.41.

2.1.1.2

2-chloro-3-{[2-({2-[(3-chloro-1,4-dioxo-1,4-dihydronaphthalen-2-yl)amino]ethyl}disulfanyl)ethyl]amino}-1,4-dihydronaphthalene-1,4-dione (NQ)

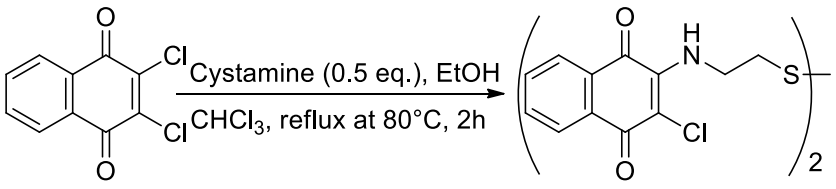

Scheme 2.2 Synthetic scheme for NQ

A solution of 201.0 mg Cystamine in 30 ml chloroform with a few drops of trimethylamine was added into the solution of 403.6 mg 2,3 dichloro-1,4-naphthoquinoe in 100 ml hot ethanol. The mixed solution was heated under reflux at 80 ℃ for three hours. The resulting solution was evaporated *in vacuo* to obtain red solid. The resultant product was extracted using 250 ml chloroform, washed three times with water and dried over Na_2SO_4. The solvent was removed under reduced pressure. 410 mg of NQ were synthesised in 86% yield according to the procedure outlined by Nagata *et al*[91]: mp 192-195 ℃; ^{1}H NMR (500 MHz, $CDCl_3$) δH 3.03-3.05 (t, J 6.5, 4H), 4.21-4.26 (q, J 6.5, 4H), 6.34-6.44 (b s, 2H), 7.64-7.78 (m, 4H), 8.06-8.18 (m, 4H); ^{13}C NMR (500 MHz, $CDCl_3$) δC 38.64, 43.12, 126.09, 126.98, 129.76, 133.53, 132.67 135.04, 143.84, 178.876, 180.33.

2.1.1.3 2-chloro-3-{[2-({2-[(3-chloro-8-nitro-1,4-dioxo-1,4-dihydronaphthalen-2-yl)amino]ethyl}disulfanyl)ethyl]amino}-5-nitro-1,4-dihydronaphthalene-1,4-dione (NNQ)

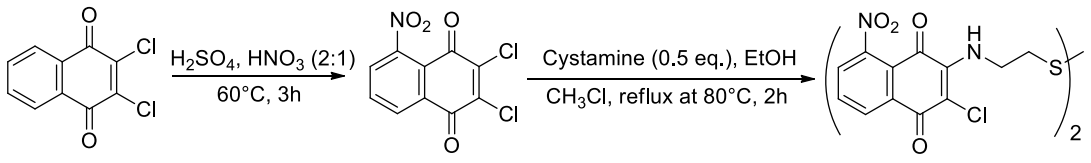

Scheme 2.3 Synthetic Scheme for NNQ

8.5mL 70% nitric acid was added to 14.0mL concentrated sulfuric acid. Then under stirring, 4.0040g (0.0176mol) 2,3-dichloro-1,4-naphthoquinone was added to the acid mixture. The solution was heated to 60 ℃ for 2 hours. The reaction mixture was then poured over 100mL ice, filtered off and the crystals obtained were washed with water for 3 times. The yellow crystal was recrystallised using chloroform and the product (2, 3-Dichloro-5-nitro-1, 4-naphthoquinone) was isolated by filtration in a yield of 42% (2.01g, 7.4 mmol). 483.2mg (1.78mmol) 2, 3-Dichloro-5-nitro-1, 4-naphthoquinone was dissolved in 100mL hot ethanol (solution 1). Then 201.0mg cystamine 2HCl (0.893mmol) was dissolved in 30 mL in chloroform with a few drops of triethylamine under sonication (solution 2). Into the hot solution 1, solution 2 was added slowly. The resulting solution was heated to keep reflux at 80 ℃. After 2 hours, the resultant red solid was filtered off, washed thoroughly with chloroform and dried over air, giving 528mg the final product in a yield of 95%. 528 mg of NNQ were synthesised in a final yield of 40% according to the procedure outlined above: mp 182-185 ℃; ^{1}H NMR (D-DMSO): δ 3.02 (4H, t, CH-S) 4.05 (4H, q, CH-N) 7.56 (2H, t, N-H) 7.74 (2H, td, 8H) 7.82 (2H, td, 7H) 7.96 (2H, d, 6H) ^{13}C NMR (500 MHz, DMSO) δC 33.28, 40.86, 118.95, 123.68, 126.87, 129.56, 132.67, 137.35, 142.04, 168.15, 186.56.

2.1.1.4 6,7-dichloro-N-(2-{[2-(6,7-dichloro-5,8-dioxo-5,8-dihydronaphthalene-2-sulfonamido)ethyl]disulfanyl}ethyl)-5,8-dioxo-5,8-dihydronaphthalene-2-sulfonamide (SNQ)

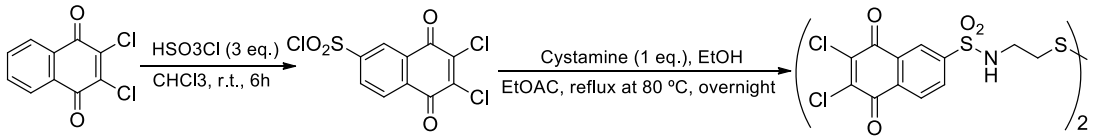

Scheme 2.4 Synthetic Scheme for SNQ

15 ml chlorosulfonic acid was slowly added during 15 mins to a stirred suspension of 5 g 2,3-dichloro-1,4-naphthoquinone in 30 ml chloroform in the ice bath. The reaction solution was heated to 50 ℃ for 12 hours. The reaction mixture was then poured over 200 ml ice, filtered off and the crystals obtained were washed with cold water for 3 times. The brownish resultant solid was recrystallised using chloroform, isolated by filtration and dried in a desiccator. 3.520 g brownish solid (solid 1) was obtained. 500 mg solid 1 was dissolved in 100 ml ethyl acetate (solution 1). Then 300.0mg cystamine·2HCl was dissolved in 30 mL in chloroform with a few drops of triethylamine under sonication (solution 2). Into the hot solution 1, solution 2 was added slowly. The resulting solution was heated to keep reflux at 80 ℃. After 24 hours, the resultant greyish solid was filtered off, washed thoroughly with chloroform and ethyl acetate and dried over air, giving 448mg the final product in a yield of 38%. 448 mg of SNQ were synthesised in 38% yield according to the procedure outlined above: mp 214-218 ℃; ^{1}H NMR (D-DMSO): δH 3.01-3.05 (m, 4H), 3.07-3.12 (m, 4H), 8.27 (s, 3H) ^{13}C NMR (500 MHz, DMSO) δC 34.94, 36.36, 116.84, 118.57, 124.63, 128.87, 130.54, 136.45, 146.66, 170.20, 178.44.

2.1.1.5 N-(2-{[2-(9,10-dioxo-9,10-dihydroanthracene-2-sulfonamido)ethyl]disulfanyl}ethyl)-9,10-dioxo-9,10-dihydroanthracene-2-sulfonamide (SAQ)

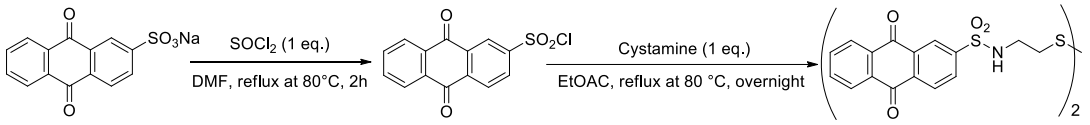

Scheme 2.5 Synthetic Scheme for SAQ

20 ml thionyl chloride was added slowly and dropwise into stirring 5.75 g sodium anthraquinone-2-sulfonate. 1 ml DMF was added into the mixture solution. The reaction solution was heated to 80 ℃ for 2 hours and then poured onto over 200 ml ice. The resultant greyish solid was filtered off, washed three times with water and dried in a desiccator overnight. 3.885 g solid (solid 1) was obtained in this step. 700 mg solid 1 was dissolved in 100 ml ethyl acetate (solution 1). Then 300.0mg cystamine·2HCl was dissolved in 30 mL in chloroform with a few drops of triethylamine under sonication (solution 2). Into the hot solution 1, solution 2 was added slowly. The resulting solution was heated to keep reflux at 80 ℃. After 24 hours, the resultant whitish solid was filtered off, washed thoroughly with chloroform and ethyl acetate and dried over air, giving 654mg the final product in a final yield of 51%. 654 mg of SAQ were synthesised in 51% yield according to the procedure outlined above: mp 203-207 ℃; ^{1}H NMR (D-DMSO): δH 2.69-2.72 (t, J 6.79, 4H), 3.08-3.10 (t, J 6.79, 4H), 7.95-7.96 (dd, J 3.33 5.58, 6H), 8.19-8.25 (m, 6H), 8.37-8.40 (m, 2H), 8.51 (d, J 1.36, 2H) 13C NMR (500 MHz, DMSO) δC 33.56, 37.79, 117.62, 119.54, 119.68, 124.87, 130.25, 130.69, 134.17, 134.38, 134.98, 142.69, 158.36, 172.61

2.1.2 Nuclear localisation sequence peptides synthesis[92]

9-fluorenylmethyloxycarbonyl (Fmoc)-protected amino acids (AAs), Rink amide linker and aminomethyl polystyrene resin were purchased from GL Biochem.

Peptide purity was checked using an Agilent 1100 series HPLC coupled with an evaporative light-scattering detector (ELSD) (Polymer Labs ELS-1000 detector).

All coupling reactions were performed at room temperature. SPPS was carried out manually using an isolate filtration reservoir as the reaction vessel, fitted with polyethylene frits (Argonaut Technologies Inc.). AAs were protected with Fmoc group at the *N*-terminus and acid labile protecting groups on the side chains. Either the Kaiser test for primary amines or the Chloranil test for secondary amines were employed to assess the completion of each synthetic step.

Kaiser test: Solution A: 80 g phenol in 20 ml EtOH and 2 ml 0.001 M aqueous KCN in 98 ml pyridine combined. Solution B: 5 g Ninhydrin in 100 ml EtOH. Three drops of solution A and two drops of solution B were added to a tiny amount of resin beads. The mixture was heated at 100 ℃ for 2 min and the colour of the solution and/or the beads was observed.

Positive result: resin/solution light to dark purple/blue, primary amine present
Negative result: resin/solution colourless or light yellow, no primary amine present

Chloranil test: Solution A: 2% acetaldehyde in DMF. Solution B: 2% chloranil in DMF. Two drops of solution A and two drops and solution B were added to a tiny

amount of resin beads. The mixture was heated at 100 ℃ for 2 mins and the colour of the solution or/and the resin was observed.

Positive result: resin/solution light to dark purple/blue, primary/secondary amine present

Negative result: resin/solution colourless or light yellow, no primary/secondary amine present

2.1.2.1 Synthesis of CGGPKKKRKVGG (NLS-1)

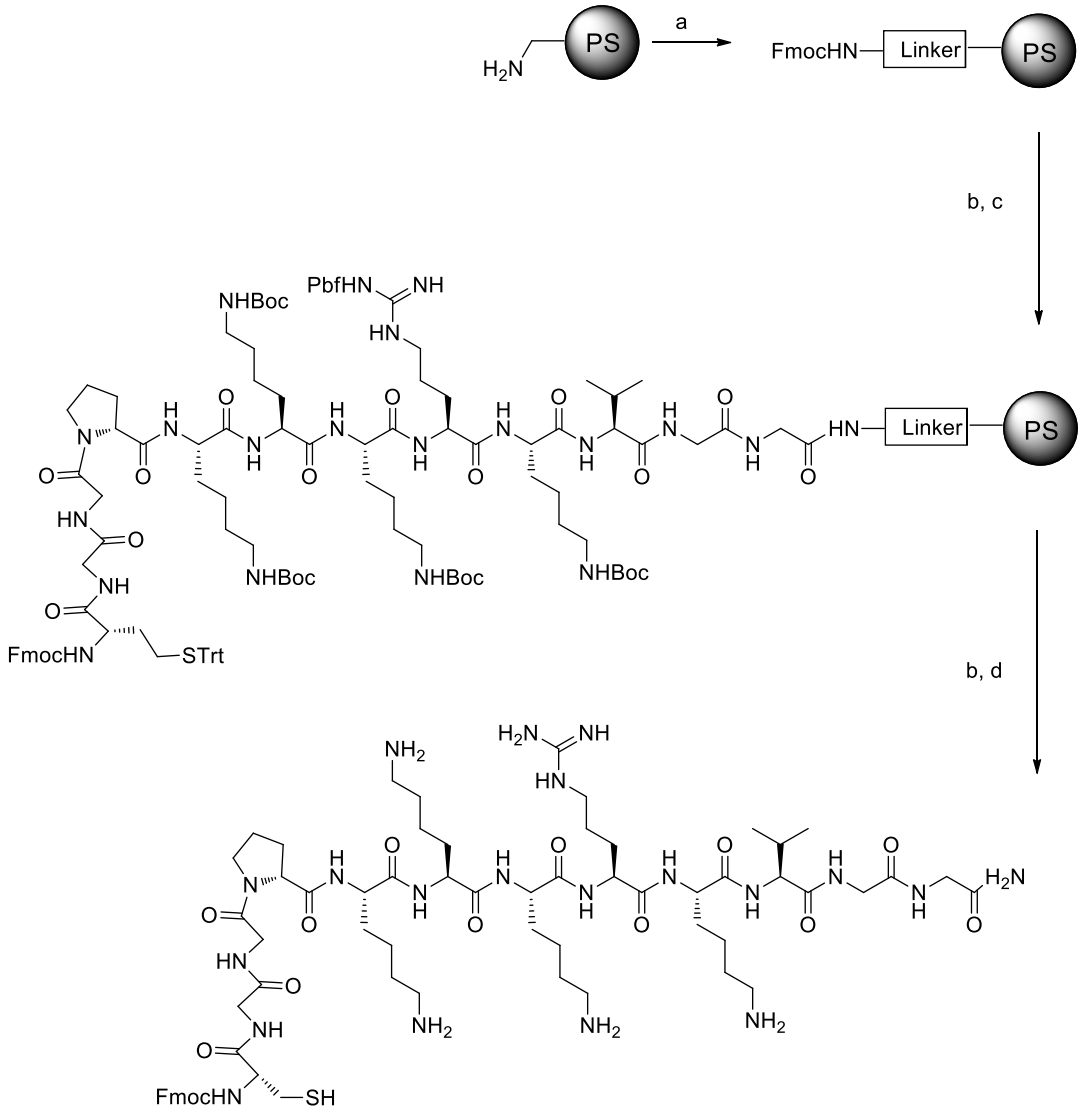

Scheme 2.6 Synthetic scheme of NLS-1. a: Rink amide linker (2 eq.), oxyma (2 eq.), DIC (2 eq.) in DMF, shaken for 1 h, the whole procedure (a) was repeated once. b: 20% piperidine in DMF, shaken for 10 min, the whole procedure (b) was repeated once, c: AAs (2 eq.), oxyma (2 eq.), DIC (2 eq.) in DMF, shaken for 1 h. d: 88% TFA, 2% TIS, 5% PhOH, 5% H_2O, shaken for 2 h.

Coupling the linker to the resin: Aminomethyl polystyrene resin (loading 0.75 mmol/g, 0.32 g, 0.24 mmol) in a 6ml vessel was swollen in DCM (4 ml) for 5 mins and washed with DMF (3 × 4 ml), methanol (3 × 4 ml) and DCM (3 × 4 ml) in order. Rink amide linker (259 mg, 0.48 mmol), oxyma (68 mg, 0.48 mmol) were dissolved in 3 ml DMF, and 78 µl DIC (0.48 mmol) was added into this solution. The resultant solution was then shaken for 10 min to be activated. The mixture was added to the resin and shaken for 1 h. The resin was washed and filtered with DMF (3 × 4 ml), methanol (3 × 4 ml) and DCM (3 × 4 ml), in that order. After drying under vacuum, the coupling procedure was then repeated before a small amount of the resin was subjected to the Kaiser test.

Coupling of AAs: A solution of 20% piperidine in DMF (4 ml) was added to the resin and shaken for 10 min. The resin was filtered and washed with DMF (3 × 4 ml), methanol (3 × 4 ml) and DCM (3 × 4 ml), in that order. The above procedure was repeated and the resin was dried under vacuum. The Kaiser test was positive. To a solution of the appropriate AA (0.48 mmol) in DMF (3 ml) was added oxyma (68 mg, 0.48 mmol) and DIC (78 µl, 0.48 mmol) and the resultant solution was shaken for 10 min. This mixture was added to the resin and shaken for 1 hour. The resin was filtered and washed with DMF (3 × 4 ml), methanol (3 × 4 ml) and DCM (3 × 4 ml), in that order. The Kaiser test was negative. The resin was swollen in DCM (4 ml) and a solution of 20% piperidine in DMF (4 ml) was added to the resin and shaken for 10 min. The resin was filtered and washed with DMF (3 × 4 ml), methanol (3 × 4 ml) and DCM (3 × 4 ml), in that order. The above procedure was repeated, and the resin was then washed with Et_2O (3 × 4 ml), dried under vacuum and stored with the foil on for cleavage.

Cleavage from resin: Resin in a 6 ml vessel was re-swollen for 5 min in 4 ml DCM and filtered. A solution of TFA: TIS: PhOH: H_2O (88: 2: 5: 5, 3 ml) was added and the vessel was shaken for 2 h. The resultant mixture was filtered into ice-cold Et_2O (30 ml). The precipitant solid was washed with Et_2O 3 times, pelleted by centrifugation and decantation and then dried under vacuum.

NLS-1 characterisation data: White solid; MS data $C_{70}H_{105}N_{17}O_{16}S$ calc. 1455.7783 Da, found 1455.8 Da; ELSD retention time – 0.606 min (100% pure).

2.1.2.2 Synthesis of Fluorescein-aminohexanoic acid-PKKKRKVC (NLS-2)

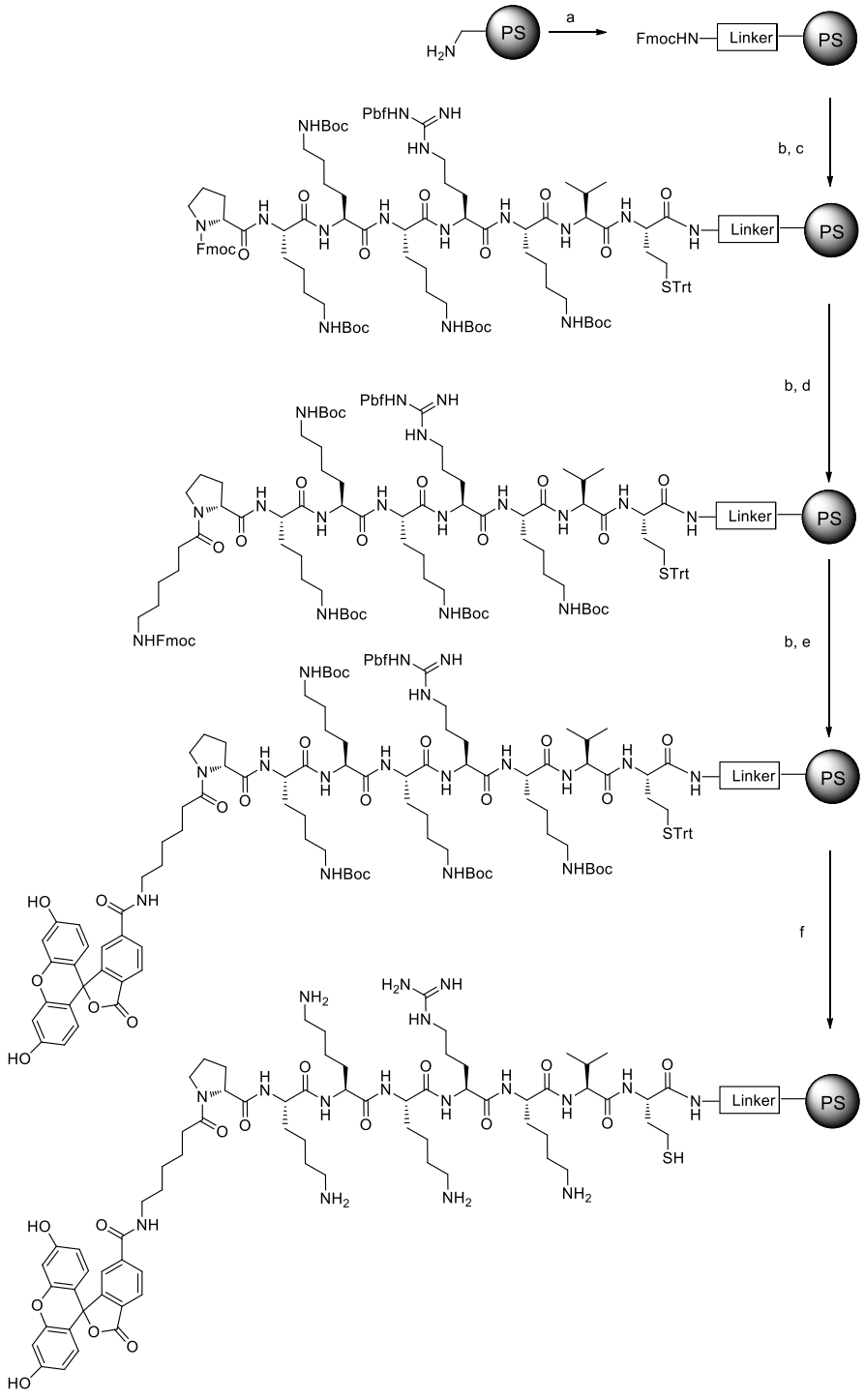

Scheme 2. 7 Synthetic scheme of NLS-2. a: Rink amide linker (2 eq.), oxyma (2 eq.), DIC (2 eq.) in DMF, shaken 1 h, the whole procedure (a) was repeated once. b: 20% piperidine in

DMF, shaken 10 min, the whole procedure (b) was repeated once. c: AAs (2 eq.), oxyma (2 eq.), DIC (2 eq.) in DMF, shaken 1 h. d: *N*-Fmoc-6-aminohexanoic acid (2 eq.) oxyma (2 eq.), DIC (2 eq.) in DMF, shaken 1 h. e: 5(6)-carboxy fluorescein (2 eq.), oxyma (2 eq.), DIC (2 eq.) in DMF, shaken 1 h. f: 88% TFA, 2% TIS, 5% PhOH, 5% H_2O, shaken 2 h.

Coupling of the Rink linker to the resin and coupling of the AAs were as described for the synthesis of NLS-1.

Coupling of spacer to 8-mer resin: After coupling of AAs, a solution of 20% piperidine in DMF (4 ml) was added to the resin and shaken for 10 min. The resin was filtered and washed with DMF (3 × 4 ml), methanol (3 × 4 ml) and DCM (3 × 4 ml), in that order. The above procedure was repeated once and the resin was dried under vacuum. The Kaiser test was positive. To a solution of *N*-Fmoc-6-aminohexanoic acid (176 mg, 0.48 mmol) in DMF (3 ml) was added oxyma (68 mg, 0.48 mmol) and DIC (78 µl, 0.48 mmol) and the resultant solution was shaken for 10 min. This mixture was added to the resin and shaken for 1 h. The resin was filtered and washed with DMF (3 × 4 ml), methanol (3 × 4 ml) and DCM (3 × 4 ml), in that order. The Kaiser test was negative

Coupling of fluorescein to spacer-8-resin: After coupling of the spacer, a solution of 20% piperidine in DMF (4 ml) was added to the resin and shaken for 10 min. The resin was filtered and washed with DMF (3 × 4 ml), methanol (3 × 4 ml) and DCM (3 × 4 ml,) in that order. The above procedure was repeated once and the resin was dried under vacuum. The Kaiser test was positive. To a solution of 5(6)-carboxyfluorescein (181 mg, 0.48 mmol) in DMF (3 ml) was added oxyma (68 mg, 0.48 mmol) and DIC (78 µl, 0.48 mmol) and the resultant solution was shaken for 10 min. This mixture was added to the resin and shaken for 1 h. The resin was

filtered and washed with DMF (3 × 4 ml), methanol (3 × 4 ml) and DCM (3 × 4 ml), in that order. The Kaiser test was negative. The resin was swollen in DCM (4 ml) and a solution of 20% piperidine in DMF (4 ml) was added to the resin and shaken for 10 min. The resin was filtered and washed with DMF (3 × 4 ml), methanol (3 × 4 ml) and DCM (3 × 4 ml), in that order. The above procedure was repeated once. The resin was then washed with Et_2O (3 × 4 ml), dried under vacuum and stored with the foil on for cleavage.

NLS-2 characterisation data: Yellow solid; MS data $C_{51}H_{96}N_{20}O_{12}S$ calc. 1213.0753 Da, found 1213.2 Da. ELSD retention time - 3.665 and 3.927 min (99% pure)

2.2 Cellular experiments

Dulbecco's modified Eagle's medium (DMEM), heat-inactivated calf serum (CS), penicillin/streptomycin, trypsin/ethylenediaminetetraacetic acid (EDTA) and L-glutamine were all purchased from Life Technologies. Phosphate buffered saline (PBS) and Corning® Cell Culture Flasks were purchased from Sigma Aldrich.

2.2.1 General cell culture condition

A549 cells were cultured in DMEM supplemented with penicillin/streptomycin (10,000 units/ml), L-glutamine (200 mM), and 10% CS. Cells were incubated at 37 ℃ and 5% CO_2 in a humidified incubator.

When freezing cells for long-term storage, cells were suspended in freezing media (90% culture media, 10% DMSO). 1 ml aliquots of suspended cells were pipetted

into 1.8 ml cryovials, transferred to a Nalgene Cryo 1 ℃ freezing container and stored at -80 ℃ in a freezer overnight. The next day, cryovials were transferred to liquid nitrogen storage.

In order to thaw frozen cells from liquid nitrogen storage, cryovials were removed from the liquid nitrogen and the cells thawed slowly at r.t. The thawed content was gently and carefully transferred to a 50 ml falcon tube with 10 ml fresh media. After centrifuging at 1000 rpm for 5 min, the supernatant was removed. The pellet was re-suspended in 5 ml fresh media and transferred to a new 75 cm^2 cell-culture flask for culturing with 10 ml fresh media. The following day, old media was removed and cells were washed with phosphate-buffered saline (PBS) twice to remove trace DMSO, and 15 ml fresh media then added.

When passaging cells, old media was removed and cells were washed with 10 ml PBS. Cells were harvested via 1.5 ml trypsination (trypsin/ ethylenediaminetetraacetic acid (EDTA)) at 37 ℃ and 5% CO_2 for 5 min. The detached cells were re-suspended in 10 ml fresh media and pelleted by centrifugation at 1000 rpm for 5 min. Appropriate aliquots were seeded for continued growth.

2.2.2 Fluorescent hypoxia assay

Cyto-ID® Hypoxia/Oxidative Stress Detection Kit was purchased from Enzo Life Sciences. On Day 1, 50,000 cells were seeded on quartz coverslips (UQG Optics Ltd, UK) in a 24-well plate and incubated for 24 h at 37 ℃ and 5% CO_2 in a humidified incubator. On day 2, after thorough washing with PBS, CS-free DMEM was added. Cells were treated with AQ-NS (10 fM), cobalt chloride (100 μM), or AQ-NS plus cobalt chloride (10 fM and 100 μM, respectively) overnight. On day 3, cobalt

chloride (100 μM) was added into cells treated only with AQ-NS timely for 3 h and 6 h treatment. Positive control cells were treated with DFO in CS-free DMEM for 3 h and negative control cells were incubated in CS-free DMEM only. Cells were thoroughly washed with PBS to remove the experimental reagents and then covered by a sufficient volume of the Hypoxia assay reagent, incubated under normal tissue culture conditions (37℃ and 5% CO_2) for 30 min. Hypoxia assay reagent was carefully removed from the 24-well plates by gently tapping the plates against layers of paper towel. Cells were washed in PBS twice. A Zeiss Axio Imager comprising a filter set compatible with Texas Red (596 nm excitation /670 nm emission) was used to record the fluorescence of cells and VECTASHIELD mounting medium was used to help maintain the fluorescence intensity. All fluorescence images were analysed using ImageJ 1.47v.

2.2.3 Transmission electron microscopy (TEM) of nanoparticles in cells

Cells were grown to appropriate confluence on Agar Scientific Thermanox coverslips and were incubated overnight with the required nanoparticles in CS-free media. The cells were washed three times with phosphate-buffered saline (PBS) and fixed for 2 h in 3% (v/v) glutaraldehyde in 0.1 M sodium cacodylate buffer. The cells were then washed three times with 0.1 M sodium cacodylate buffer, followed by post-fixation overnight with 1% (w/v) osmium tetroxide in 0.1 M sodium cacodylate buffer, dehydrated with acetone (50-100% in steps of 50, 70, 90 and 100%) and then infiltrated and embedded in epoxy resin. Ultrathin sections of the sample were taken using a diamond knife. The sections were positioned on grids and stained with 2% aqueous uranyl acetate. The grids were then examined and photographed at an

accelerating voltage of 80 keV in a CM120 Biotwin (Philips) transmission electron microscope connected to a digital camera.

2.2.4 MTT assay

A549 cells were seeded in a 96-well plate at a density of 1,000 cells/well. Following incubation for 24 h in a humidified incubator with 5% CO_2 at 37 ℃, cells were washed twice with PBS before treatment with AQ-NS (10 fM), NC-PPh_3 (100 fM) and NR-PPh_3 (100 fM) in CS-free media. After further overnight incubation, cells were thoroughly washed with PBS and the wells charged with fresh phenol red-free media (90 µl) and 3-(4,5-dimethylthiazol-2-yl)-2,5-diphenyltetrazolium bromide solution (10 µl, 5 mg/ml). After 4 h treatment, media was carefully removed so as not to disturb the cells and formazan was dissolved using 100 µl solubilising solution (10% TRITON X-100, 0.1 N HCl in IPA), gently shaking until full dissolution was achieved. Absorbance was recorded on a BIOTEK Synergy HT microplate reader at 570 nm and 690 nm.

2.2.5 Mitochondria isolation

Pierce Mitochondria Isolation Kit for Cultured Cells and Halt Protease Inhibitor Cocktail, EDTA-free (100X) were purchased from Thermo Scientific. Dounce Tissue Grinder was purchased from Sigma Aldrich.

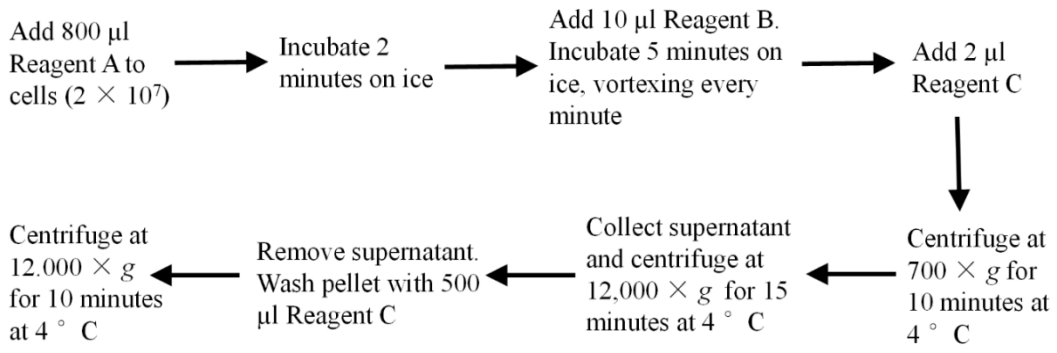

Scheme 2.8 Procedure summary of the Mitochondria Isolation Kit

Immediately before use, protease inhibitors was added to the Reagent A and Reagent C; inhibitors were only added to the reagent amount being used for the procedure and not to the stock solutions. 2×10^7 cells was pelleted by centrifuging harvested cell suspension in a 2.0 ml microcentrifuge tube at ~850 × *g* for 2 minutes. The supernatant was carefully removed and discarded. 800 µl of Reagent A was added in and vortexed at medium speed for 5 seconds. The tube was incubated on ice for exactly 2 minutes. Cell suspension was transferred to the Dounce Tissue Grinder. Cells were homogenised on ice. 50 strokes were performed to effectively lyse the cells for 80% lysis rate with a small clearance pestle (0.05 mm). Cell lysates were return to the original tube and 800 µL of Mitochondria Isolation Reagent C was added in. The Dounce Tissue Grinder was rinsed with 200 µL of Mitochondria Isolation Reagent A and then the solution was added into the tube containing the sample. The tube was inverted several times to mix. The tube was subject to centrifuge at 700 × *g* for 10 minutes at 4 ℃. The supernatant was transferred to a new, 2.0 ml tube and centrifuged at 12,000 × *g* for 15 minutes at 4 ℃. The supernatant (cytosol fraction) was transferred to a new tube. The pellet contained the isolated mitochondria.500 µl Reagent C was added to the pellet, and centrifuged at 12,000 × *g* for 5 minutes. The supernatant was discarded. The mitochondrial pellet was maintained on ice for use.

2.2.6 Isolated mitochondrial delivery

MAITE medium was used to keep isolated mitochondria healthy and alive.

MAITE medium: 25 mM sucrose, 7 mM sorbitol, 100 mM KCl, 0.05 mM EDTA, 5 mM $MgCl_2$, 10 mM Tris-HCl, pH 7.4 and 10 mM H_3PO_4. For a 100 ml solution, 0.86 g sucrose, 1.37 g sorbitol and 0.74 g KCl were dissolved and then 10 µl 0.5 M EDTA, 500 µl of 1 M $MgCl_2$, 2 ml 0.5 M Tris-HCl, and 68 µl orthophosphoric acid were added in. The pH was adjusted to 7.4 using 0.5 M Tris base and tissue culture water was added for a final volume of 100 ml. The solution was sterilised by filtration through a 0.2 µm filter and stored at 4 ℃. Each filter was used for only 10 ml medium.

The isolated mitochondrial pellet was carefully re-suspended in 300 µl MAITE medium. 100 µl of the mitochondrial suspension was incubated with 100 fM SBTPP functionalised NS and NR overnight on ice before washing twice with MAITE medium by centrifugation at 5000*g*. All the procedures were performed in a cold room at 4 ℃.

2.2.7 BCA Protein Assay of isolated mitochondria

Pierce BCA Protein Assay Kit was purchased from Thermo Scientific.

A) Mitochondrial lysis

1. 50 µl of the 2% in Tris-buffered saline was added in 100 µl of the isolated mitochondria and the tube was vortexed for 1 min.
2. The mitochondria were centrifuged at 12,000*g* for 2 min. The supernatant contained soluble mitochondrial protein that could be analysed by BCA

Protein Assay.

B) Preparation of Diluted BSA standards

A set of protein standards were prepared by diluting the stock BSA solution. (Table 2.1)

Table 2.1 Preparation of Diluted BSA standards

Vial	Volume of Diluent (µl)	Volume of BSA solution (µl)	Final BSA concentration (µg/ml)
A	0	300 of stock	2000
B	125	375 of stock	1500
C	325	325 of stock	1000
D	175	175 of vial B	750
E	325	325 of vial C	500
F	325	325 of vial E	250
G	325	325 of vial F	125
H	400	100 of vial G	25
I	400	0	0

C) Preparation of the BCA working reagent (WR)

6 ml of the WR was required for 3 replicates. The WR was prepared by mixing 50 parts of BCA Reagent A with 1 Part of BCA Reagent B (6 ml of Reagent A and 120 µl of Reagent B).

D) Microplate measurement

25 µl of each standard or mitochondrial sample replicate was pipetted into a 96-well plate. 200 µl of the WR was added into each well and the plate was mixed thoroughly. The plate was covered and incubated at 37 ℃ for 30 min. After cooling to room temperature, the absorbance was measured at 562 nm on a BIOTEK Synergy HT microplate reader. The 562 nm absorbance of the blank standard was subtracted from the 562 nm measurements of all other standards and sample replicates. The

standard curve was built by plotting the average blank-corrected 562 nm measurements for each BSA standard vs. its concentration in μg/ml. The curve was then used to determine the protein concentration of the isolated mitochondria.

2.2.8 MTT Assay for isolated mitochondria

Isolated mitochondria were diluted and re-suspended in MAITE Medium to 50 μg/ml. 20 μl 3-(4,5-dimethylthiazol-2-yl)-2,5-diphenyltetrazolium bromide solution (5 mg/ml) and 10 of disodium succinate solution (50 mM) were added into 70 μl diluted mitochondrial suspension in a Molecular BioProducts 0.2 ml clear PCR tube. After incubating on ice for 6 h, the tube was placed in a 1.5 ml Eppendorf tube and centrifuged at 6000*g* for 5 min. The supernatant was carefully removed without disturbing the pellet. The resultant formazan was dissolved using 100 μl solubilising solution (10% TRITON X-100, 0.1 N HCl in IPA), gently shaking until full dissolution was achieved. The mixture was transferred to a 96-well plate and absorbance was recorded on a BIOTEK Synergy HT microplate reader at 570 nm and 690 nm. All the procedures were performed in a cold room at 4 ℃.

2.3 SERS Experiments

2.3.1 General SERS experiment conditions

Two SERS spectrometers were involved in this work. They were a Renishaw inVia Raman spectrometer (Renishaw) and an Ocean Optics QE65 Pro spectrometer (Ocean Optics). Which one was used is stated specifically in each case. The Renishaw was built with a 785 nm diode laser with maximum 10 mW power and a 50 × Olympus Long Working Distance objective (NA = 0.45), to focus the laser onto

gold nanoparticles (NP) or cells. The Ocean Optics was equipped with a 785 nm laser with 350 mW power. All SERS spectra were processed using Origin Pro 8.1 software.

Aqueous suspensions of gold nanoshells (NS) (2×10^9 NS/ml, 3.3 pM) were purchased from Nanospectra Biosciences. NS were resonant at 780 nm and had a 125 nm silica core and a 25 nm thick gold shell. Aqueous suspensions of gold nanorods (NR) (7.96×10^{11} NR/ml, 1.32 nM) were purchased from Nanopartz Inc. NR were resonant at 780 nm and had a 10 nm axial diameter and a 38 nm length. Aqueous suspensions of gold nanocolloids (NC) (1.79×10^{11} NC/ml, 300 pM) were purchased from Sigma Aldrich. NC were resonant at 526 nm and had a 30 nm diameter.

2.3.2 Nanoparticles (NP) functionalisation

NS were functionalised by incubating with 1 mM solutions of AQ, NQ, SAQ and SNQ overnight. The solution of NQ was 9:1 water:EtOH while solutions of AQ, SAQ and SNQ were 99:1 water:DMSO. All NS were thoroughly washed twice with distilled water after functionalisation. NR and NS were incubated with 1mM 4-(bromotriphenyl-λ^5-phosphanyl)butane-1-thiol (thiol-*triphenylphosphine*) in water for 48 h. NR and NC were washed three times with distilled water after functionalisation. UV-Vis and SERS spectra were collected to check the functionalisation.

2.3.3 Spectroelectrochemistry

2.3.3.1 Potentiostat spectroelectrochemistry

Two kinds of working electrodes were used in this work: microfabricated electrodes, purchased from Scottish Microelectronic Centre, and self-fabricated gold-coated glass slides. Normal glass slides (76 mm × 26 mm, 1.0–1.2 mm thick, Thermo Scientific) were shaped into small pieces (~12 mm × 26 mm) using a diamond pen. The surface of these glass pieces was immersed in potassium hydroxide-saturated ethanol solution overnight for thorough cleaning. These glass pieces were then rinsed with ethanol and distilled water and allowed to dry under nitrogen. A layer of chromium (30 nm) and a layer of gold (150 nm) were coated onto the glass surface by sputter deposition. The gold-coated glass pieces served as working electrodes. Which type of the electrode was used will be specified.

Before functionalisation with the probe molecules, both the microelectrodes and the gold-coated glass pieces were carefully rinsed three times with acetone, ethanol and water and allowed to dry under nitrogen. 3 µl of Poly-L-lysine solution (0.1% w/v in PBS buffer) was deposited onto the electrode surface, which was incubated for 2 h at r.t. After this time, the electrodes were carefully rinsed with water and left to dry under nitrogen. 5 µl NS solution were deposited onto the electrodes and allowed to dry at r.t. Loose NS, which were not attached to the electrode, were washed off with water. A 10 µl solution of the probe molecules (1 mM) were deposited over the NS and incubated overnight in the dark. Electrodes were carefully rinsed with water to remove loosely adsorbed probe molecules and left to dry at r.t.

The electrodes were encapsulated within a superstructure (made of silicone) (Figure

2.1), which was sealed with the Araldite® glue and mounted on a glass slide. Only a very small area of the functionalised surface was exposed and the majority of the electrode surface within the superstructure was covered by the Araldite® glue. (See Figure 2.1)

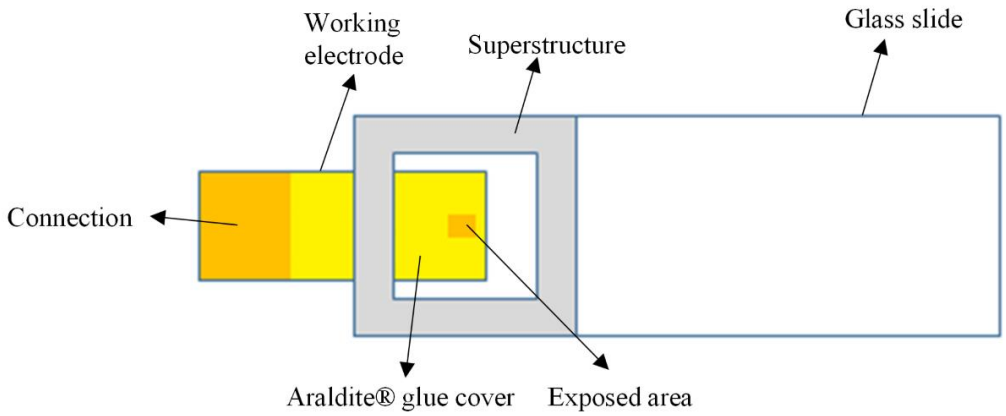

Figure 2.1 Structure of the spectroelectrochemical system

A coiled platinum wire (0.5 mm diameter), serving as the auxiliary electrode and a coiled silver wire (0.5 mm diameter) coated with silver chloride, serving as the reference electrode, were inserted into the space provided by the superstructure, which was charged with PBS (0.1 M, pH 7.2), to form a three electrode system. These electrodes were connected to a μAUTOLAB Type III potentiostat, using NOVA 1.9 software to control the potential. The pseudoreference electrode was calibrated using potassium ferricyanide and measured to have a potential of 291 mV *vs* NHE. All measured values are quoted *vs* NHE for consistency. SERS spectra were recorded on the Renishaw spectrometer at varying potentials by focusing the laser on an appropriate NS aggregate for 30s using a 785 nm diode laser with 1 mW power over a Stokes Raman shift range of 400-1800 cm^{-1}. While working with the Ocean

Optics spectrometer, spectra were collected from the electrode surface for 10s with a 350 mW laser over a Stokes Raman shift range of 0-2000 cm^{-1}.

2.3.3.2 Redox couple solution spectroelectrochemistry

3 µl Poly-L-lysine solution (0.1% (w/v) in PBS) was deposited on the Quartz glass slide, which was incubated for 2 h at r.t. The glass slides were then carefully rinsed with water and left to dry under nitrogen. 5 µl NS solution were deposited onto the glass slide surface and allowed to dry at r.t. Loose NS, which were not able to attach to the glass, were washed off with water. A 10 µl solution of the probe molecules (1 mM) were deposited over the NS and incubated overnight in the dark. The glass slides were carefully rinsed with water to remove loosely adsorbed probe molecules and left to dry at r.t. Potentials were changed by altering the concentrations of oxidised and reduced species of redox couples (See Tables 2.2 and 2.3). Tris buffer was used to make up the GSH/GSSG solution while PBS was the buffer for the Cystine/Cysteine solution. The potential was calculated based on the Nernst equation at pH 7.2.[56] 50 µl redox solution were deposited on the nanosensors and a cover slip covered the solution to block the air and also even the solution. SERS spectra were recorded after 2 min of equilibration on the Renishaw spectrometer by focusing the laser on an appropriate NS aggregation for 30 s using a 785 nm diode laser with 1 mW power over a Stokes Raman shift range of 1400-1800 cm^{-1}. When using the Ocean Optics spectrometer, spectra were collected from the glass surface for 10 s with a 350 mW laser over a Stokes Raman shift range of 0-2000 cm^{-1}.

Table 2.2 Solution potentials provided by different concentrations of GSH and GSSG at pH 7.2

GSH/ M	GSSG/ M	POTENTIAL/ mV
0.0016	0.01	-146
0.0032	0.01	-162
0.0047	0.01	-174
0.0047	0.005	-183
0.0095	0.01	-192
0.0158	0.01	-204
0.0221	0.01	-213
0.0316	0.01	-222
0.0316	0.005	-231
0.0632	0.01	-240
0.0949	0.01	-251

Table 2.3 solution potentials provided by different concentrations of Cystine and Cysteine

Cys/ M	Cyss/ M	POTENTIAL/ mV
0.003162278	0.01	-150
0.004743416	0.01	-162
0.004743416	0.005	-171
0.009486833	0.01	-180
0.015811388	0.01	-192
0.022135944	0.01	-201
0.031622777	0.01	-210
0.031622777	0.005	-219
0.063245553	0.01	-228
0.09486833	0.01	-239
0.09486833	0.005	-249

2.3.4 Intracellular SERS measurements

200,000 cells were seeded on 25 × 25 × 1 mm quartz coverslips (UQG Optics Ltd, UK) and incubated for 24 h at 37℃ and 5% CO_2 in a humidified incubator. Nanosensors were added to serum-free DMEM (to a final concentration of 10 fM) and incubated with cells overnight. In order to induce hypoxia, $CoCl_2$ solution was added to the media at a final concentration of 100 μM and maintained in a 5% CO_2 atmosphere at 37℃. SERS measurements were made after 3 h, 6 h and overnight. In order to induce oxidative stress, 2,2'-Azobis(2-amidinopropane) dihydrochloride

(AAPH) was added to the media at a concentration of 30 mM and SERS measurements were taken after 30 min. The position of NS was determined by collecting maps of Raman spectra using raster scans (785 nm laser with 5 mW power for 2 seconds) in 5 μm steps over cells with a computer-controlled xy-stage to find the approximate position of the NS in cells and further measurements (785 nm laser with 1 mW power for 30 seconds) were also performed as raster scans in 1 μm steps over a smaller area to determine the precise location. Spectra were then recorded for 30 s between a Stokes Raman shift range of 1400–1800 cm^{-1}. All spectra were processed using OriginPro 8.1.

2.4 Other experimental techniques

2.4.1 Cyclic voltammetry

Cyclic voltammograms (CVs) were carried out with a PGSTAT128N potentiostat controlled by GPES v4.9. All results were analysed using Origin Pro 8.1. A gold disc electrode (7.07 mm^2, Metrohm) was used as a working electrode, along with platinum gauze (Sigma Aldrich) serving as the auxiliary electrode and a Saturated calomel electrode serving as the pseudo-reference electrode. In order to clean the electrode, it was first ground on Trident polishing cloths (Buehler) with Micropolish Alumina powder (1 μm, Buehler), rinsed with distilled water and then left in water for sonication for 30 min. This procedure was then repeated with 0.3 μm Micropolish Alumina powder. The clean electrode was immersed into a solution of probe molecules (1 mM in DMSO) overnight for functionalisation. Before CV measurements, the electrode was carefully rinsed with water. A conventional three-electrode cell was used and charged with PBS (0.1 M, pH 7.2). At least 5 scans were recorded at each scan rate. All buffers were degassed by nitrogen bubbling for 2 h.

2.4.2 Intracellular pH measurements using BCECF, AM

Measurements of fluorescence intensity of BCECF (Molecular Probes, Life Technologies) were carried out using a spectrofluorometer (FluoMax-1) with excitation wavelength pairs of 490/440 nm. Slit width settings were 5 nm for both excitation and emission. The pH-dependent ratio of the emitted fluorescence intensity at 535 nm excited by 490 nm and 440 nm, respectively, was used to obtain the pH.

25,000 cells were seeded on ø 13 mm coverslips (VWR) and incubated for 24 h at 37 ℃ and 5% CO_2 in a humidified incubator. Functionalised AQ-NS were added to CS-free DMEM (to a final concentration of 10 fM) and incubated with cells overnight. In order to induce hypoxia, cobalt chloride solution was added to the media at a final concentration of 100 μM and maintained in a 5% CO_2 atmosphere at 37 ℃ for different lengths of time as required. Cells were thoroughly washed with PBS before loading the fluorescent dye. Cells were incubated with 5μM BCECF, AM in HBSS for 20 min. At the end of dye loading, the coverslip was removed and washed with PBS and then placed diagonally in a 3 ml cuvette filled with HBSS, facing the exciting laser beam at a 45^{o} angle to record the spectra. 4 independent samples were measured for both the treated and untreated cell populations. After the last run of each cell population, 10 μM nigericin (Molecular Probes, Life Technologies) and 150 mM potassium ions were added to the buffer immediately following the pH_i measurements to equilibrate the extracellular and intracellular pH and the spectra were re-collected after 5 min. The pH of HBSS was 7.60.

In situ calibration of fluorescence ratio to pH_i was performed using untreated cells prepared as above. 10 μM nigericin (Molecular Probes, Life Technologies) and 150

mM potassium ions were added to the buffer at various external pHs between 6.5 and 8.8.

2.4.3 UV-Vis spectroscopy

Solutions containing NS, NR, NC, probe-functionalised NS and SBTPP-functionalised SBTPP were measured in a Varian Cary 50 scan UV-Vis spectrophotometer. The solutions were loaded in a 70 µl cuvette and the spectra recorded from 300 to 1000 nm.

2.4.4 DFT calculations

The Raman-active vibrational modes of the oxidised and reduced probe molecules were calculated using DFT at the B3LYP/6-31G(d) level of theory. These calculations were carried out using Becke's three-parameter exchange functional, coupled with the Lee-Yang-Parr correlation functional (B3LYP),[2,3] in combination with the 6-31G(d) basis set. The possible intermediate forms, semi-quinone, between the oxidised and reduced species were also investigated using DFT at the UB3LYP/6-31G(d) level. Because the unpaired electron exists in the structures of the semi-quinone, these calculations were performed using unrestricted Becke's three-parameter exchange functional. Molecular structures were firstly drawn and preliminarily optimised with Avogadro v.1.1.0. Also with Avogadro, the input file for Gaussian 03 software, which contained the coordinates of the atoms in the molecule, was generated. All calculations were carried out using the Gaussian 03 software package.

Vibrational mode assignments were based on visual inspection of the calculated modes, which were animated using the Gaussum 3.0 and Gnuplot 4.6.

Chapter 3 Fabrication and characterisation of nanosensors

3.1 Introduction

This chapter aims to synthesise and characterise redox-sensitive quinone compounds which can be used to expand the potential detection range and also construct calibration curves using spectroelectrochemistry. As stated in Chapter 1, previous work in our group has established a sophisticated SERS-based system for quantifiably monitoring intracellular redox potentials. Two quinone compounds were synthesised as probe molecules in previous work, one of which is HQ, responsible for measuring supraphysiological oxidative stress in cells, and the other is NQ, suitable for recording physiological cellular redox potentials. Quinone molecules are redox sensitive and their structures can change with varying potentials, thus leading to corresponding changes in the fingerprints of their SERS spectra. Furthermore, the modification of the cystamine group can potentially allow the molecules to be vertically attached to the surface of gold nanoshells and therefore enhance the SERS signals. It is also worthwhile to note that HQ and NQ are simple organic quinone molecules, so we can easily modify their structures to tune mid-point potentials. For example, the presence of electron-withdrawing groups (such as nitro or sulfonyl groups) on the aromatic rings can lead to less electron density within the molecule and thus stabilise the reduced states, making the redox potential more positive (compared to the unsubstituted molecule).

3.2 Synthesis and electrochemical characterisation of Nanosensors

3.2.1 Synthesis and electrochemical characterisation of AQ

9.10-anthraquinone-2-carboxylic acid was first reacted with thionyl chloride to convert the carboxyl group to a more reactive acyl chloride group. This step aimed to ensure a more efficient reaction with Cystamine to form the amide bond. After the first step, the acyl carbonyl carbon of the resultant 9.10-anthraquinone-2-carbonyl chloride was attacked by the nucleophilic amine group of Cystamine to yield the resultant deep red solid (see Scheme 3.1)..[91] The yield was 84%.

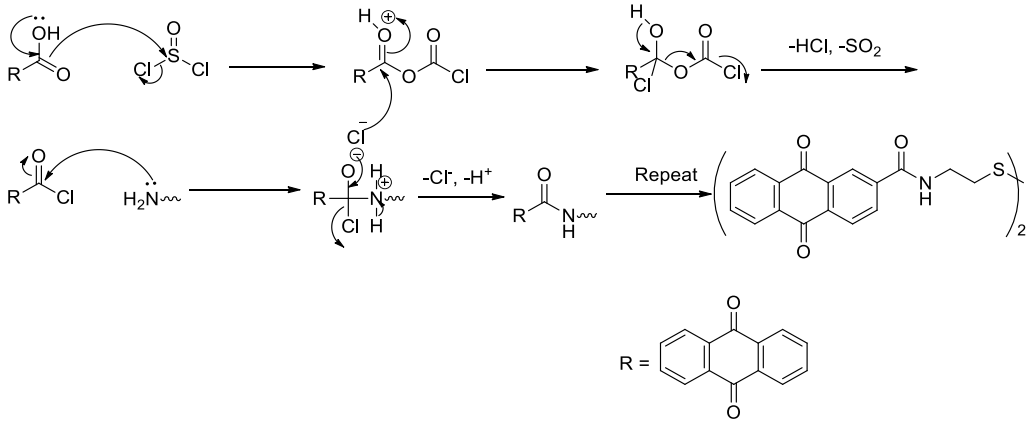

Scheme 3.1 Mechanism of AQ synthesis

In order to monitor redox changes, the probe molecule must be electrochemically reversible. The electrochemical reversibility was first investigated as a prerequisite by cyclic voltammetry. Ideally, in terms of the theoretical conditions where the electrochemical reaction is only controlled by electron transfer kinetics and electron transfer is fast enough, a CV of surface-adsorbed molecules should show symmetric reduction and oxidation peaks and the peak currents should be approximately 1.

Furthermore, the plots of oxidation currents against the corresponding scan rates should be linear. [93]

However, in the case of AQ, its CV did not display ideal electrochemical reversibility and a separation between oxidation and reduction peaks was observed whether at high scan rates or low scan rates (Figure 3.1). The oxidation peak currents increased linearly with scan rates (Figure 3.2). This indicates that the AQ molecules were surface-confined and were adsorbed on the surface of the gold electrode. The observed separation between the oxidation and reduction peaks suggested that electron transfer between AQ molecules and the electrode surface is slow. Literature related to redox chemistry on the electrode surface suggested that the slow electron transfer rate is mainly caused by the formation of multilayers, making it hard for the electrons to reach the outer layer of the adsorbed molecules.[94] On the other hand, the reaction rate could also be hindered by the diffusion of H^+, due to the low concentration of H^+ (3.98×10^{-8} M, pH 7.2). While these two factors both lead to the separation of the oxidation and reduction peaks, making the electrochemical reaction quasi-reversible, the CV of AQ still showed a chemically reversible electrochemical process which demonstrated its potential utility for monitoring both oxidative and reductive changes. Indeed, this is the case for all of the redox probe molecules in the following parts.

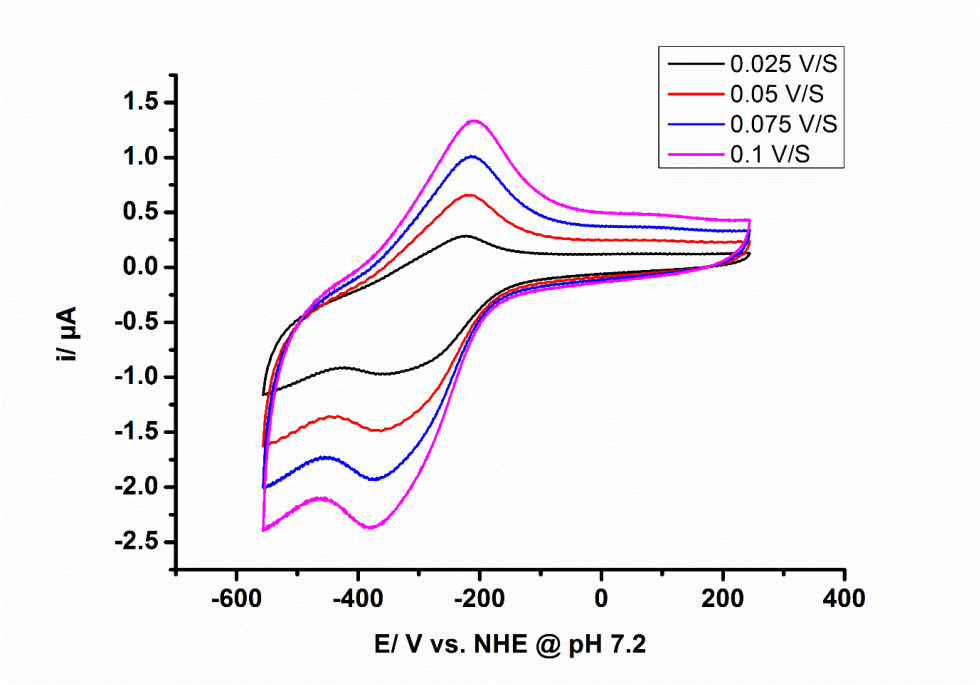

Figure 3.1 CV of AQ on a gold disc electrode in PBS at pH 7.2 at various scan rates from 0.025 V/S to 0.1 V/S.

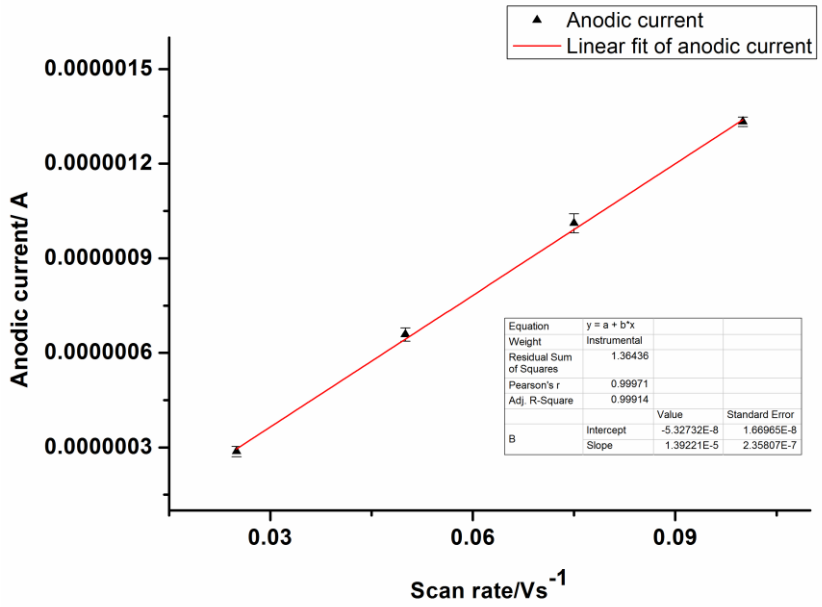

Figure 3.2 Oxidation peak currents plot against scan rates. Error bars represent the standard deviation of 5 consecutive scans.

3.2.2 Synthesis and electrochemical characterisation of NQ

NQ was made via a previously published substitution reaction[78]. The 2-position of 2,3-dichloro-1,4-naphthoquinone was attacked by the nucleophilic amine group of Cystamine and the chlorine was then substituted by the amine.. (Scheme 3.2)

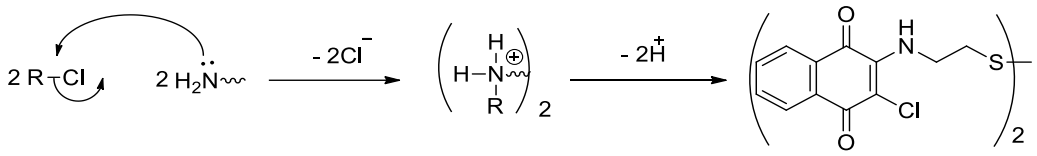

Scheme 3.2 Mechanism of NQ synthesis

Electrochemical reversibility was investigated and the mid-point potential of NQ was measured by cyclic voltammetry (Figure 3.3).

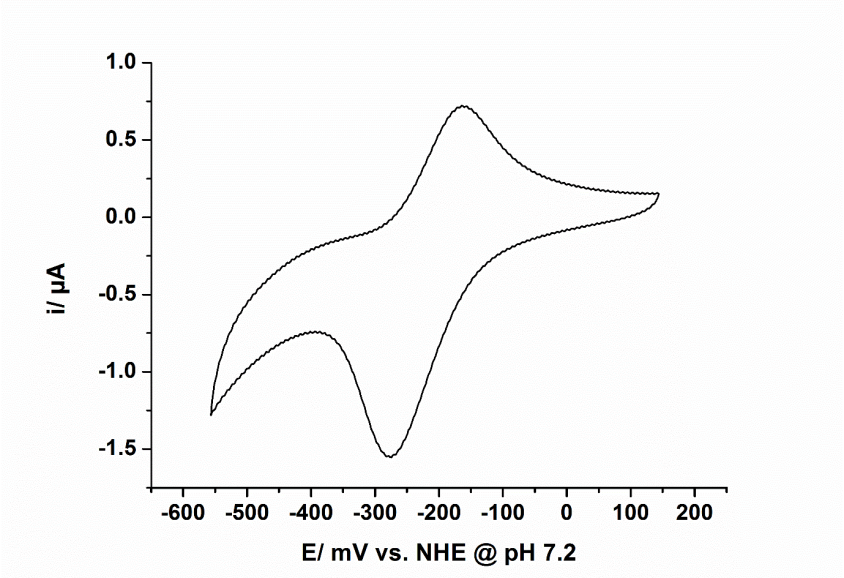

Figure 3.3 CV of NQ on a gold disc electrode. Scan rate = 0.025 V/s

As expected, there was also a separation between the reduction and oxidation peaks and ideal electrochemical reversibility was not observed here either. However, as stated in section 3.2.1, the results here are in good agreement with the findings of AQ. The CV of NQ revealed a half-wave potential of -218 mV $\pm$ 3 mV.

3.2.3 Synthesis and electrochemical characterisation of NNQ

In order to expand the measuring range of our technique for covering the gap between NQ and HQ, the first thought was to nitrate NQ to shift its potential in the anodic direction. The nitro group is a strongly electron withdrawing group which can decrease the electron density on the aromatic ring, thus making it easier to receive electrons and also helping stabilise the anion radical intermediate.

The two-step synthesis of Nitro-NQ firstly included a nitration reaction of 2,3-dichloro-1,4-naphthoquinone, which substituted the 5/6-position H with the nitro group (the 5-position substituent was the major product) (Scheme 3.3). In the second step, the resultant 2,3-dichloro-5-nitro-naphthoquinone was reacted with Cystamine to yield an orange solid. The mechanism of the first reaction is only presented here as the second step was the same as previous two synthesis processes.

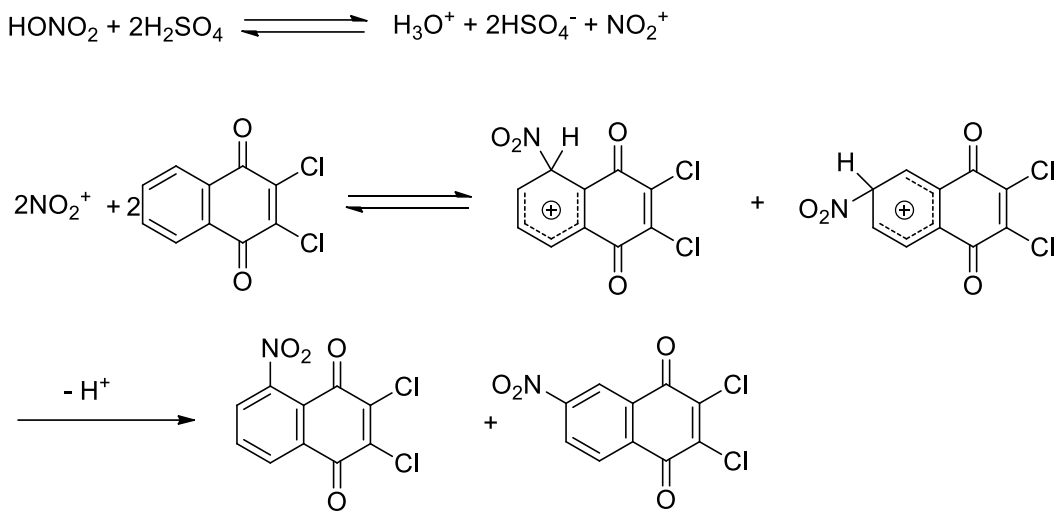

Scheme 3.3. Mechanism of the nitration of NQ

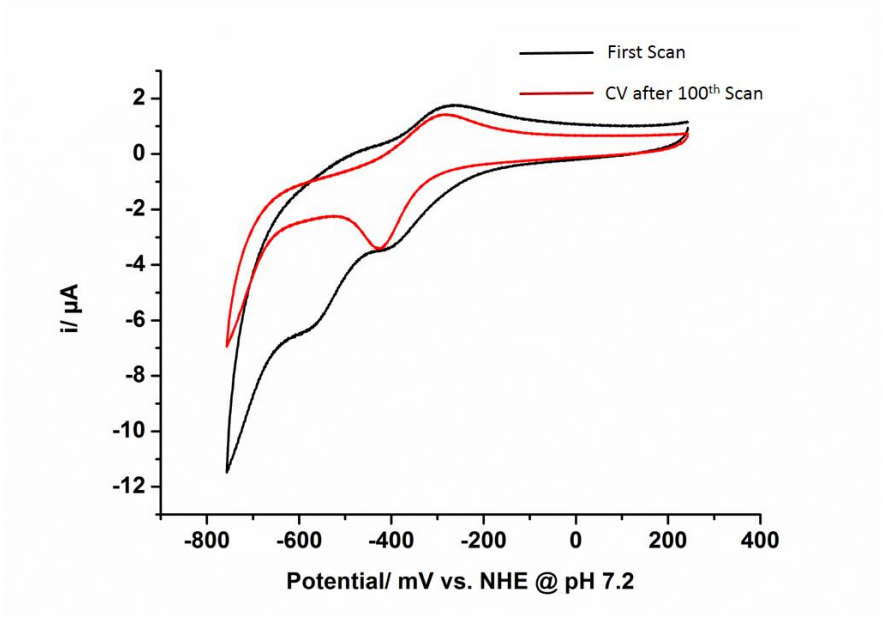

Figure 3.4 CV of NNQ on a gold disc electrode. Scan rate = 0.1 V/s

Figure 3.4 shows the CV of Nitro-NQ. Based on the two-electron/two-proton redox reaction (Figure 3.1), only one pair of peaks should be recorded, corresponding to the oxidation/reduction of the quinones. Interestingly the electrochemical behaviour is

different from that predicted. The CV from the first scan presented two reduction waves, one reduction peak at -0.389 V and a second wave at more reductive potential of -0.757 V. With an increasing number of the scans, the voltammogram eventually showed only one pair of peaks, giving a half-wave potential ($E_{1/2}$) of -0.334 V ± 0.005 V, which was lower than the $E_{1/2}$ of NQ. The aim of the synthesis of Nitro-NQ was to cover the gap between NQ and HQ, in which the potential window should be more positive than the NQ. And theoretically, the substitution of electron-withdrawing groups on the aromatic rings is able to alter the potential towards a more oxidative way. However, the findings showed that the half-wave potential of the resultant Nitro-NQ was more negative than that of the unsubstituted NQ.

One hypothesis is that the nitro group was irreversibly reduced to the amino group during the first couple of CV scans (Scheme 3.4).[95] As the amino group is electron-donating, making the quinone more electronegative can stabilise the oxidised form. Furthermore, the two reduction peaks observed on the first scan correspond support this hypothesis because the reduction process involved a series of intermediate states and products (Scheme 3.5)[95], which could be reflected in the CV by a series of oxidation peaks.

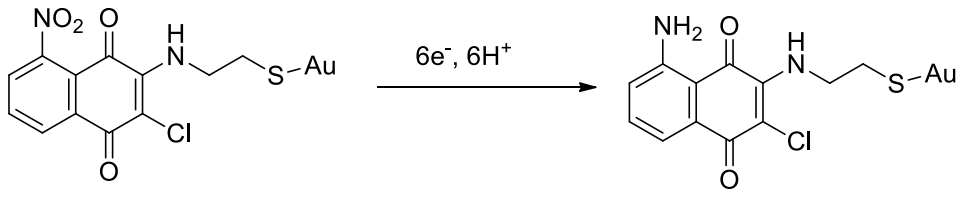

Scheme 3.4 Reduction the 5-nitro group

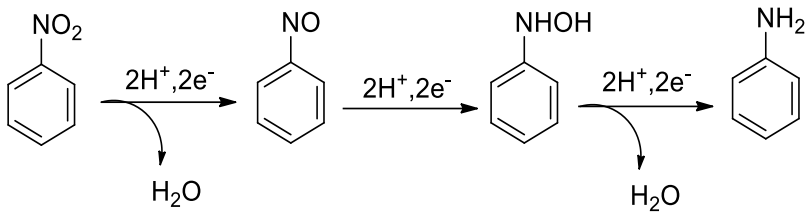

Scheme 3.5 Mechanism of the reduction process of the aromatic nitro group

While Nitro-NQ was not suitable to monitor redox changes, it is worth noting that the CV of Nitro-NQ suggested its reduction product could possibly serve as a sensor for measuring redox potentials which are more reductive than the range covered by NQ.

3.2.4 Synthesis and electrochemical characterization of SNQ

SNQ was synthesised through a two-step reaction. The first step involved the chlorosulfonation of the 2,3-dichloro-1,4-naphthoquinone, which substituted the 6-position H with the chlorosulfonyl group. During the second step, the resultant 2,3-dichloro-6-chlorosulfonyl-1,4-naphthoquinone was reacted with Cystamine to produce a brownish solid. As sulfonyl chloride is more active than the 2/3-position chlorine, the nucleophilic amine was more likely to react with the chlorine of the chlorosulfonic group. (Scheme 3.6)

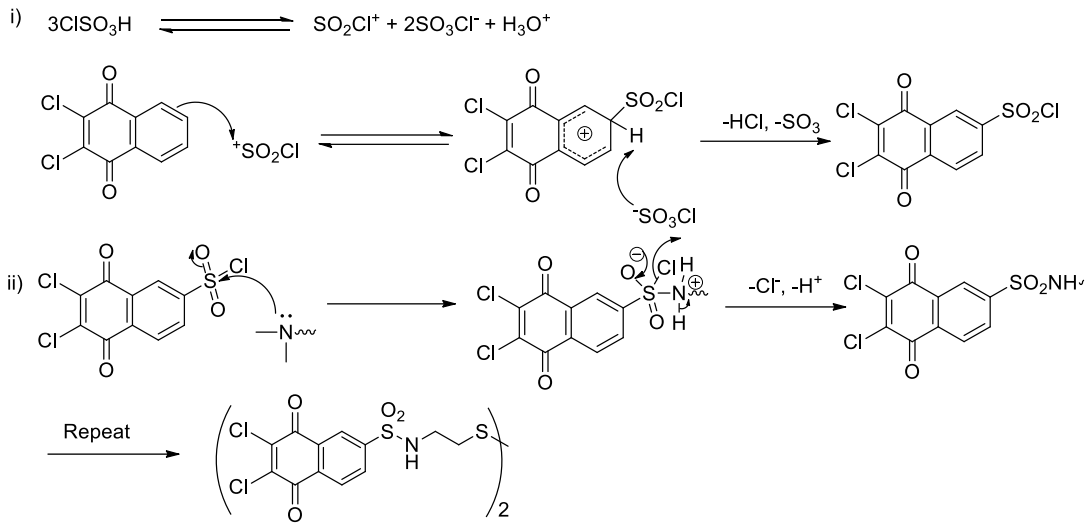

Scheme 3.6 Mechanism of SNQ synthesis

The CV of SNQ revealed a half-wave potential of -97 mV ± 2 mV at pH 7.2 which was more oxidative than NQ, suggesting SNQ would be potentially useful in recording more oxidative redox potentials. Furthermore, these findings also demonstrated that in terms of the ease to modify the structure of small organic molecules, it is likely to expand our technique to suit any potential range needed.

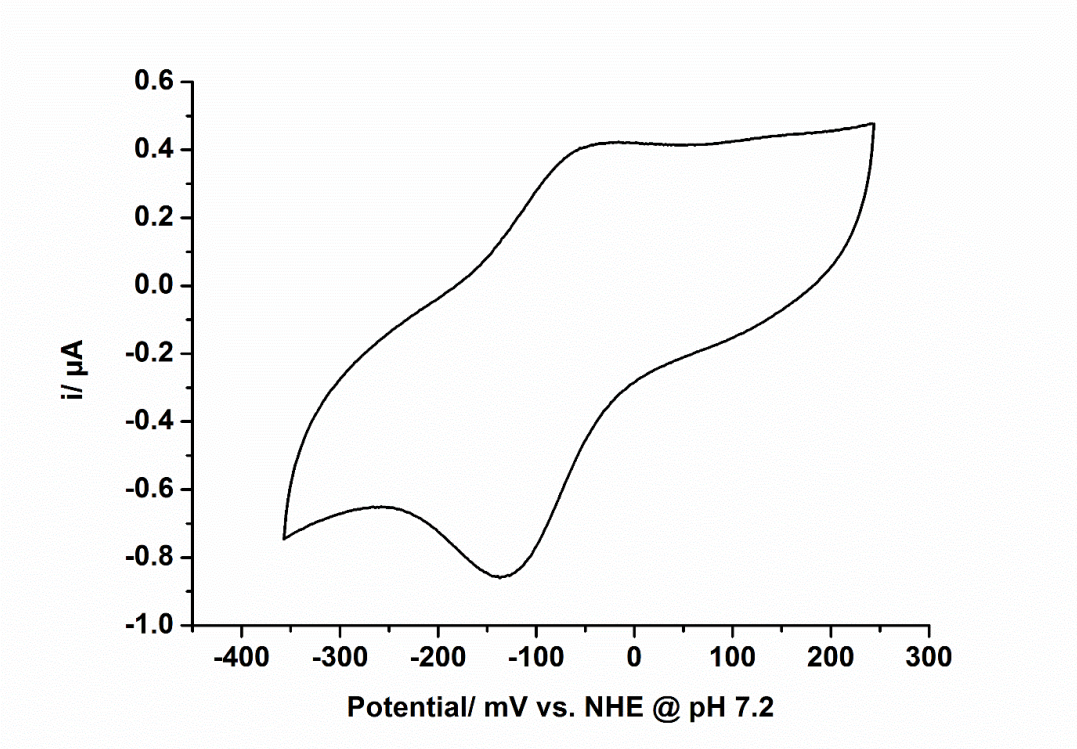

Figure 3.5 CV of SNQ on a gold disc electrode. Scan rate = 0.025 V/s

3.2.5 Synthesis and electrochemical characterisation of SAQ

After the successful synthesis and characterisation of SNQ, we naturally paid attention to the similar chlorosulfonation of AQ to yield SAQ, which was expected to be more oxidative than AQ. This synthesis also included two steps. 9,10-anthraquinone-2-sulfonic acid sodium salt was first reacted with thionyl chloride to convert the sulfonic group into sulfonic chloride which was more vulnerable to attack by the nucleophilic amine. The second reaction was the same as in the synthesis of SNQ, so only the mechanism of the first step is shown in Scheme 3.7.

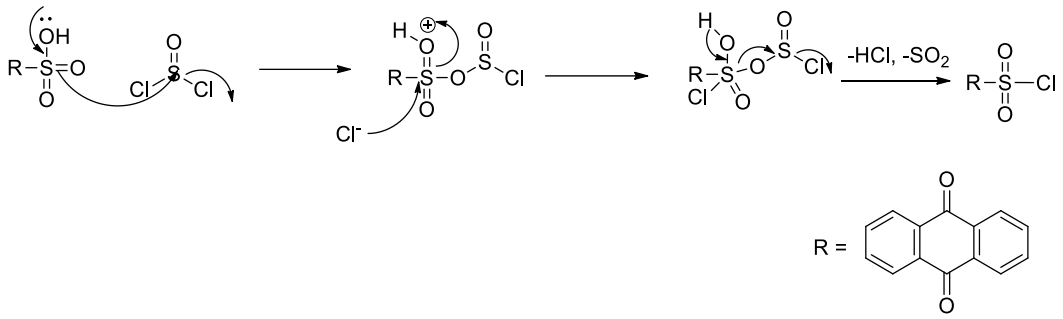

Scheme 3.7 Mechanism of SAQ synthesis

The electrochemical reversibility of SAQ and its half-wave potential was also investigated by CV (Figure 3.6). In the voltammogram, a separation between the oxidation and reduction peaks was recorded once again. However, further analysis of these CVs also confirmed the quasi-reversibility of SAQ and its use for monitoring redox potentials. The CV indicated a half-wave potential of -237 mV ± 4 mV.

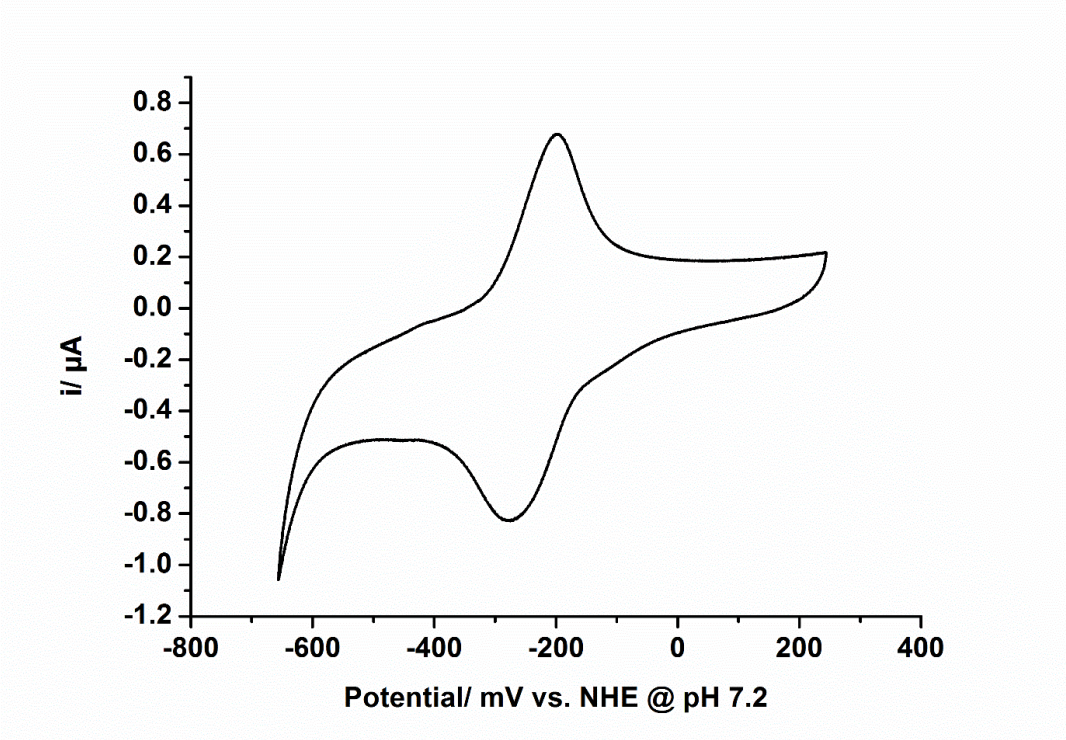

Figure 3.6 CV of SAQ on a gold disc electrode. Scan rate = 0.025 V/s

3.2.6 Electrochemical characterisation of HNQ

HNQ was synthesised by Dr. Patrick Thomson. As expected, there was also a separation between the reduction and oxidation peaks and ideal electrochemical reversibility was not observed here either. The CV indicated a half-wave potential of -245 mV ± 3 mV.

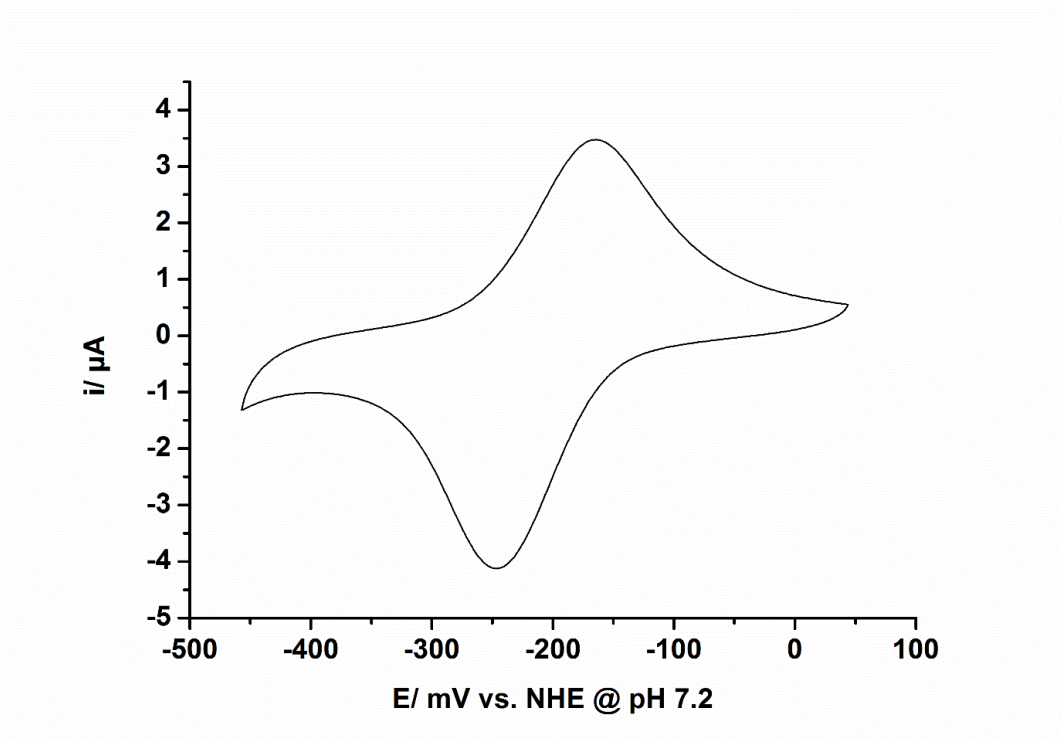

Figure 3.7 CV of HNQ on a gold disc electrode. Scan rate = 0.025 V/s

3.2.7 Electrochemical characterisation of ANQ

ANQ was synthesised by Dr. Patrick Thomson. The electrochemical reversibility of ANQ and its half-wave potential was also studied by CV (Figure 3.8). In the cyclic voltammogram, a separation between the oxidation and reduction peaks was again

recorded once. The half-wave potential of ANQ, determined by the CV, is -309 mV vs. NHE.

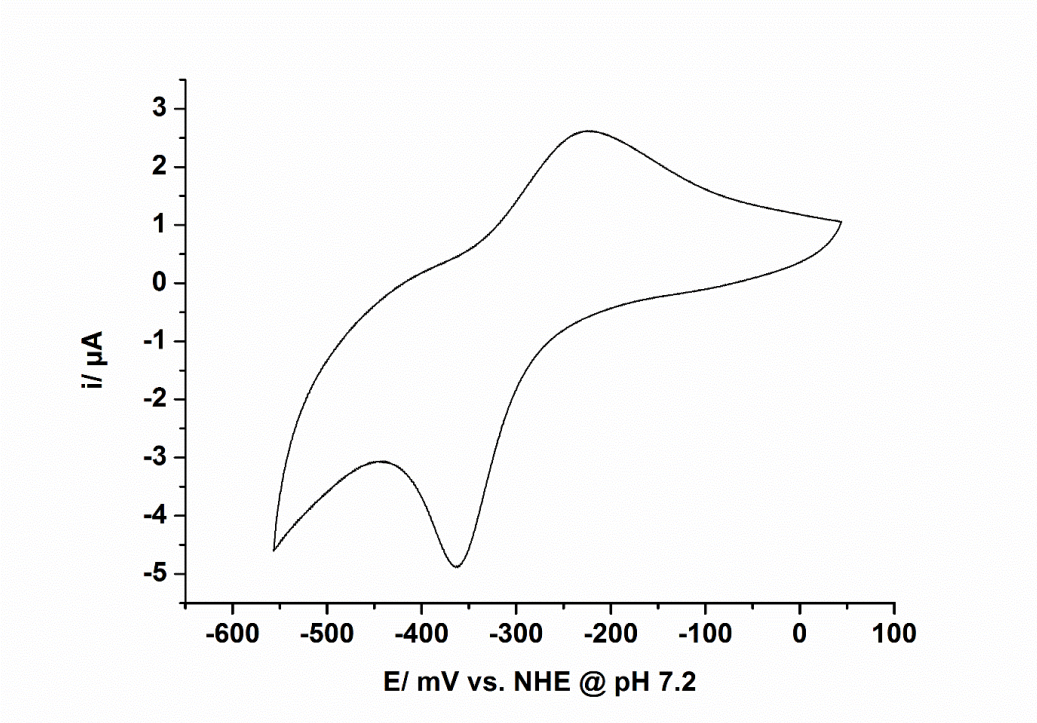

Figure 3.8 CV of ANQ on a gold disc electrode

3.2.8 Theoretical potential ranges

The results presented above demonstrate that through simple organic synthesis, we managed to build a library of redox-sensitive quinone compounds, which are able to cover various redox potential windows (Figure 3.9). Since the half-wave potential values of these probe molecules were determined by CV, we could generate the theoretical Nernstian plots by varying the ratio of reduced:oxidised species. These curves suggest the potential ranges which they could monitor in principle, but also guided us to focus the spectroelectrochemistry on specific ranges, centred on the

half-wave potentials of each probe molecule.

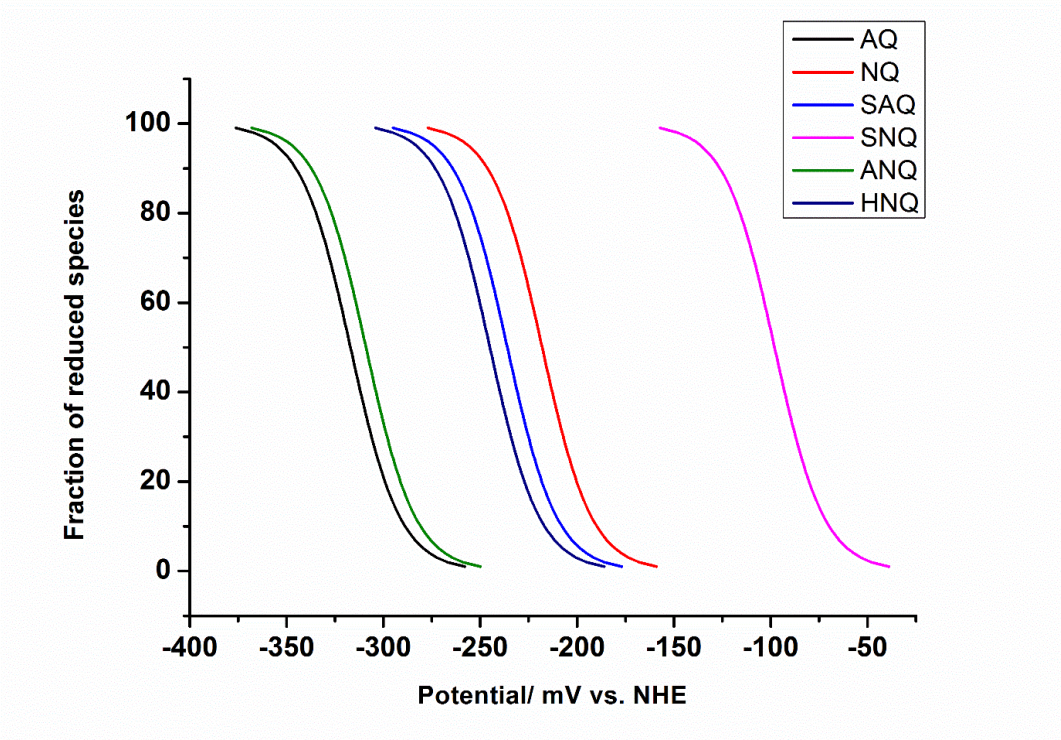

Figure 3.9 Theoretical potential windows of nanosensors as determined by the Nernst equation

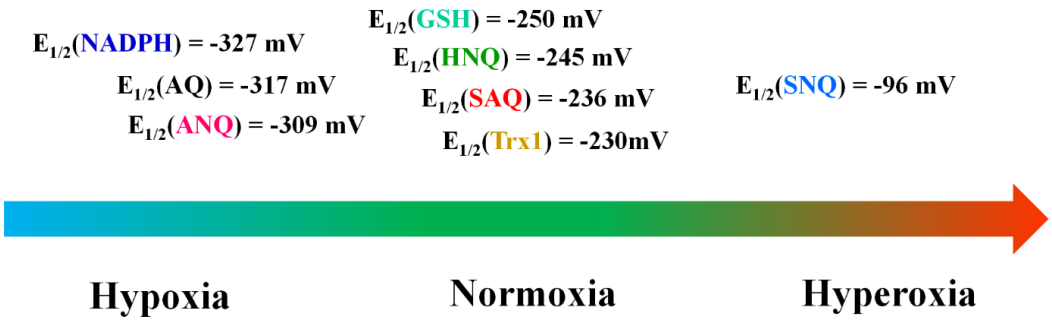

Figure 3.10 Summary of the half-wave potentials of all the probe molecules, along with the half-wave potentials of some abundant redox species in cells.

From Figure 3.9, we can also see the Nernstian plots of several abundant redox species in cells including GSH, NADPH and Trx1[11]. It is worth noting that the half-wave potentials of HNQ and SAQ are similar to that of GSH and Trx1, which means HNQ and SAQ would be suitable for monitoring the redox potentials in cellular normoxia. AQ and ANQ, with their more negative half-wave potentials, which are similar to that of NADPH, would be useful for detecting the redox changes in cellular hypoxia. SNQ, on the other hand, could potentially cover the gap between NQ and HQ to record the events and processes associated with cellular oxidative stress and also optimise our technique.

3.3 SERS spectroelectrochemistry and DFT calculations

In order to link the SERS fingerprints of the probe molecules with redox changes, SERS spectroelectrochemistry was employed to investigate the spectral behaviours at different potentials. A three-electrode system was employed to perform the SERS spectroelectrochemistry (please see Chapter 2.3.3 for the detailed set-up of electrochemical system). The nanosensors were firstly immobilised on the surface of working electrodes. There were two types of working electrodes involved in these experiments. Microfabricated gold electrodes were initially utilised to serve as working electrodes for controlling the potential. The calibration work of AQ and SAQ was performed on this type of electrode. However, the quality of these microfabricated electrodes was found to be inconsistent. Thus after the completion of the spectroelectrochemistry of AQ and SAQ on the Renishaw spectrometer, instead of continuing to use the microfabricated electrodes, we crafted a simple device by sputtering a gold coating on re-shaped glass slides (Figure 2.1). These gold-coated glass slides were masked by Araldite® glue to provide only a very small exposed area

as the working surface. The masked gold-coated glass slide then took the place of the working electrodes in the following calibration work performed on the Ocean Optics spectrometer. A silver wire with a coating of silver chloride and a platinum wire served as the reference electrode and the counter electrode respectively. The potential applied on the working electrode was varied using a potentiostat and this electrochemical system was immobilised under the laser to collect SERS spectra.

To fix the nanosensors onto the gold electrodes, a drop of poly-L-lysine solution was deposited on the electrode surface. This poly-L-lysine coating could allow the NS to bind to the electrode surface via formation of coordinate complexes between gold and poly-L-lysine.[96] (Figure 3.11). In order to study whether the poly-L-lysine coating would influence the electrochemical pattern of the probe molecules, a gold disc electrode was functionalised with poly-L-lysine and the CVs were run in PBS with 10 mM potassium ferricyanide at pH 7.2 (Figure 3.12). The mid-point potential of potassium ferricyanide, from the CV, was found to be 365 mV, which correlated well with the literature value. For further investigation into the potential effect of poly-L-lysine on the probe molecules, the poly-L-lysine-functionalised gold electrode was then immersed in AQ solution overnight to allow the formation of the same poly-L-lysine/AQ layers as on the gold-coated electrodes. The CVs of the double layers were run in PBS at pH 7.2 (Figure 3.13). As expected, the half-wave potential of AQ in this case was identical to the value obtained from direct functionalisation onto the disc electrode. The electrochemical reversibility was also consistent with the result in Figure 3.1. So the two experiments both confirmed that poly-L-lysine did not affect the electrochemical behaviour of the molecules

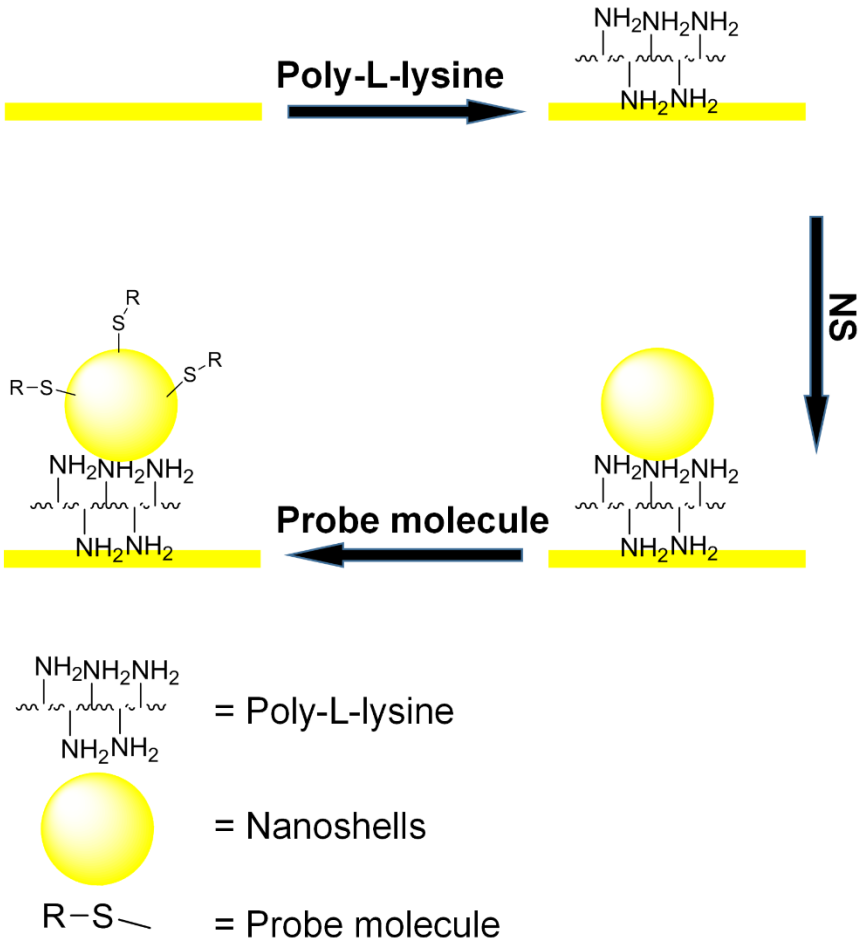

Figure 3.11 Scheme of the fabrication of the electrodes for spectroelectrochemsitry

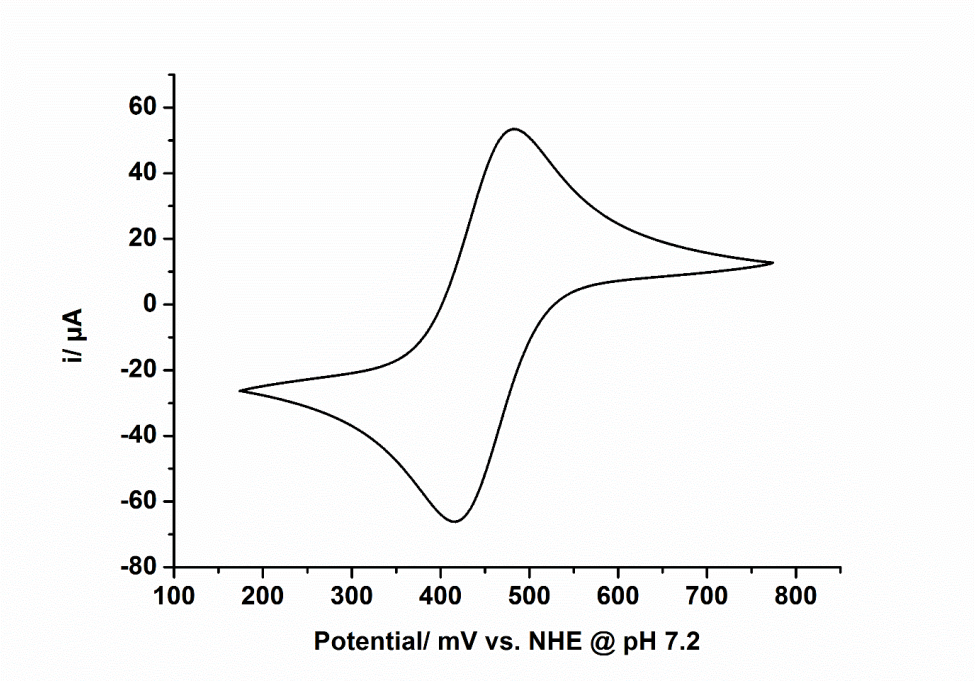

Figure 3.12 CV of Ferricyanide on a poly-L-lysine coated gold disc electrode. Scan rate = 0.025 V/s

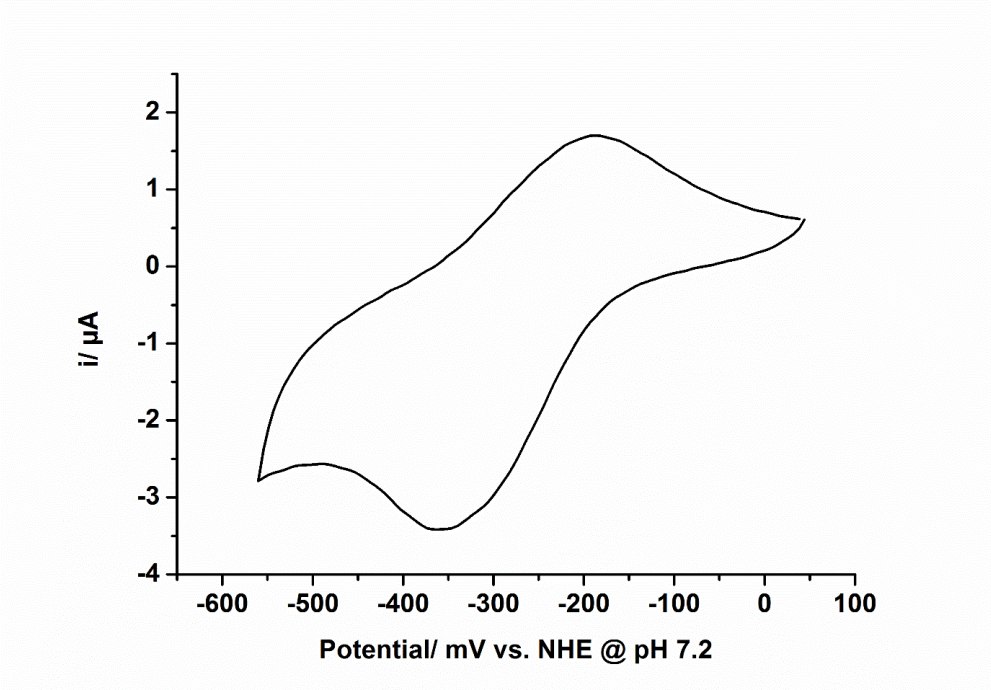

Figure 3.13 CV of AQ on a poly-L-lysine coated gold disc electrode. Scan rate = 0.025 V/s

Using a potentiostat, the potential was varied and SERS spectra were recorded by focusing the laser on either a single aggregate of nanosensors when using the Renishaw spectrometer or a small area of the functionalised electrode surface when using the Ocean Optics spectrometer to determine whether the changes in potential could be quantifiably linked with changes in the SERS fingerprints of the probe molecule. Calculated spectra generated by DFT can help verify these spectra and also assign the observed peaks to specific vibrational modes.

When performing the spectroelectrochemistry, a AgCl/Ag wire served as the reference electrode. Its potential was determined by running a CV of potassium ferricyanide using the same electrochemical system as for spectroelectrochemistry (Figure 3.14). Since the half-wave potential of potassium ferricyanide was known, after subtracting the half-wave potential obtained in the CV, we could calculate the potential of the AgCl/Ag wire. This process was performed before every measurement to ensure the accuracy of the reference potential. For example, the half-wave potential of potassium ferricyanide in Figure 3.14 is 105 mV vs. the AgCl/Ag wire, whereas its real half-wave potential vs. NHE is 360 mV; therefore in this case the pseudo-reference potential of this wire is 255 mV.

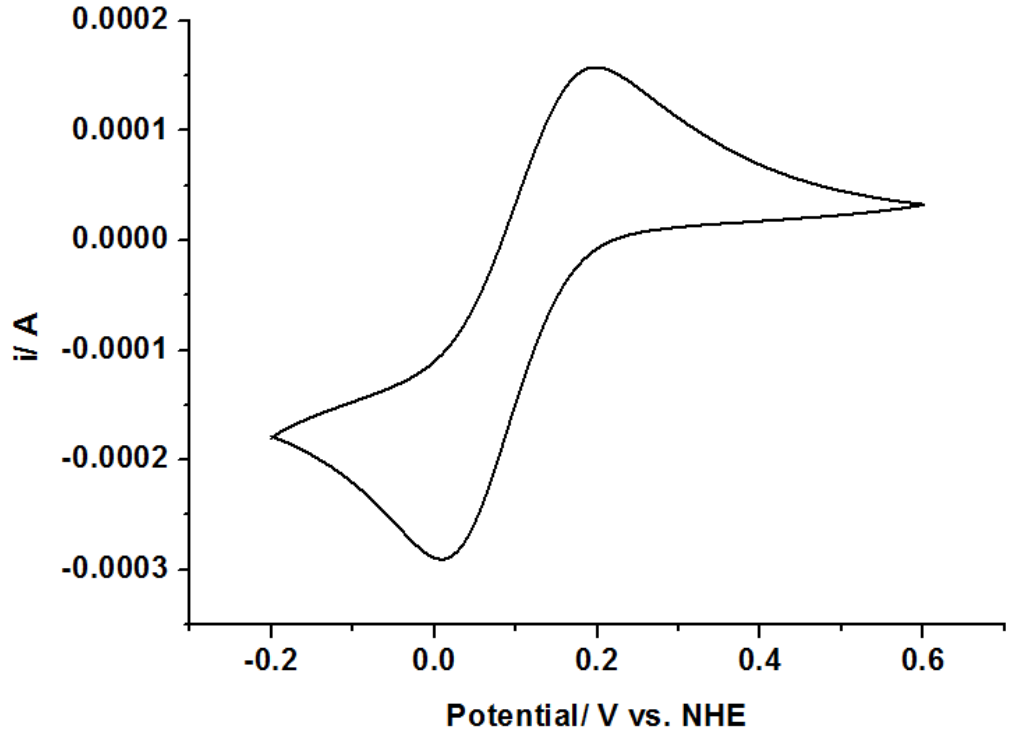

Figure 3.14 CV of potassium ferricyanide using AgCl/Ag wire as a reference electrode. Scan rate = 0.025 V/s

3.3.1 Spectroelectrochemistry of AQ and DFT calculations

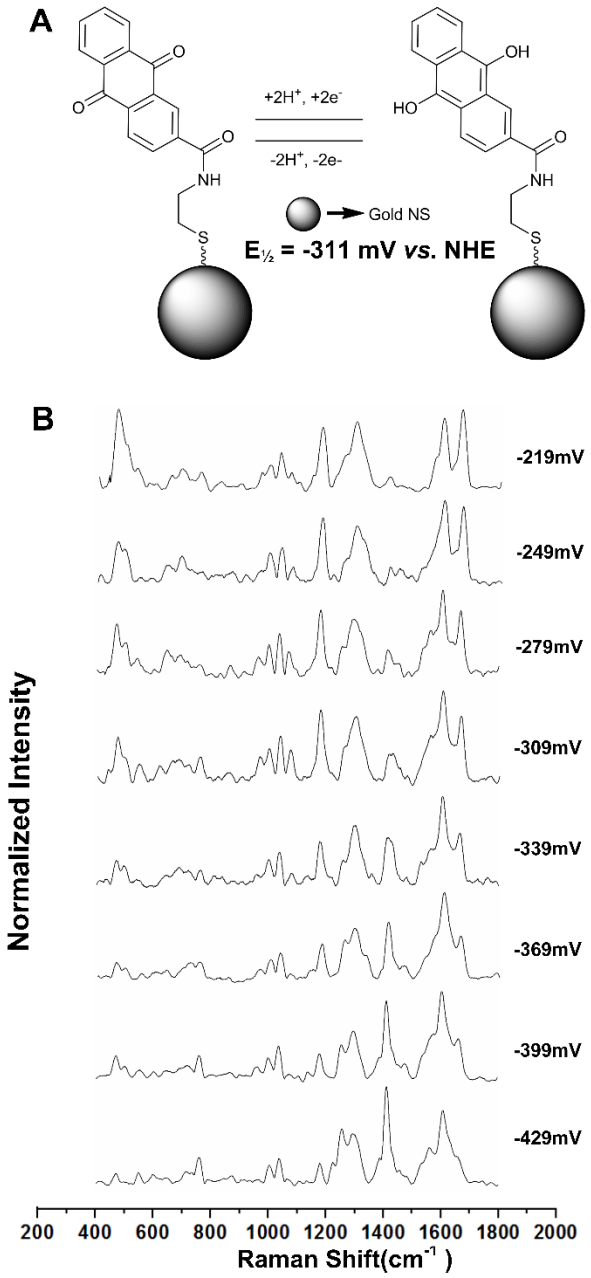

Figure 3.15 A: Structures, electron transfer schemes and standard reduction potentials. B: Potential-dependent changes of AQ in SERS spectra. (Spectra were collected by focusing the laser on an appropriate NS aggregate for 30s using a 785

nm diode laser with 1 mW power. Baselines were corrected manually by choosing 8 points on the spectrum using Origin Pro 8.1)

Figure 3.15 shows the structures, electron transfer schemes and mid-point potential of AQ along with the SERS spectra of AQ at different potentials from -219 to -429 mV which were obtained on the Renishaw spectrometer. DFT calculated the vibrations of a single molecule in *vacuo* with no interactions from other molecules or media. Compared to the predicted spectra by DFT calculations, both the spectra of the reduced and the oxidised species were in excellent correlation with the observed spectra (Figure 3.16). The assignments and positions of peaks in DFT calculations can be found in Table 3.1 and 3.2, which well match the observed spectra. For example, as expected, several spectral features change as a function of potential including the in-plane aromatic C-H wagging at 1180 cm^{-1}, the aromatic C-C stretching at 1405 cm^{-1}, and the quinone C=O stretching at 1666 cm^{-1}. In choosing a peak to use for quantification of redox potential, it is worth bearing in mind that the peak at 1405 cm^{-1} is near the background peak of silica which is often present in spectra measured from glass substrates, whereas the peak at 1666 cm^{-1} is less likely to suffer from background interference. Since the intensity of C=O stretching peak at 1666 cm^{-1} varies with potential while the C=C stretching peak at 1606 cm^{-1} stays constant (as shown in Figure 15B), we divided the peak intensity at 1666 cm^{-1} by the peak intensity at 1606 cm^{-1} to give a measure of the fraction of molecules which are oxidised. By setting the fully oxidised value to 1 and the fully reduced value to 0 we can plot the fraction of the oxidised AQ against potential to construct the calibration curve (Figure 3.17). Theoretically, this curve should fit the Nernstian plots but in fact it is more spread out and covers a broader potential range. However, it is worth bearing in mind that the Nernst equation describes an ideal redox reaction occurring in solution, whereas our reporter molecules are chemically adsorbed onto the surface

of NS. As a result of surface confinement and the hydrophobicity of the organic probe molecule, the interface between the molecule and aqueous solution might slow down either electron transfer or proton transfer, making AQ-NS behave differently from the ideal scenario. However, it can be seen that the midpoint potential of the calibration curve correlates well with half-wave potential, and the repeatability of the spectroelectrochemistry demonstrates that SERS spectra can be used to report on potential. Furthermore, when we look at other SERS measuring systems such as SERS pH sensors which share similar constraints to our probes, their measuring ranges are often more stretched than theory would dictate (determined by the Henderson-Hasselbach equation).

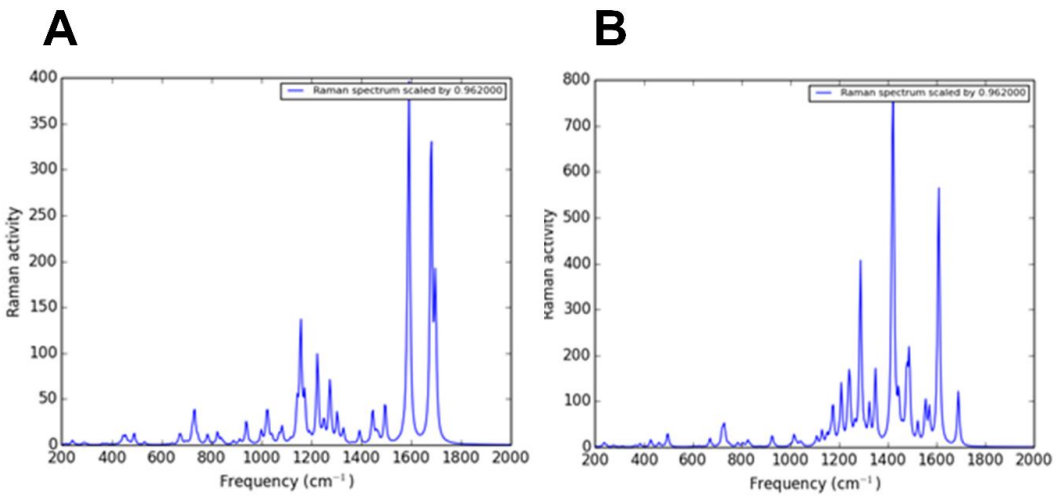

Figure 3.16 Predicted spectra of AQ by DFT calculations: A: Predicted spectra of oxidised AQ B: predicted spectra of reduced AQ (See Table 3.1 and Table 3.2 for the tabulated frequencies and their corresponding vibrational modes)

Table 3.1 Vibrational assignments of oxidised AQ

Raman shift/ cm^{-1}	Assignment
468	Amide N-H stretching
1001	Out-of-plane aliphatic C-H wagging
1039	Aliphatic C-C stretching
1177	Ring breathing
1299	In-plane aromatic/ aliphatic C-H wagging
1606	In-plane aromatic C-H wagging/ C-C stretching
1666	Quinone C=O stretching

Table 3.2 Vibration assignments of reduced AQ

Raman shift/ cm^{-1}	Assignment
1001	Out-of-plane aliphatic C-H wagging
1039	Aliphatic C-C stretching
1224	O-H wagging/ Amide N-H wagging
1289	Ring breathing
1415	Aromatic C-C stretching
1299	In-plane aromatic/ aliphatic C-H wagging
1606	In-plane aromatic C-H wagging/ C-C stretching

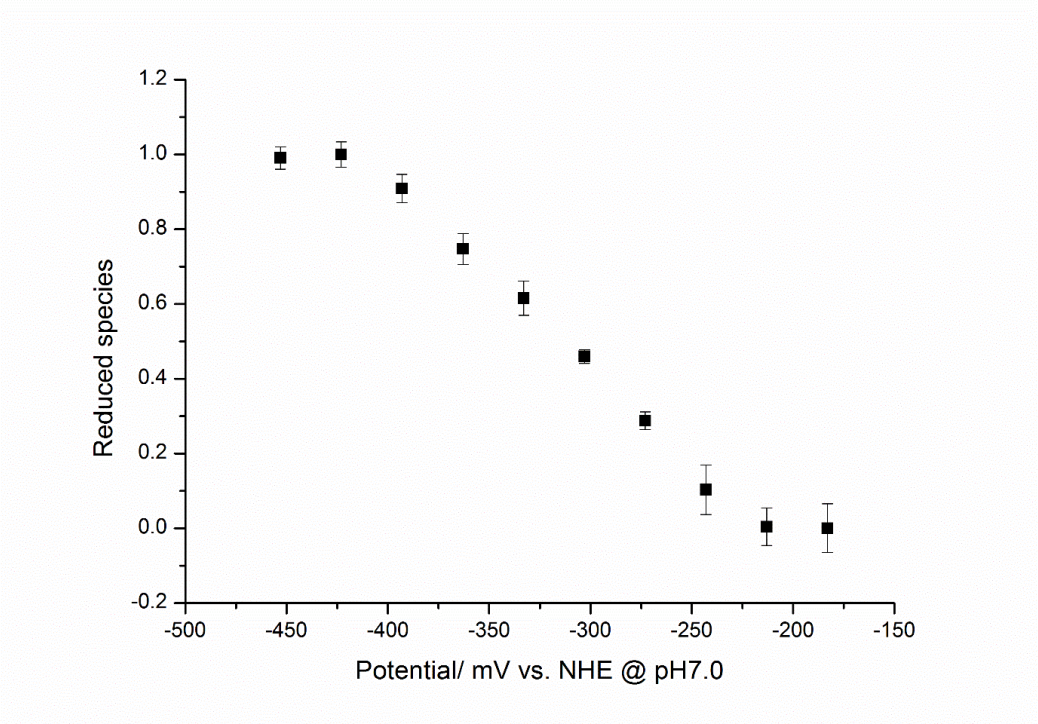

Figure 3.17 Calibration curve of AQ and its covering window obtained on the Renishaw InVia Raman Spectrometer

Only one set of redox peaks were detected in the CV of AQ, which suggests that the electrochemical reaction of AQ is a one-step, two-electron process, otherwise two separate oxidation peaks as well as two reduction peaks would be seen. Furthermore, the explanation of a stretched calibration curve corresponds to theory very well. While the CV data suggests a concerted $2e^-$ reaction, it is possible that an intermediate radical (also known as the semiquinone, see Scheme 3.8 A, B) or radical anion (Scheme 3.8 C) is able to be formed from a single-electron redox reaction (Scheme 3.8), which could broaden the measuring window.

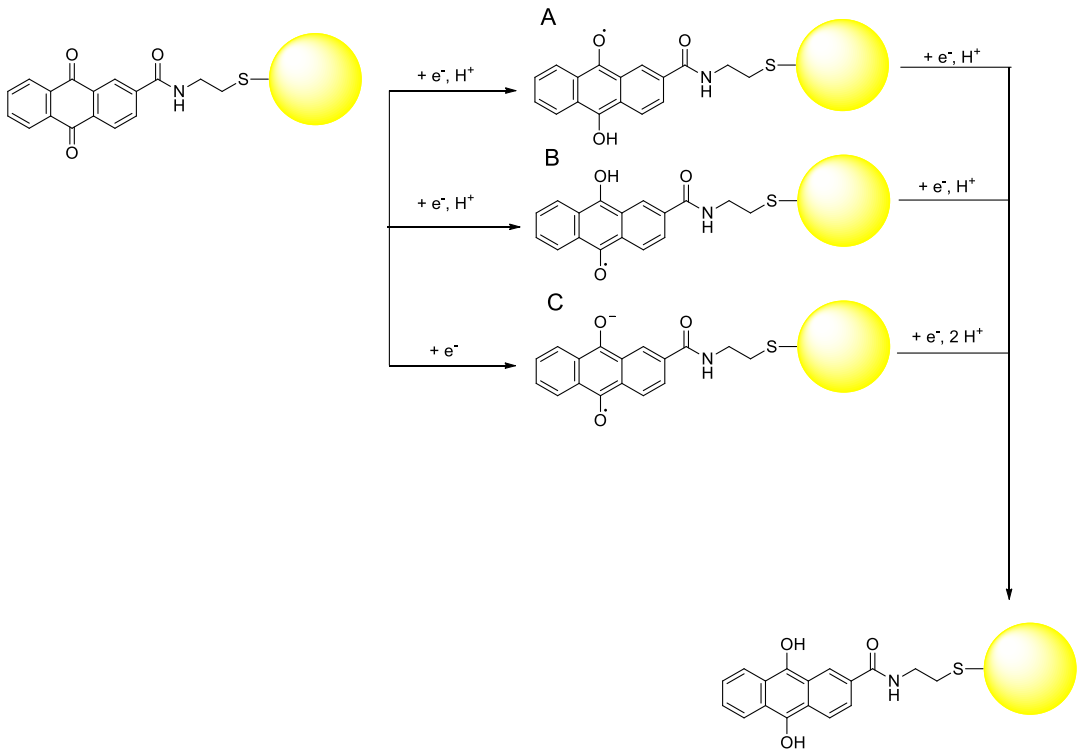

Scheme 3.8 single electron redox reaction of AQ: A and B are two isomers of the semiquinones and C is an unprotonated semiquinone

As the structure of AQ is not symmetrical, either of the two isomers of the semiquinone or an unprotonated anion might exist as an intermediate. Here we took isomer A and structure C, (a radical anion) and performed DFT calculations. As expected, by comparing the predicted spectra of semiquinones (Figure 3.18) and the spectra of AQ, the peak at 1426 cm^{-1}, which is due to the specific stretch of the semi-quinone bond (C-OH), is only present in the spectra of semi-quinones. These findings were in accordance with the CV and also further demonstrated that the stretched measuring window was not due to the formation of a semiquinone. In fact, all of the quinone probe molecules displayed the similar character of having broader calibration curves than Nernstian plots.

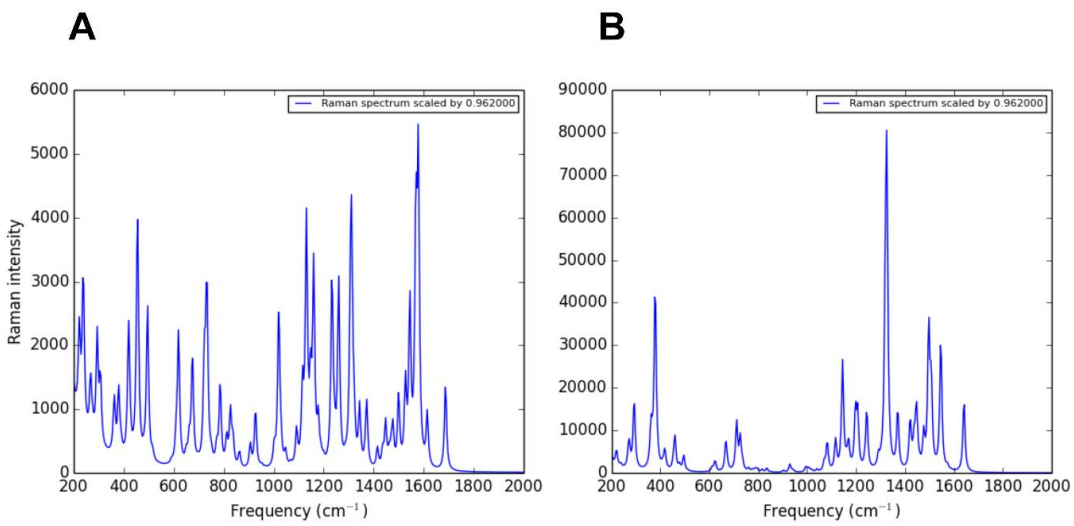

Figure 3.18 A: Predicted spectra of Structure A in Scheme 3.8 by DFT calculations B: Predicted spectra of Structure C in Scheme 3.8 by DFT calculation.

3.3.2 Spectroelectrochemistry of SAQ and DFT calculations

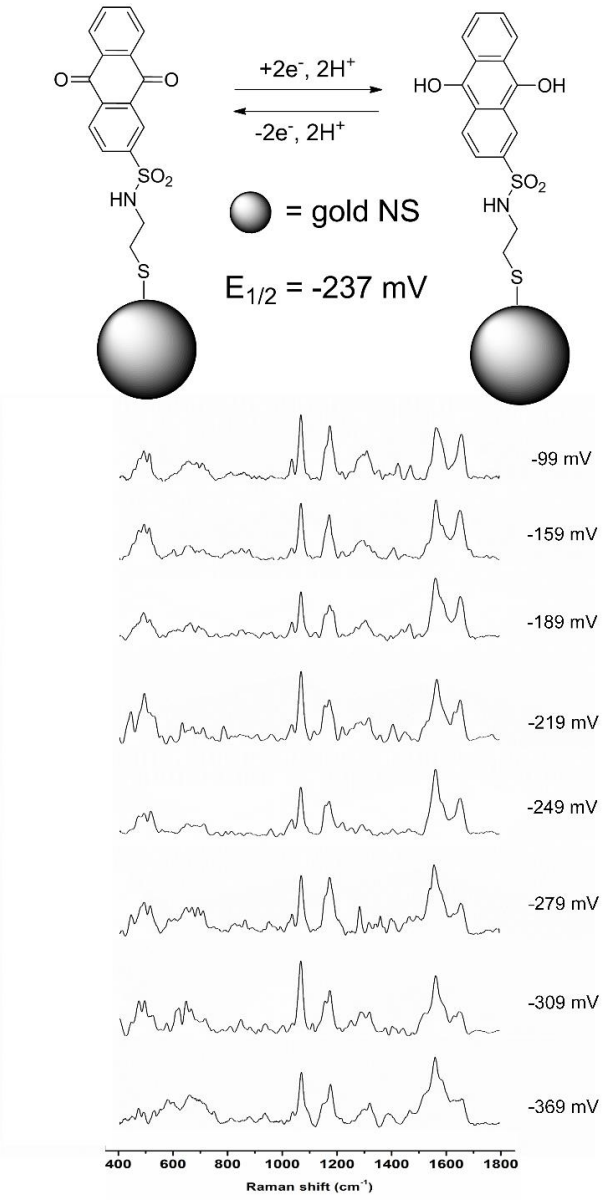

Figure 3.19 Structures, electron transfer scheme, half-wave potential and the SERS spectra of SAQ recorded from -99 to -369 mV on the Renishaw InVia Raman spectrometer. (Spectra were collected by focusing the laser on an appropriate NS aggregate for 30s using a 785 nm diode laser with 1 mW power. Baselines were corrected manually by choosing 8 points on the spectrum using Origin Pro 8.1)

Figure 3.19 shows the structures, electron transfer schemes and half-wave potential of SAQ along with the SERS spectra of SAQ at different potentials from -99 to -369 mV recorded on the Renishaw spectrometer. These spectra, again, agreed well with the predicted spectra of both reduced and oxidised species by DFT calculations (Figure 3.20). Since SAQ is a derivative of AQ, its redox dependent spectral changes behaved very similarly. The vibrational mode of the quinone C=O bond stretching was also observed at 1661 cm^{-1} and changed as a function of potential. The intensity of the peak at 1661 cm^{-1} was normalised in the same way as for AQ to generate the calibration curve of SAQ (Figure 3.21). From Figure 3.21, we can see that although SAQ also covers a larger range than the theoretical Nernstian plots, the mid-point potential of this curve is in accordance with the half-wave potential determined by the CV. This result indicates that the stretched measuring window was not an exception that happened only to AQ but to all the molecules studied.

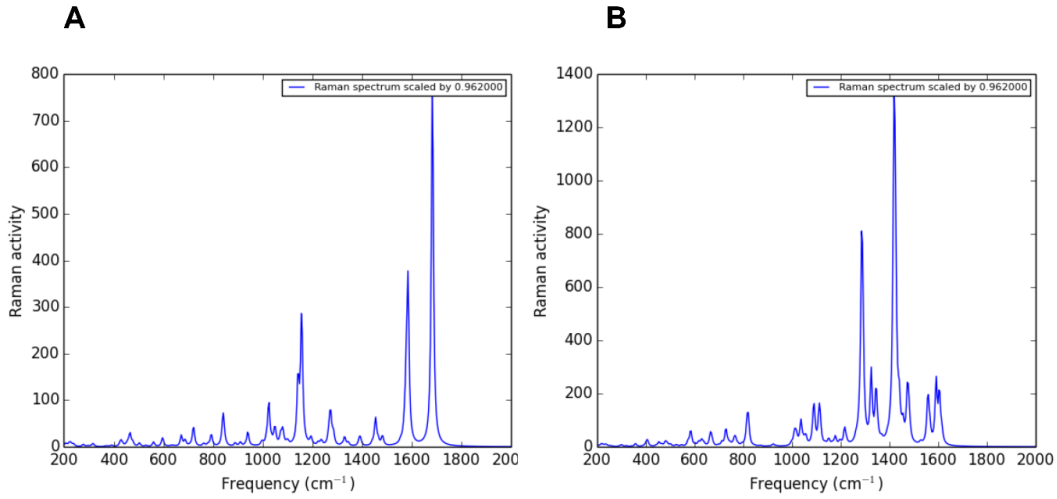

Figure 3.20 Predicted spectra of SAQ by DFT calculations: A: Predicted spectra of oxidised SAQ. B: predicted spectra of reduced SAQ.(See Table 3.3 and Table 3.4 for the tabulated frequencies and their corresponding vibrational modes)

Table 3.3 Vibration assignments of oxidised SAQ

Raman shift/ cm^{-1}	Assignment
495	Amide N-H stretching
1068	Out-of-plane aliphatic C-H wagging
1180	Ring breathing
1310	Aliphatic C-C stretching
1601	In-plane aromatic C-H wagging/ C-C stretching
1666	Quinone C=O stretching

Table 3.4 Vibration assignments of reduced SAQ

Raman shift/ cm^{-1}	Assignment
652	In-plane aromatic/ aliphatic C-H wagging
1068	Out-of-plane aliphatic C-H wagging
1180	Ring breathing
1310	Aliphatic C-C stretching
1601	In-plane aromatic C-H wagging/ C-C stretching

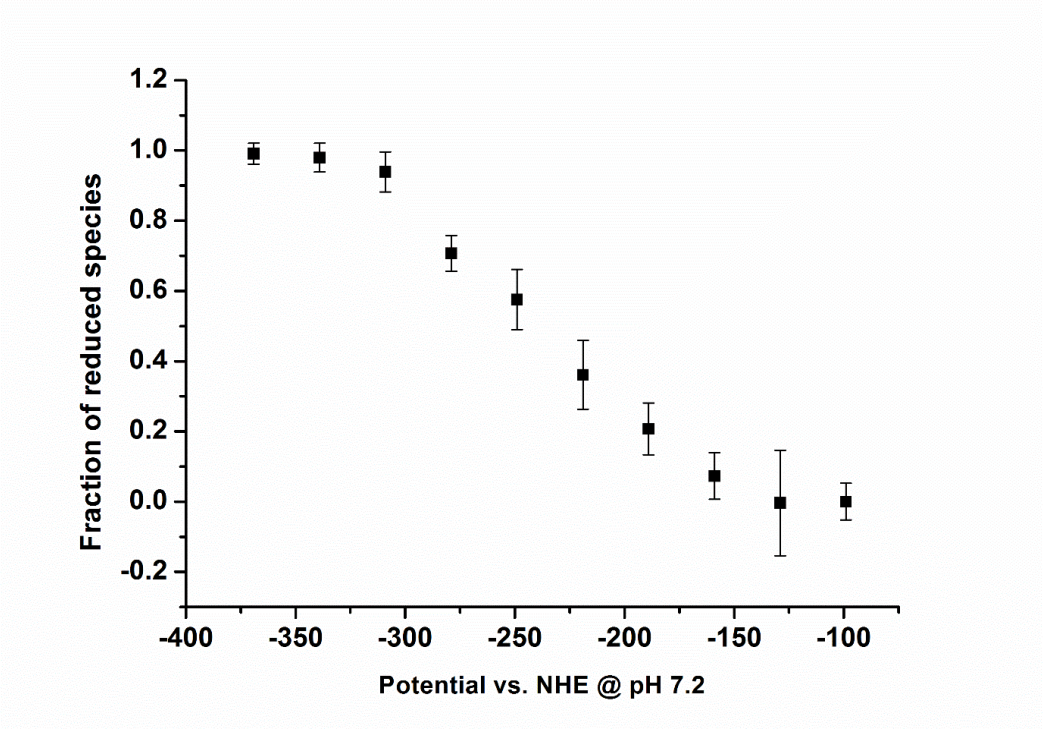

Figure 3.21 Calibration curve of SAQ and its covering window obtained on the Renishaw InVia Raman spectrometer

3.3.3 Spectroelectrochemistry of HNQ and DFT calculations

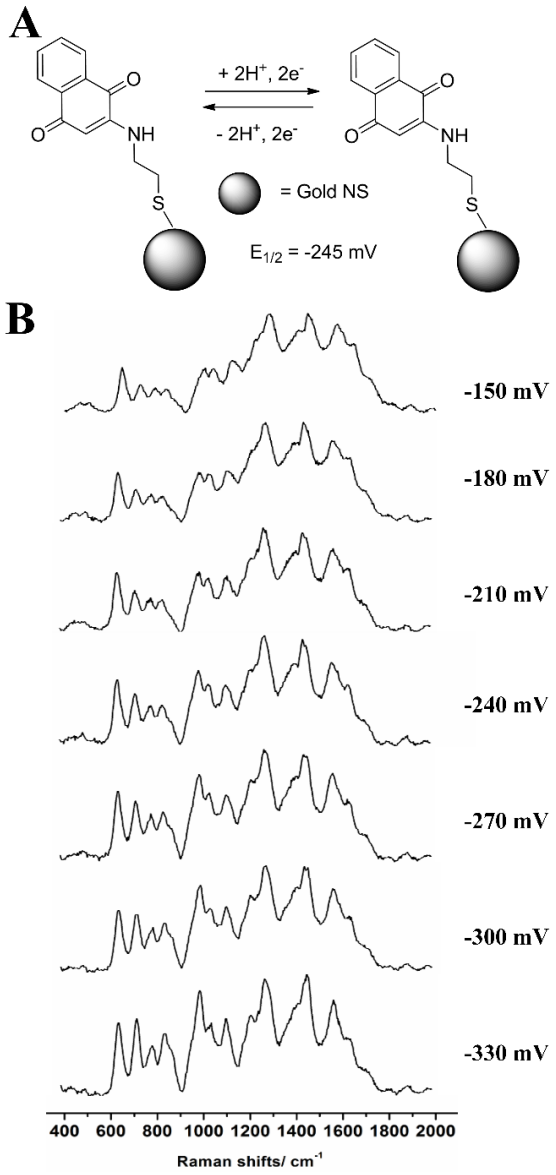

Figure 3.22 Structures, electron transfer scheme, half-wave potential and the SERS spectra of HNQ recorded from -150 to -330 mV on the Ocean Optics Raman spectrometer. (Spectra were collected by focusing the laser on an appropriate NS aggregate for 10s using a 785 nm diode laser. Baselines were corrected manually by choosing 8 points on the spectrum using Origin Pro 8.1)

Figure 3.22 illustrates the structures, electron transfer schemes and half-wave potential of HNQ along with the SERS spectra of HNQ at various potentials from -150 to -330 mV recorded on the Ocean Optics spectrometer. These spectra are in accord with the predicted spectra of both reduced and oxidised species by DFT calculations (Figure 3.23). Although HNQ is structurally similar to NQ, whose calibration curve was based on the normalised peak intensity of the C=O bond stretching around 1630 cm^{-1}, it is worth noting that the calibration curve of HNQ was generated from the normalised intensity of the peak at 725 cm^{-1}, which is due to the aromatic ring breathing of the reduced species, against the redox potential (Figure 3.24). Again, the curve of HNQ spread over a larger window than theory, however the mid-point potential was also in agreement with the half-wave potential determined by the CV. Additionally, in terms of the similar half-wave potentials of SAQ and HNQ, we find that both calibration curves are consistent in range as well as shape, suggesting that the half-wave potential is a reliable factor for predicting the measuring window.

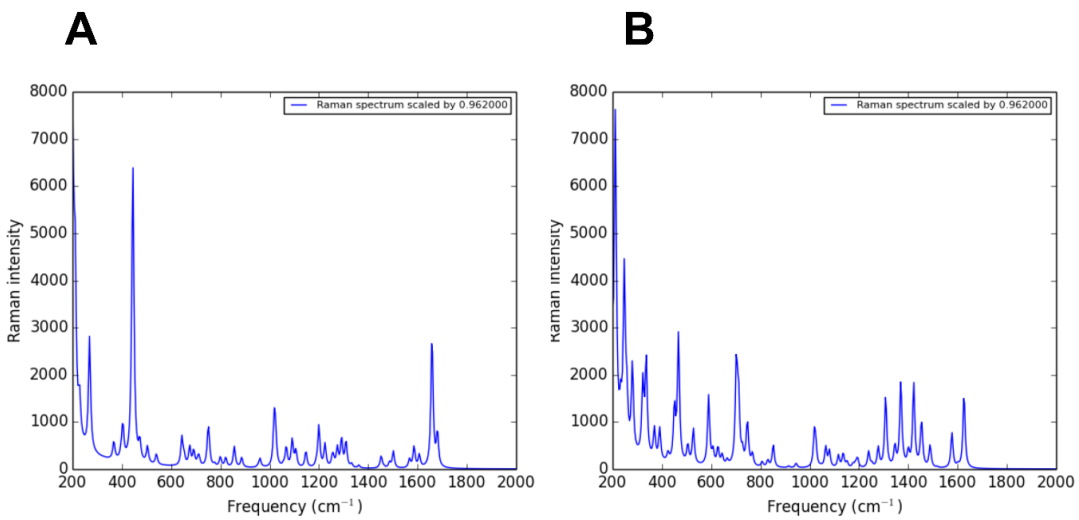

Figure 3.23 Predicted spectra of HNQ by DFT calculations: A: Predicted spectra of oxidised HNQ B: predicted spectra of reduced HNQ. (See Table 3.5 and Table 3.6 for the tabulated frequencies and their corresponding vibrational modes)

Table 3.5 Vibration assignments of oxidised HNQ

Raman shift/ cm^{-1}	Assignment
653	Out-of-plane aliphatic C-H wagging
1282	In-plane aromatic C-H wagging/ C-C stretching
1406	Symmetric ring breathing
1582	Aromatic ring stretching

Table 3.6 Vibration assignments of reduced HNQ

Raman shift/ cm^{-1}	Assignment
651	Out-of-plane aliphatic C-H wagging
725	Aromatic ring breathing
843	Aromatic ring stretching
998	In-plane aromatic C-H wagging
1118	O-H wagging
1285	In-plane aromatic C-H wagging/ C-C stretching
1403	Symmetric ring breathing
1579	Aromatic ring stretching

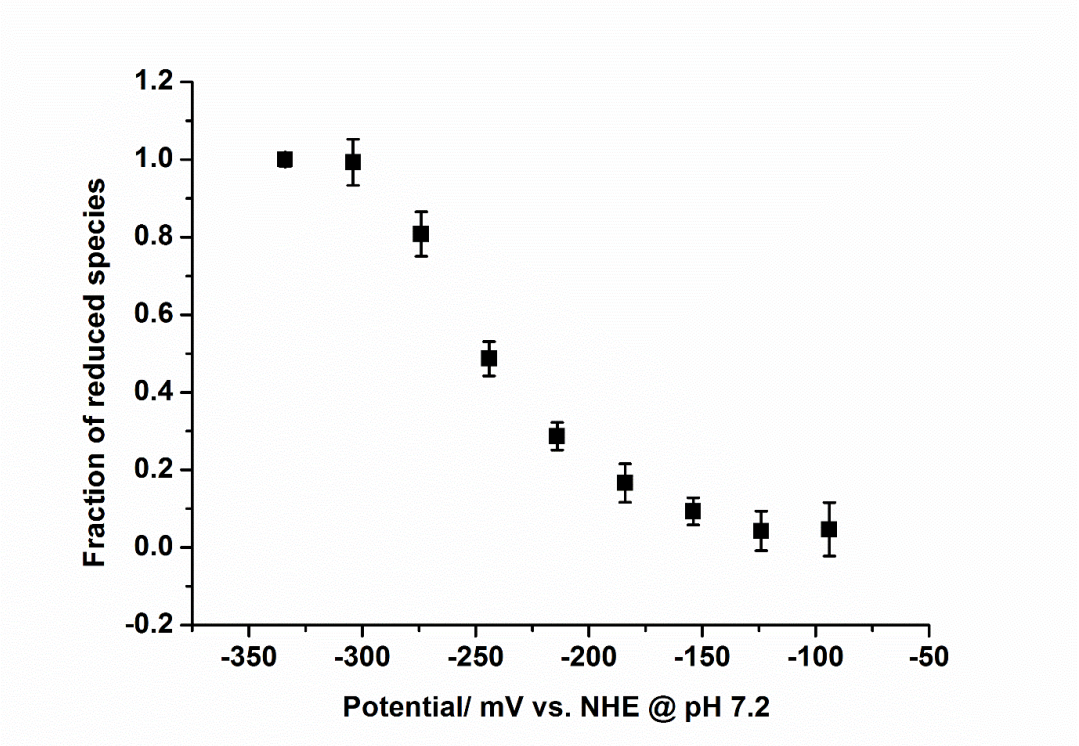

Figure 3.24 Calibration curve of HNQ and its covering window obtained on the Ocean Optics Raman Spectrometer

3.3.4 Spectroelectrochemistry of ANQ and DFT calculations

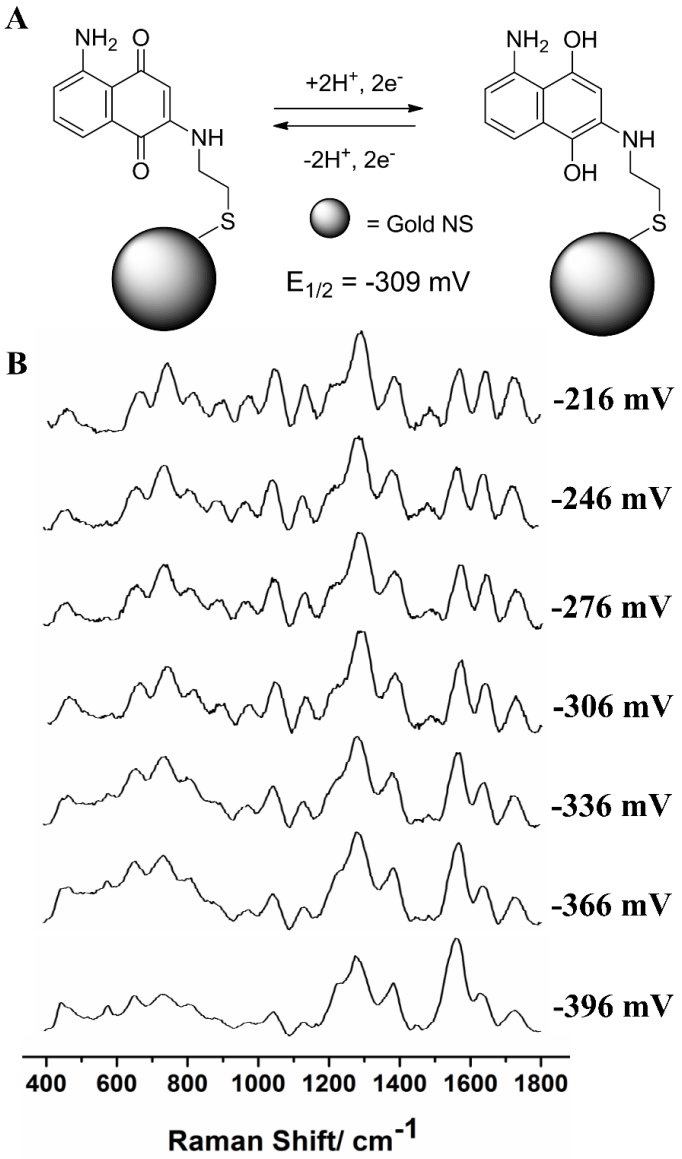

Figure 3.25 Structures, electron transfer scheme, half-wave potential and the SERS spectra of ANQ recorded from -216 to -396 mV on the Ocean Optics Raman spectrometer. (Spectra were collected by focusing the laser on an appropriate NS aggregate for 10s using a 785 nm diode laser. Baselines were corrected manually by choosing 8 points on the spectrum using Origin Pro 8.1)

Figure 3.25 depicts the structure, electron transfer schemes, half-wave potential and the SERS spectra of ANQ recorded from -216 to -396 mV recorded on the Ocean Optics spectrometer. Once again, the spectra of ANQ showed a similar oxidation-dependent pattern to other probe molecules and also matched the predicted spectra by DFT calculations. The peak at 1622 cm^{-1}, which is due to the quinone C=O bond stretching, changed as function of potential. Therefore we chose to plot the normalised peak intensity of the peak at 1622 cm^{-1} against the potential to conduct the calibration curve. As expected, ANQ also covers a broader range than the theoretical window and the mid-point potential of that curve agrees with its half-wave potential.

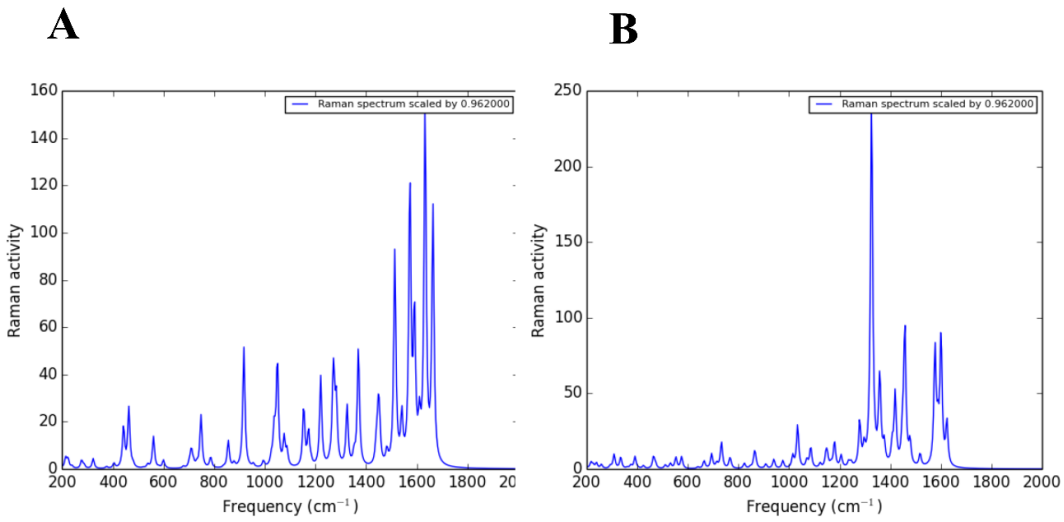

Figure 3.26 Predicted spectra of ANQ by DFT calculations: A: Predicted spectra of oxidised ANQ B: predicted spectra of reduced ANQ. (See Table 3.7 and Table 3.8 for the tabulated frequencies and their corresponding vibrational modes)

Table 3.7 Vibration assignments of oxidised ANQ

Raman shift/ cm^{-1}	Assignment
447	Carbon framework angle bending
651	Aliphatic C-C stretching
725	Aromatic ring stretching/ aliphatic C-H wagging
1035	In-plane N-H wagging
1118	In-plane aromatic C-H wagging
1285	In-plane aliphatic C-H wagging
1374	Aromatic C-N stretching
1570	Aromatic ring breathing/ symmetric H-N-H wagging
1629	C=O stretching
1715	Aromatic C-C stretching

Table 3.8 Vibration assignments of reduced ANQ

Raman shift/ cm^{-1}	Assignment
442	Carbon framework angle bending
661	Aliphatic C-C stretching
1033	In-plane N-H wagging
1290	In-plane aliphatic C-H wagging
1374	Aromatic C-N stretching
1577	Aromatic ring breathing/ symmetric H-N-H wagging
1715	Aromatic C-C stretching

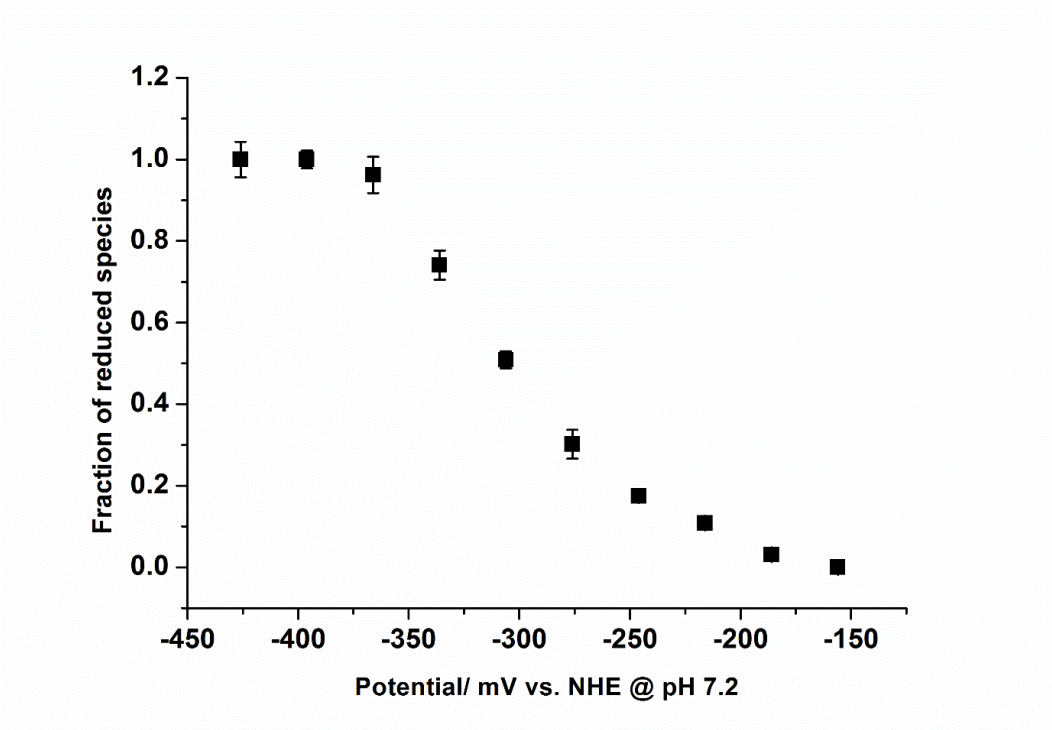

Figure 3.27 Calibration curve of ANQ and its covering window obtained on the Ocean Optics Raman Spectrometer

3.4 Conclusion

A series of redox sensitive probes has been synthesised and characterised. They all showed an oxidation state dependent pattern in their SERS fingerprints, which agreed with the spectra predicted by DFT calculations. Based on these spectral changes, calibration curves were generated and verified by comparing the mid-point potentials of the curves with their half-wave potentials. Although the practical measuring windows were all demonstrated to be more stretched than Nernstian plots, this behaviour is consistent between probe molecules and experimental systems. Results presented in next Chapter will further confirm this.

In these spectroelectrochemistry experiments, AQ and SAQ were calibrated on the Renishaw InVia spectrometer while the calibration work of HNQ and ANQ was carried out on the Ocean Optics spectrometer. Figure 3.28 shows the calibration curves of HNQ and ANQ obtained, which cover a range of more than 250 mV and is thought to be able to record the events and redox changes from cellular normoxia to hypoxia. From Figure 3.29, it can be also seen that AQ and SAQ joined to measure a similar potential window which spreads over 250 mV. Hence, on both spectrometers, I have managed to construct separate nanosensing systems which share an analogous measuring window and could be potentially applied in cells to record the redox state.

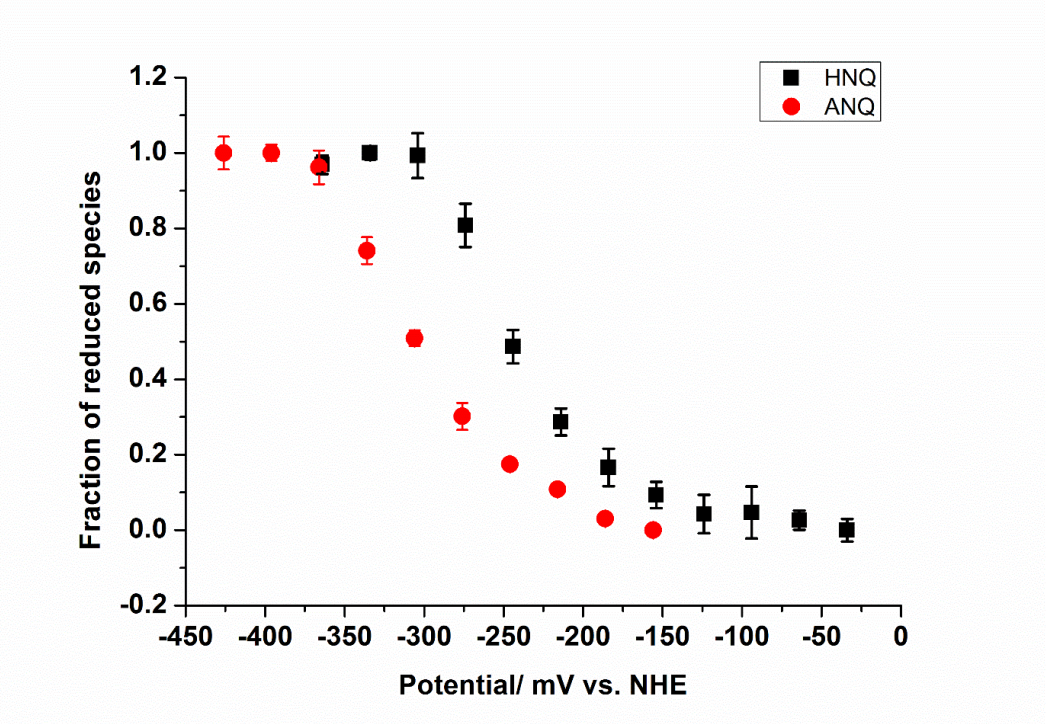

Figure 3.28. Calibration curves of HNQ and ANQ obtained on the Ocean Optics Raman spectrometer.

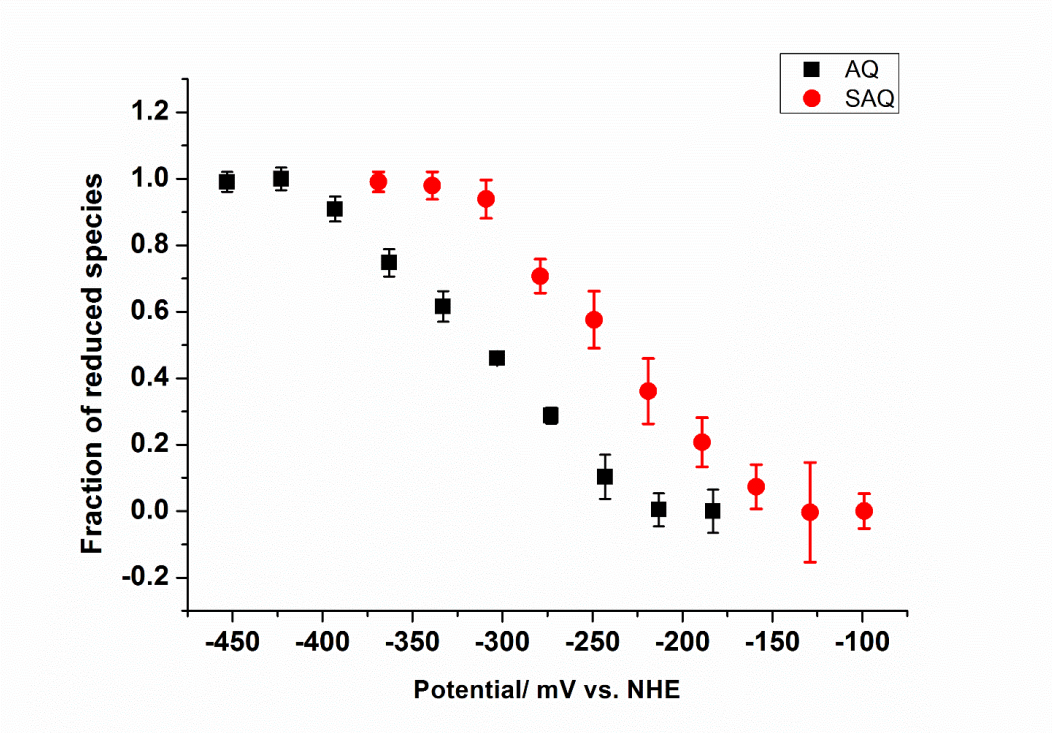

Figure 3.29. Calibration curves of AQ and SAQ obtained on the Renishaw InVia Raman spectrometer.

Chapter 4 functionalisation of nanosensor, cellular delivery and mitochondrial study

4.1 Introduction

The aim of this chapter is to investigate the fuctionalisation of redox sensitive molecules on nanoparticles and their delivery in cells and mitochondria. Gold nanoparticles (GNP) with controlled geometrical, optical and surface chemical properties have been widely used in biology, chemistry and medicine.[90,97–100] Many publications concerning GNP and their applications have included cellular delivery of drugs, antigens and genes, optical biosensing and medical therapies (Figure 4.1).[90,97,100,101]Because of the diversity of GNP types (Figure 4.2) and also the ease of grafting their surface with various molecules, GNP can serve as a platform to target specific cellular organelles.[97,99]

However, the impact of GNP on human and environmental health remains controversial. Many reports suggest that GNP are nontoxic to cells, while others contradict this and suggest that GNP could lead to many adverse effects by interacting with cellular components such as the membrane, mitochondria, or nucleus.[101–103] These malignant outcomes are related to DNA or organelle damage, oxidative stress and apoptosis. Other reports suggest that the cytotoxicity of GNP is size-dependent and varies in different cell lines.[103] In fact, due to the biocompatibility of GNP, they are less harmful to cells than other nanoparticles, such as fullerenes, metal oxide nanoparticles and carbon nanotubes, which have been demonstrated to cause oxidative stress in cells.[102,103]

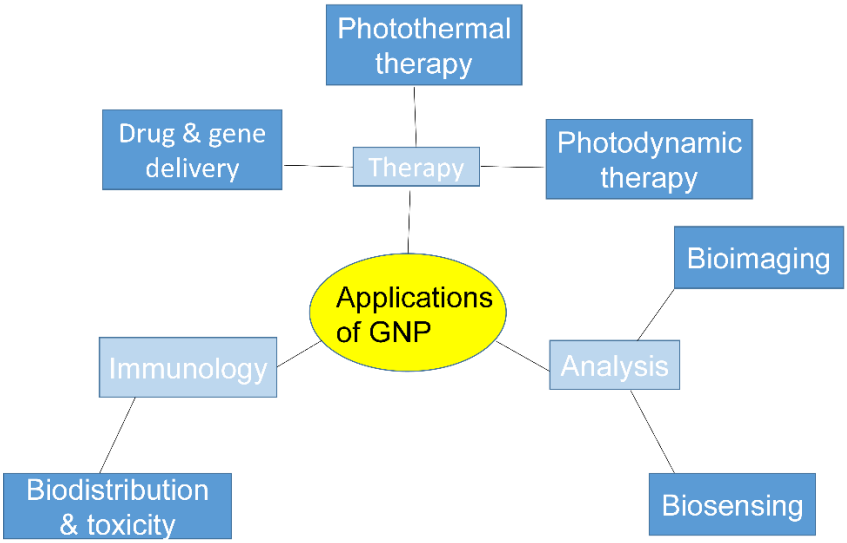

Figure 4.1 General applications of GNP

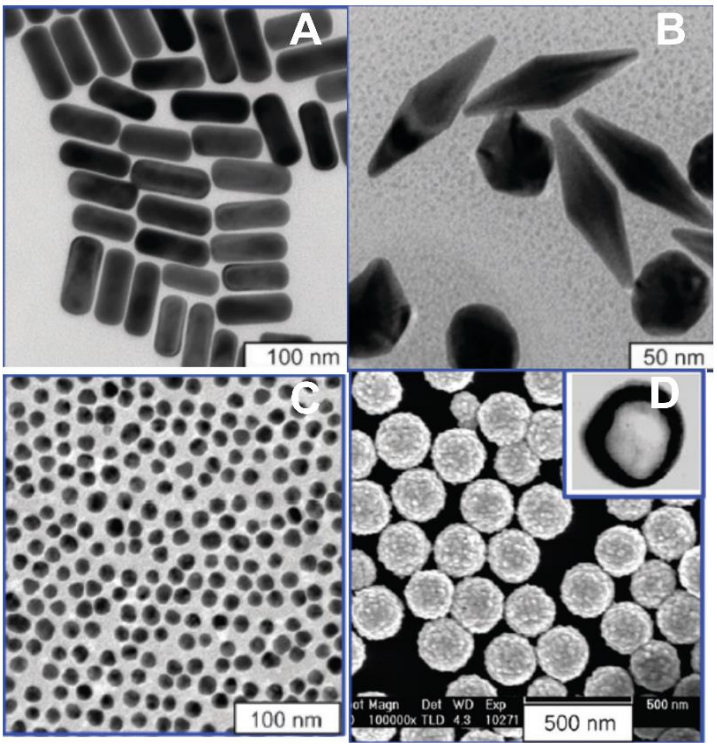

Figure 4.2 Various types of GNP: A gold nanorods B gold nano bipyramids C gold nanocolloids D gold nanoshells with SiO_2 core. (Adapted from *Ref. 5*)

Previously, the Campbell group has established a protocol of functionalising the nanosensors and delivering them into the cytosol of NIH/3T3 cells. From TEM results, nanosensors were discovered mostly to be translocated in the cellular cytoplasm without being encapsulated in vesicles or coated with lipids.[78] While the exact mechanism of the uptake is unclear, previous studies indicate that nanoparticles of different shapes and diameters can enter cells via a variety of pathways including phagocytosis, pinocytosis and receptor-mediated endocytosis.

However, functionalisation of the nanosensors can be affected by the varying solubility of the probe molecules. The unique surface properties of the nanoparticles with different diameters and shapes are also able to influence the surface functionalisation. Therefore, it was still necessary to study specific procedures to graft different probes on the surface of different types of nanoparticles. Furthermore, because a different cell line was used in this work, cellular delivery still needed to be investigated.

Previous results in our group have demonstrated that modified NS neither induce formation of reactive oxygen species nor change the cellular redox glutathione status, indicating that the introduction of such NS does not induce changes in the cellular redox environment. Since the cytotoxicity of GNP is size-dependent, the toxicity of nanorods (NR) and nanocolloids (NC) of different diameters was also studied in this work to determine whether they were harmful to cells.

4.2 Functionalisation of GNP

Due to the hydrophobicity of the organic probe molecules, aqueous solutions of these probes could not be made up because NS easily aggregate or attach to the side of Eppendorf tubes in organic solvents other than ethanol. In order to functionalise NS with the redox sensitive molecules, a mixture of organic solvent and water was used. Following the previous protocol in our group, NQ could dissolve sufficiently in 10% ethanol/water for effective functionalisation. Thus NQ derivatives (SNQ, HNQ and ANQ), with a similar solubility, could be processed in the same way as NQ. However, the AQ family (AQ and SAQ) were insoluble in ethanol. Various organic solvents were tested and 1% DMSO in water was found to work well without leading to aggregation of NS or increasing the difficulty of washing the NS. Below is the scheme of the protocol for surface-modifying NS (Figure 4.3).

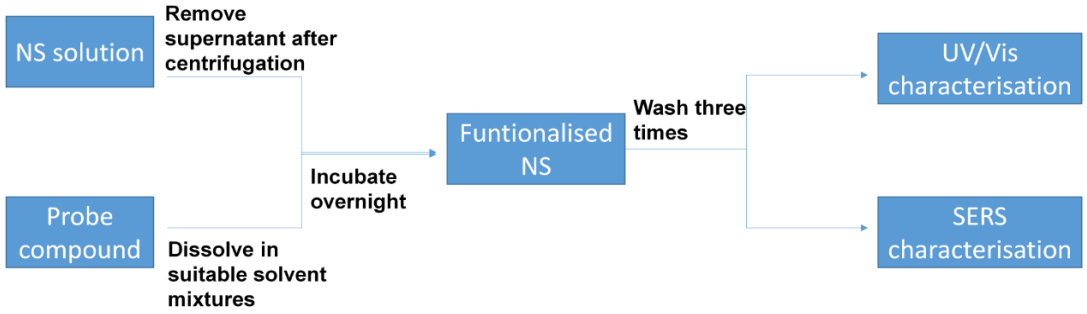

Figure 4.3 General scheme of the protocol for functionalising NS with redox sensitive molecules.

After overnight incubation with the redox probe solution, functionalised NS were thoroughly washed with water and then subjected to centrifugation to remove excess probe molecules and the organic solvents, preventing them do harm to the cells. To

confirm the modification of the NS, both UV/Vis and SERS were employed. Bare NS were resonant at 785 nm. With a layer of coating, functionalised NS showed slightly red shifted compared to bare NS (Figure 4.4). This shift demonstrated the successful modification of NS. SERS measurements of the dried nanosensors on gold glass slides or Quartz slides further confirmed the coating (Figure 4.5) .

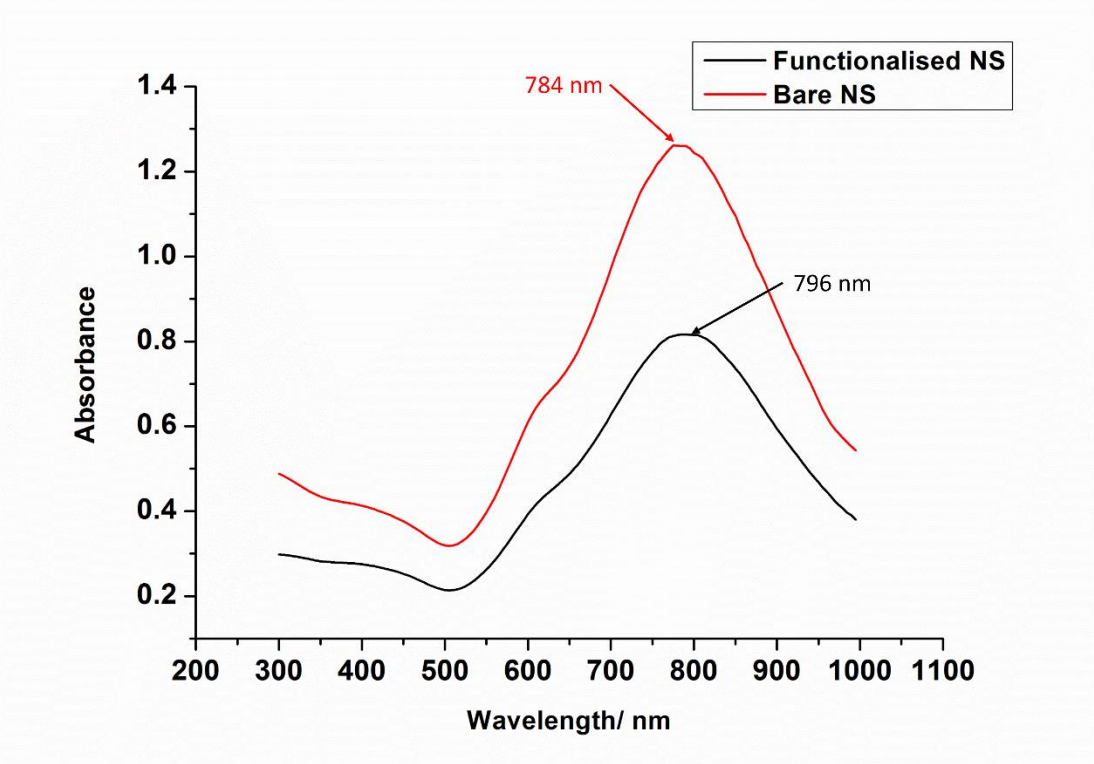

Figure 4.4 UV/Vis spectra of bare NS and functionalised NS

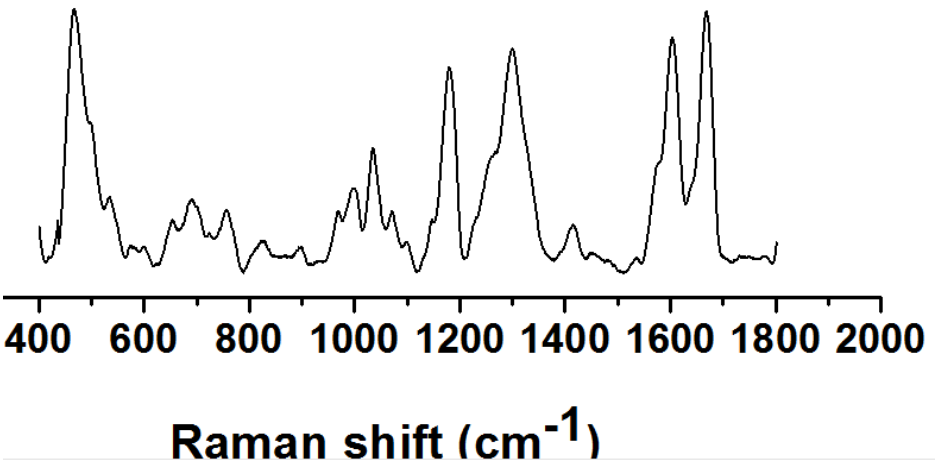

Figure 4.5 SERS spectra of the functionalised AQ-NS

4.3 Cytosolic Nanosensor Delivery

Transmission electron microscopy (TEM) is a high-resolution technique, in which an electron beam passes through ultra-thin samples.[104] The interactions of the electrons transmitted through the samples are captured using a digital camera, to generate images of the specimen. TEM can provide significantly higher resolutions than the light microscope. Since cellular compartments are beyond the resolution of the light microscope and GNP are more electron-dense than the cell tissues, TEM is a good technique to detect the cellular uptake of GNP.

In terms of the structural similarity of the probe molecules and the uncharged NS surface, the previous protocol for NS delivery was followed. Cells were treated with nanosensors in CS-free media to eliminate the negative effect of proteins. TEM samples were prepared as procedures outlined in Chapter 2.2.3. As expected, the TEMs show that either single AQ-NS or small aggregates can be taken up by A549 cells and translocated to the cytoplasm (Figure 4.6). The cellular uptake of NS is in

agreement with previous work in our group which has demonstrated that both bare NS and NS modified with the redox-sensitive molecules NQ and HQ could be delivered into the cytoplasm of NIH/3T3 fibroblast cells in CS-free DMEM independent of energy, cholesterol and clathrin. More images can be seen in appendix.

These TEMs also demonstrated that the nanosensors can be used to monitor intracellular redox potentials if excess nanosensors in the media are removed before measurements by thoroughly washing.

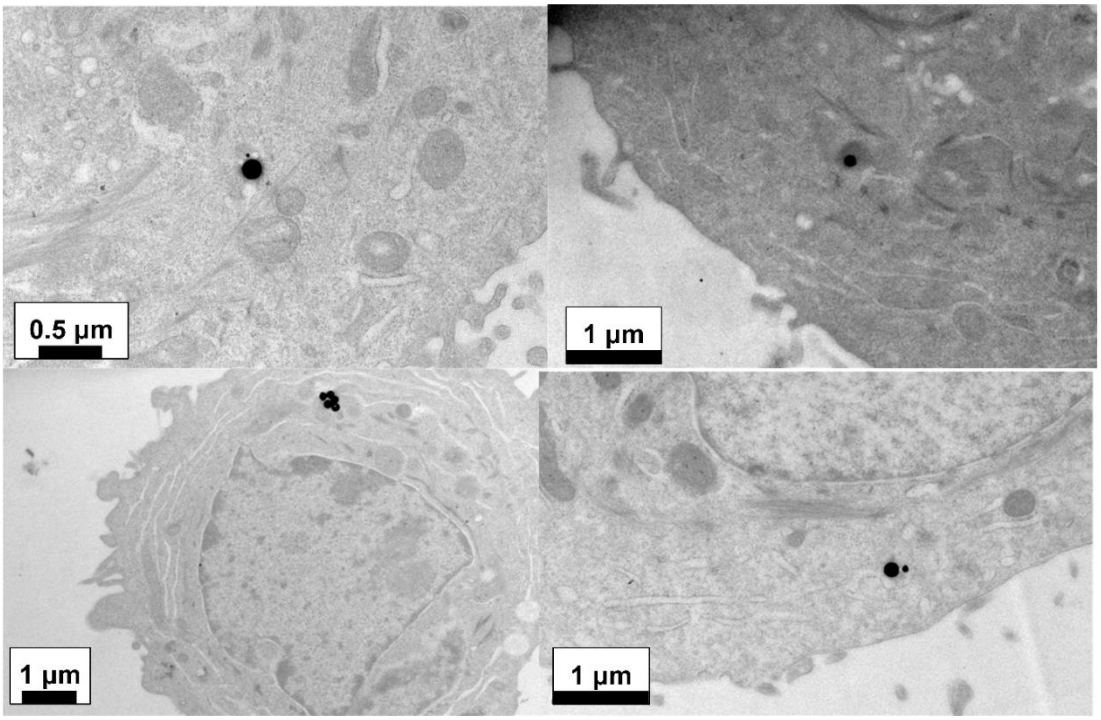

Figure 4.6 TEM images of nanosensors in cells.

4.4 MTT Assay

The MTT assay is a standard colorimetric assay to investigate cell proliferation and viability. In healthy cells, MTT, the yellow tetrazole compound, can be reduced by mitochondrial reductase to an insoluble purple formazan.[105]

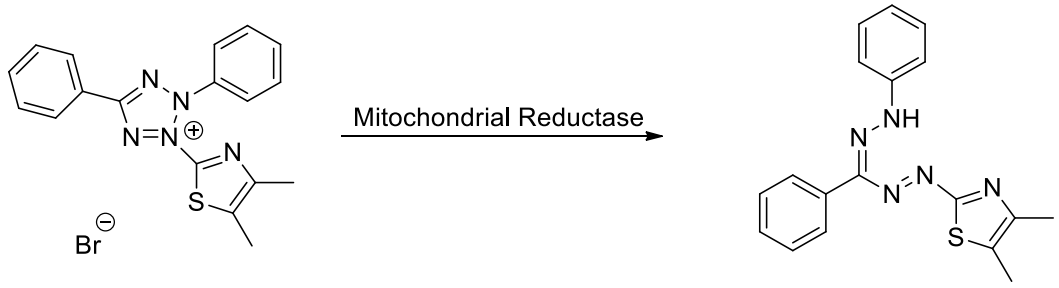

Figure 4.7 MTT reaction by mitochondria. The yellow MTT compound is reduced by mitochondrial reductase to form purple formazan crystals.

The insoluble formazan formed is dissolved in a solubilisation solution to produce a coloured solution. Absorbance was recorded spectrophotometrically at 570 nm and cell viability is calculated based on equation 4.1.

$$\%\ \text{Cell Viability} = \frac{(A_{570\text{Exp}} - A_{690\text{Exp}})}{(A_{570\text{Control}} - A_{690\text{Control}})} \times 100$$

Equation 4.1 Cell viability formula based on MTT assay. A_{570} indicates the absorbance at 570 nm while A_{690} is the absorbance at 690 nm.

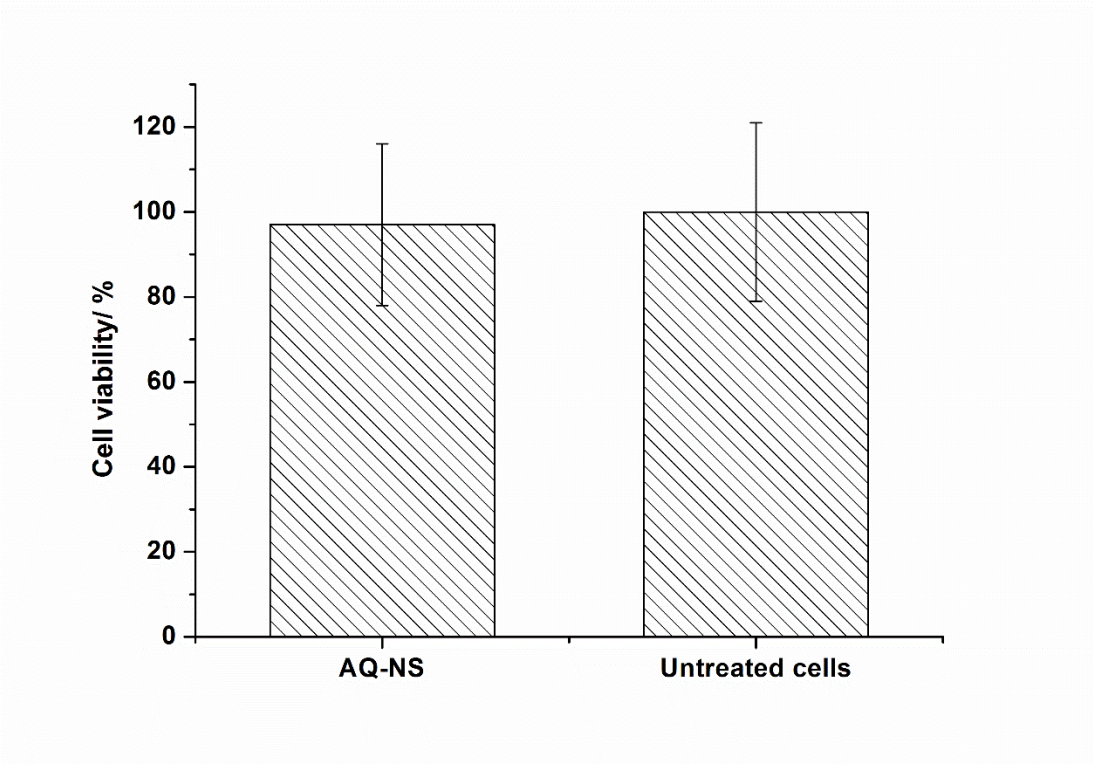

Figure 4.8 Cell viability determined by the MTT assay. Error bars represent the standard deviation of three independent measurements. For each sample, at least 2000 cells were measured to generate the assay result.

From Figure 4.8, it can be seen that the calculated viability of AQ-NS treated cells was 97% ± 19%, which showed no significant stimulation or inhibition of cell viability or growth induced by the introduction of AQ-NS. Thus, the uptake of nanosensors was not toxic to the cells as determined by the MTT assay.

4.5 Intracellular pH measurements

This chapter aims to reversibly measure the redox potential in live cells using the well-characterised SERS nanosensors and also quantify the potential change when cells respond to chemically induced hypoxia.

As Chapter 3 stated, our nanosensors are sensitive to pH changes since protons are involved in the conversion between their reduced and oxidised forms. A slight change in intracellular pH (pH_i) can result in a non-negligible shift in the cellular redox potential value measured from inside the cells. Hence it is very important to know the pH_i and its variance when cells respond to chemically induced hypoxia.

Currently there are several techniques which can be used to measure pH_i, including SERS-based nanoprobes [106,107], pH sensitive GFP[108] and some fluorescent dyes[109,110]. Among them, BCECF, AM (2',7'-Bis-(2-Carboxyethyl)-5-(and-6)-Carboxyfluorescein, Acetoxymethyl Ester) is considered a gold standard tool and the one most widely employed to study pH_i.[109,110] The BCECF, AM was purchased from Life Technologies as a mixture of three different molecular species of the AM ester of BCECF (Figure 4.9); however, all three forms are membrane-permeant and can be converted to the same BCECF acid (Figure 4.9) by a nonspecific intracellular esterase, and shows a pH-dependent spectral response. Once entering the cells, the acid form of BCECF is dominantly positively charged which can be better retained inside the cells. BCECF acid has a pK_a of 6.98, which is ideal for estimating the pH_i. Measurements with BCECF can be made by determining the pH-dependent ratio of emission intensity at 535 nm when the dye is excited at ~490 nm versus ~440 nm.

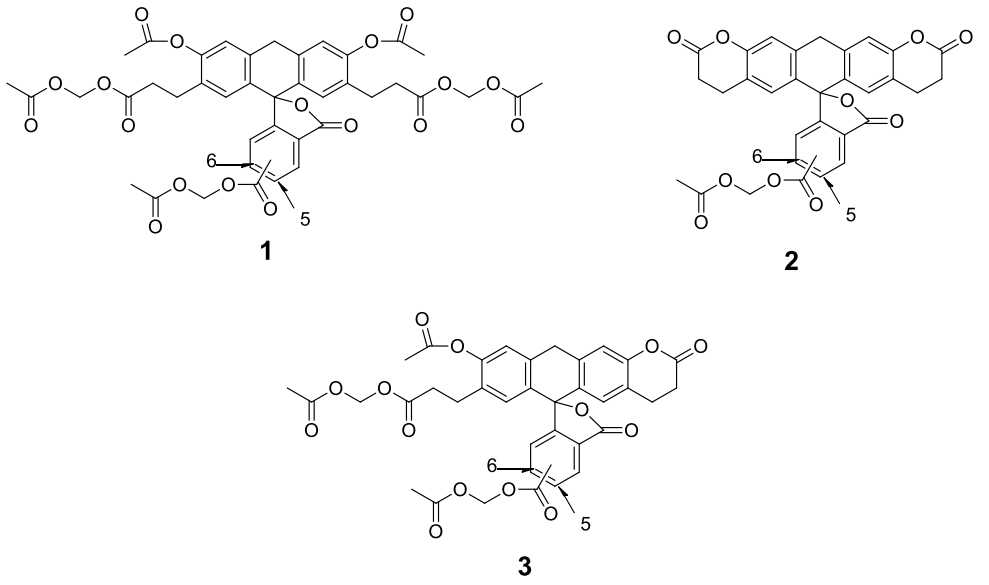

BCECF, AM is a mixture of the three moleculer species as shown above.

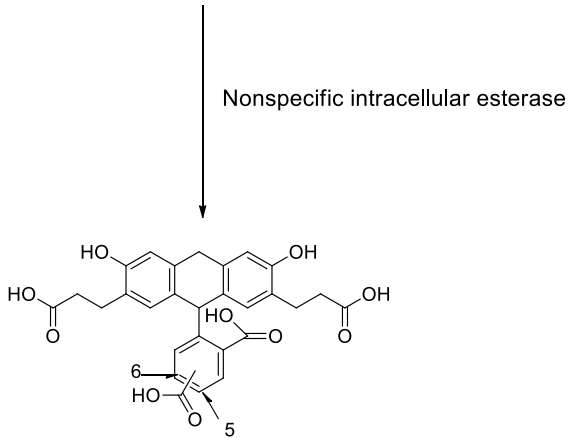

Figure 4.9 Structures of BCECF, AM and BCECF acid and the conversion from the ester form to acid form. Arrows in each of these structures represent the mixture of 5- or 6-carboxyfluorescein.

4.5.1 *In situ* calibration of BCECF fluorescence response

BCECF, AM is a mixture of esters which are non-fluorescent and insensitive to pH, hence it is not suitable for *in vitro* calibration. We can instead use the acid form of BCECF to construct the calibration curve. However, since the fluorescent response may be different when the dye is loaded into cells, *in situ* calibration was carried out with the help of Nigericin to equilibrate the intracellular and extracellular pH. Nigericin is an H^+, K^+ ionophore and acts as an antiporter of H^+.[111,112] As the intra- and extracellular pH was equilibrated, the pH of the buffer, which also represented the pH in cells, was recorded immediately after the fluorescence measurements.

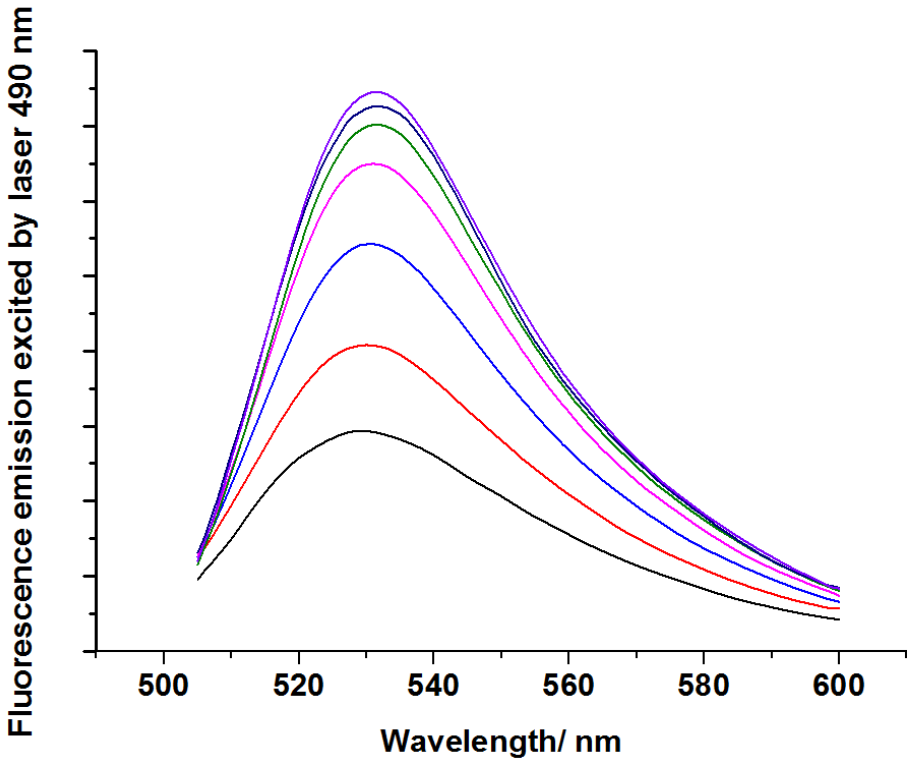

Figure 4.10 pH-dependent spectral change of BCECF acid in cells excited at 490 nm. The

pH_i was varied by equilibrating the inter- and intra-cellular pH with Nigericin.

Figure 4.10 shows the normalised fluorescence spectra of BCECF acid excited by 490-nm laser with varying pH. The normalisation was performed by dividing the fluorescence intensity at peak 530 nm which was excited by 490-nm laser by the peak intensity at 530 nm excited by 440-nm laser The normalised fluorescence intensity around 530 nm increases as a function of pH. Thus the normalised fluorescence intensity at 530 nm was chosen to plot against pH to generate the *in situ* calibration curve.

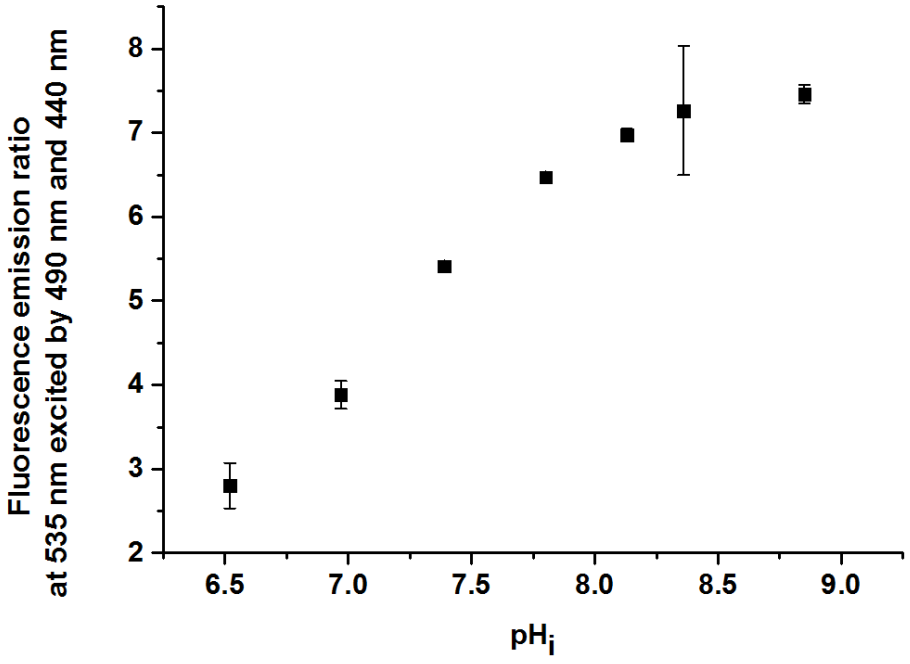

Figure 4.11 *In situ* calibration curve of BCECF performed in cells. Error bars represent the standard deviation of three independent samples.

4.5.2 pH_i measurements

In situ calibration was followed by pH_i measurements. After dye loading, cells were thoroughly washed with PBS and immersed in HBSS (pH 7.60) to obtain the fluorescence spectra. Figure 4.12 shows the pH_i data measured in treated and untreated cell populations based on the calibration curve. NS were functionalised by incubating with 1 mM solutions of AQ overnight. The solution of of AQ was 99:1 water:DMSO. Functionalised AQ-NS were thoroughly washed twice with distilled water after functionalisation to remove excess AQ. Functionalised AQ-NS were characterised with both UV-Vis and SERS. (See Chapter 4.2 for protocols and results) In order to investigate whether the AQ-NS would cause any change to the pH, 200,000 cells were seeded on 25 × 25 × 1 mm quartz coverslips and incubated for 24 h at 37 ℃ and 5% CO_2 in a humidified incubator. AQ-NS were added to serum-free DMEM (to a final concentration of 10 fM) and incubated with cells overnight. Neither the introduction of AQ-NS nor the treatment with cobalt chloride resulted in any alteration to the pH_i and all these values were found to be around 8. Since pH 8 is higher than widely reported pH_i ranging from 7.0 to 7.4[113–115], after the last run of each cell population, nigericin was added into the buffer to balance the intracellular pH with the buffered pH and the fluorescence spectra were collected again from these samples. As expected, the pH_i dropped to around 7.60 which is exactly the same as the pH of HBSS. These findings confirmed the measured pH_i although they were inconsistent with the literature value.

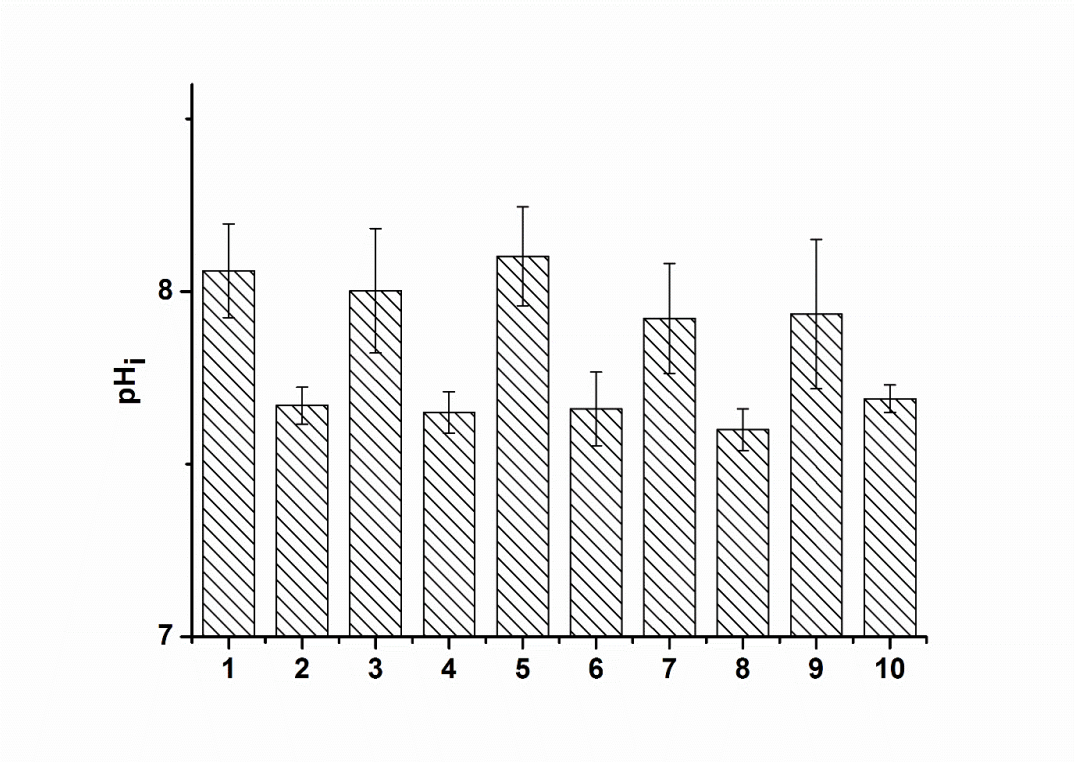

Figure. 4.12 Intracellular pH measurements: 1. Untreated cells; 2. Untreated cells, nigericin added into buffer; 3. Cells treated with AQ-NS; 4. Cells treated with AQ-NS, nigericin added into buffer; 5. Cells treated with $CoCl_2$ for 3 hr plus AQ-NS; 6. Cells treated with $CoCl_2$ for 3 hr plus AQ-NS, nigericin added into buffer; 7. Cells treated with $CoCl_2$ for 6 hr plus AQ-NS; 8. Cells treated with $CoCl_2$ for 6 hr plus AQ-NS, nigericin added into buffer; 9. Cells treated with $CoCl_2$ overnight plus AQ-NS; 10. Cells treated with $CoCl_2$ overnight plus AQ-NS, nigericin added into buffer. Error bars represent the standard deviation of pH across 4 independent samples.

4.5.3 Study of pH-dependence of $E_{1/2}$

pH_i measurements have revealed that intracellular pHs under various redox conditions was around 8, while the calibration work was carried out at pH 7.2. Equation 4.2 shows how the half-wave potential of AQ varies with the pH change. An increase of one pH unit corresponds to a negative shift of approximate 60 mV in

the half wave potential.

$$\mathrm{AQ(Red)} \overset{2e^-}{\rightleftharpoons} \mathrm{AQ(Ox)} + 2\mathrm{H^+}$$

$$E \approx E^0 - \frac{RT}{nF} ln \frac{[\mathrm{AQ(Red)}]}{[\mathrm{AQ(Ox)}][\mathrm{H^+}]^2} = E^0 + \frac{RT}{F}\, ln[\mathrm{H^+}] + \frac{RT}{2F} ln \frac{[\mathrm{AQ(Ox)}]}{[\mathrm{AQ(Red)}]}$$
$$= E^0 + 59.2\ mV lo\, g[\mathrm{H^+}] + 29.6\ mV\ log \frac{[\mathrm{AQ(Ox)}]}{[\mathrm{AQ(Red)}]}$$
$$= E^0 - 59.2\ mV\ \mathrm{pH} + 29.6\ mV\ log \frac{[\mathrm{AQ(Ox)}]}{[\mathrm{AQ(Red)}]}$$

$n\ is$ the number of moles of electrons transferred in the cell reaction

F is the Faraday Constant, $\mathrm{F} = 9.648\,533\,99 \times 10^4 \mathrm{C mol^{-1}}$

R is the universal gas constant, $\mathrm{R} = 8.314\,472\ \mathrm{J\,K^{-1} mol^{-1}}$

T is the room temperature of 298K

Equation 4.2 Nernst equation of AQ, illustrating the influence of pH change on the half-wave potential

In order to study the pH-dependence of the half-wave potential of AQ and also to confirm the theoretical deduction above, CVs of AQ were collected from a series of pHs ranging from 6 to 8.2. In Figure 4.13B, the half-wave potentials determined by CVs were plotted against their corresponding pHs. The fitted line indicates a slope of 59.23 mV which correlates exactly with the calculated value from the Nernst Equation as in the mathematical deduction above. Therefore, both the theoretical calculation and practical measurements demonstrate that it is reliable to use the Nernst equation for the adjustment of the calibration curve according to the measured pH.

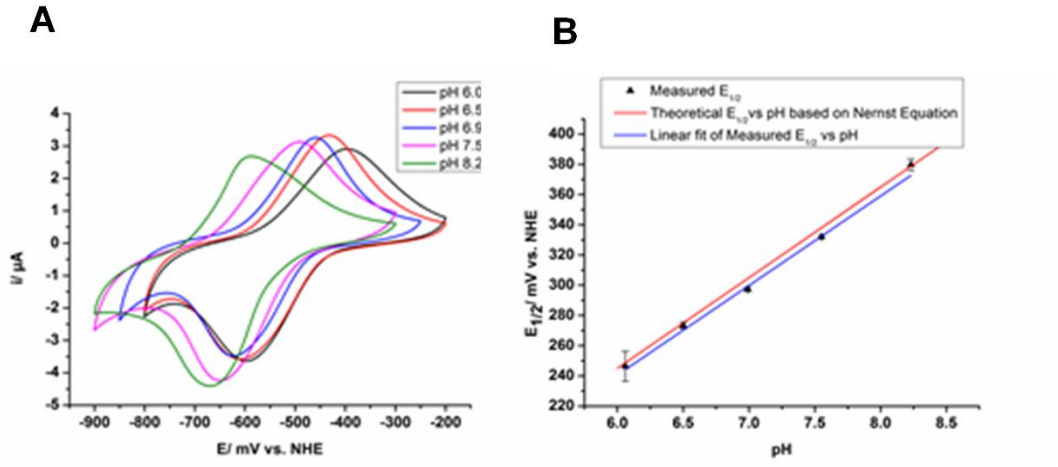

Figure 4.13 A; CVs of AQ performed at various pH spanning from pH 6.0 to 8.2. B: Practical half-wave potentials of AQ vs. pH and the theoretical half-wave potentials vs. pH according to the Nernst Equation. Error bars represent the standard deviation of three independent CVs.

4.6 Intracellular IRP measurements

4.6.1 Introduction

Chapter 3 demonstrated a suite of SERS sensors for measuring redox potentials spanning the range -150 mV to -400 mV. In this chapter, the possibility of intracellular delivery of these nanosensors, without inducing any cytotoxic effects the possibility of intracellular delivery of these nanosensors, was confirmed. Additionally, considering that the nanosensors are pH sensitive, intracellular pH measurements were performed to find out the pH_i under specific redox environment. Following on from these chapters, the next target was to use SERS nanosensors to measure redox potentials in hypoxic cells.

Raman spectroscopy has grown rapidly since the surface-enhancing phenomenon of Raman intensity was discovered and recognised on electrochemically roughened metal surfaces.[82] Especially over the past decades, with the significant development in nanofabrication[85,100], Raman spectroscopy has become increasingly popular, demonstrating its power as a suitable analytical technique for ultra-sensitive and selective detection of molecules adsorbed onto metal surfaces, such as gold and silver nanoparticles. As SERS also gives little interference from water, it shows a great potential for biological sensing applications.

Previous studies on the intracellular application of SERS have been well documented. For example, SERS-based intracellular pH probes have been well developed. pH-sensitive molecules, such as mercaptobenzoic acid, could be grafted onto the surface of nanoparticles and delivered into cells and then the cellular pH could be monitored by the SERS fingerprints of the pH probes.[106,107]

Other than intracellular pH measurements, similar application has been well established in *in vivo* glucose sensing.[116,117] Without having to draw blood, the Van Duyne group has developed a SERS-based biosensor for monitoring *in vivo* glucose concentration. With the help of SESORS (surface enhanced spatially offset Raman spectroscopy), the Van Duyne group has managed to detect blood glucose concentration accurately and consistently, even in the presence of additional bioanalytes through the skin of living rats. Thus this technique is highly promising for future clinical use and relieving the pain of diabetic patients due to frequent blood glucose checks.

SERS can be also used to study the disease state. By investigating carbohydrate−lectin interactions at the surface of mammalian cells, Craig *et al.* were

able to discriminate cancerous cells and non-cancerous cells via confocal SERS[118], which could be a useful complement for current gold techniques. In 2006, Shanmukh *et al* reported a sensitive and rapid method to detect trace levels of viruses, which was based on silver nanorod array substrates and SERS measurements.[119]

Of course, our group has introduced a SERS-based tool for monitoring intracellular redox state. Auchinvole *et al* have demonstrated the successful utility of these nanosensors to quantify the redox potential of cells both in normoxia and oxidative stress, as explained in Chapter 1.[78] However, the limited range of these nanosensors provided the motivation to develop new reporters that span a greater range of potentials and are therefore suitable for measurements in hypoxic cells.

Therefore, in this chapter, the findings of redox potential in both normoxic and hypoxic cells are presented. The correlation between cellular hypoxia and redox potential is also built using a standard assay of hypoxia.

4.6.2 Intracellular measurements using AQ-NS

All intracellular measurements were carried out using the Renishaw InVia Raman spectrometer.

4.6.2.1 Measurements in homeostatic cells

AQ covers a redox potential window ranging from -240 mV to -410 mV at pH7.2, in which cellular normoxia is included. Thus AQ was first used to measure the redox potential in resting cells. These measurements were also made to ensure the

reliability of the calibration curve, in terms of its nonconformity with Nernstian plots, by comparing the results with those obtained with NQ, also in resting cells.

Under the microscope, SERS spectra were collected from a single cell. Since excess AQ-NS were removed from the medium in PBS before measurements, all SERS spectra were collected from within cells (as verified by TEM). As expected, spectra recorded from AQ-NS were successful in revealing the intracellular cytoplasmic redox potential in cells under normoxia (Figure 4.14). By dividing the peak intensity at 1666 cm^{-1} by the intensity of peak at 1606 cm^{-1} and inserting this ratio into the calibration curve of AQ, the redox potential in normoxic cells was reported to be -319 mV ± 11 mV *vs* NHE (pH_i 8.03). At this potential, AQ is approximately 18% reduced.

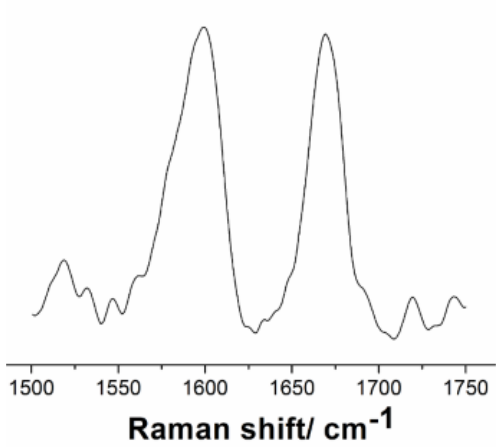

Figure 4.14 Representative spectrum of AQ-NS recorded from within normoxic cells.

In order to correlate potentials measured with AQ-NS with those measured using our established nanosensor (NQ-NS), intracellular redox potentials in resting A549 cells were also recorded with NQ-NS.

Figure 4.15 shows the SERS spectra collected from NQ-NS inside normoxic cells. The oxidation state illustrated a potential of –315 mV ± 5 mV *vs* NHE (pH_i 8.03), which correlates well with the measurements carried out with AQ-NS as shown in Figure 4.16. This result further demonstrats the reliability of the calibration curves generated using spectroelectrochemistry.

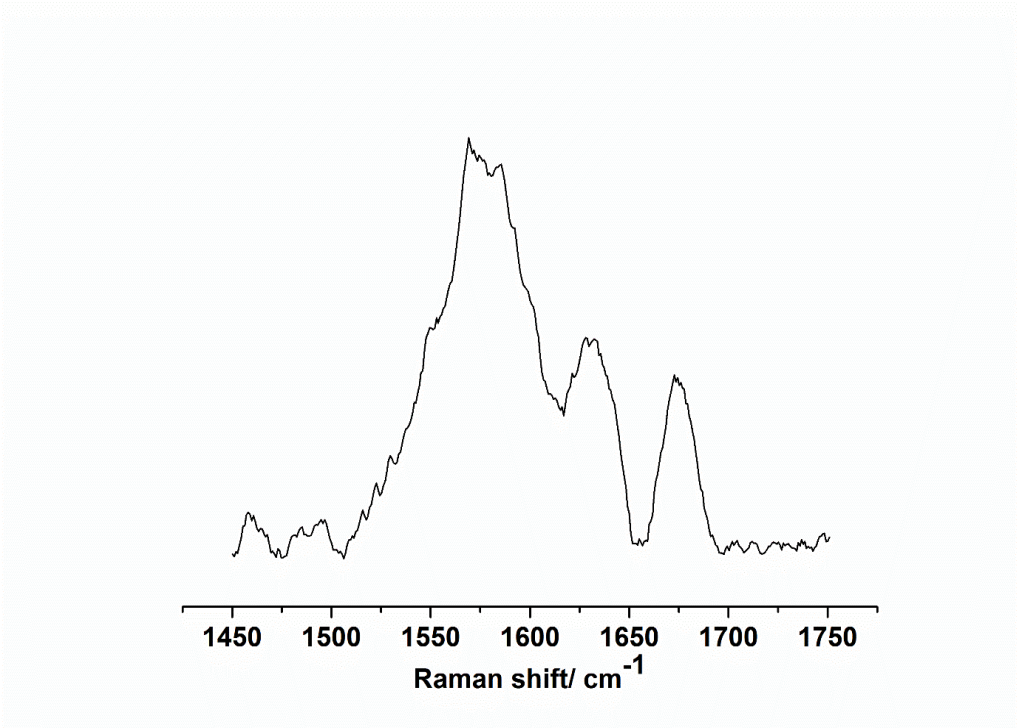

Figure 4.15 Representative spectrum of NQ-NS recorded from within normoxic cells

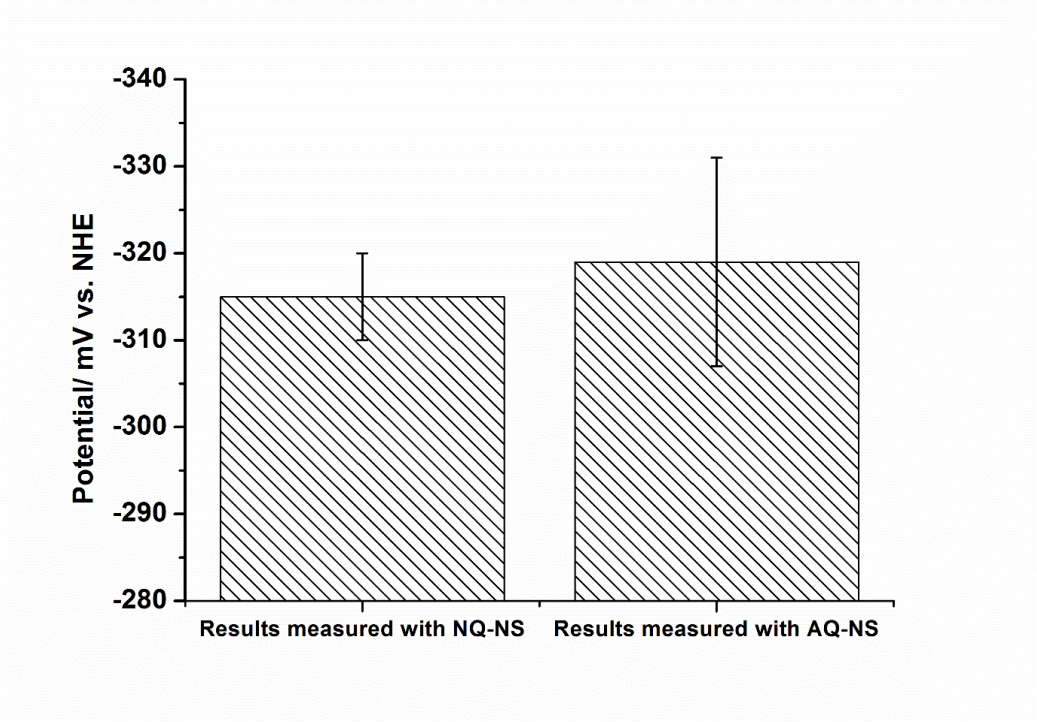

Figure 4.16 Intracellular measurements made with AQ-NS and NQ-NS under normoxic conditions. Error bars indicate the standard deviation of a minimum of eight different cells.

4.6.2.2 Monitoring redox changes in hypoxic cells

Since the primary target is to quantify the redox potential in hypoxic cells, following successful application of AQ-NS in homeostatic cells, cellular hypoxia was naturally the next thing to be studied.

The hypoxia-inducible factors (HIF) activate the pathway to enable expression of genes responsible for hypoxia. However, in normoxia, the α units of HIF (HIF-1α) are rapidly degraded by prolyl hydroxylase domain (PHD), which specifically acts on the hydroxylation of two proline residues in HIF-1α.[13,22,23,27,28] When cells are exposed to hypoxia, HIF-1α is stabilised and translocates from the cytoplasm into the

nucleus, dimerizing with the β unit (HIF-1β) to form the transcriptionally active HIF-1 complex.[13,23,26,28]

In mammalian systems, cobalt chloride has been widely used in cultured cells and tissues as a chemical agent to induce a biochemical and molecular response similar to that observed in low-oxygen condition. PHD contains an iron binding site which is crucial for the function of the enzyme. Cobalt can replace iron to occupy this site and thus inactivate PHD to degrade HIF-1α. This mechanism is thought to explain the observation that treatment with cobalt chloride mimics hypoxia in cells.[120–122] In fact, besides cobalt, nickel works in the same way to initiate hypoxic metabolism while desferrioxamine (*DFO*) chelates iron to achieve the same aim.[123,124] In these experiments, cobalt chloride was used to induce cellular hypoxia.

Cells were incubated in DMEM with 100 μM cobalt chloride for 3 hours, 6 hours and overnight (16 hours). As expected, spectra collected from treated cells revealed that intracellular redox potential underwent reductive changes responding to the induction of hypoxia. After 3 hours treatment with cobalt chloride, spectra collected from AQ-NS within cells showed a dramatic decrease in the peak at 1666 cm^{-1}, which corresponded to a potential of -391 mV *vs* NHE (pH_i 8.09) based on the calibration curve. When the treatment time was extended to 6 hours, the intracellular redox potential further dropped to -424 mV *vs.* NHE (pH_i 7.94). Overnight incubation finally resulted in the full reduction of AQ-NS in cells, meaning the redox environment was even more reductive than detection limit of AQ-NS (pH_i 7.93).

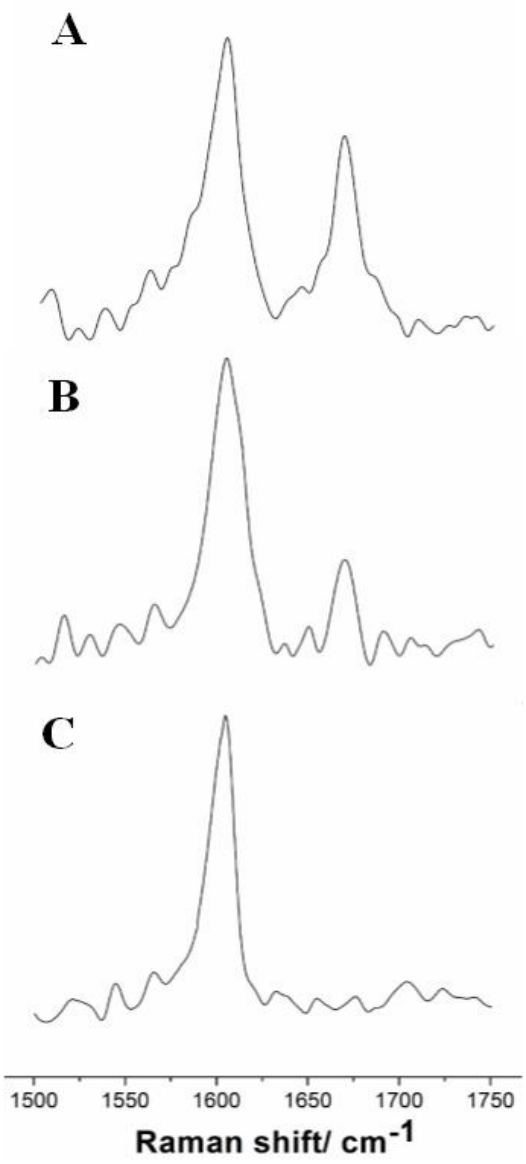

Figure 4.17 Representative spectra of AQ-NS collected from cells under different hypoxic conditions: A, Cells treated with cobalt chloride for 3 hours; B, Cells treated with cobalt chloride for 6 hours; C, Cells treated with cobalt chloride overnight (16 hours)

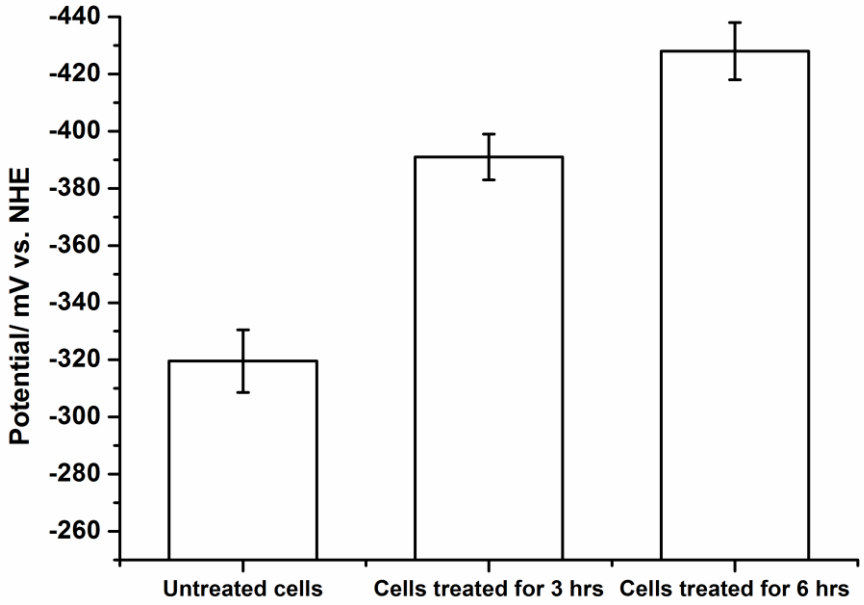

Figure 4.18 Intracellular redox potentials measured using AQ-NS under normoxic and different hypoxic conditions induced by cobalt chloride. Error bars indicate the standard deviation of a minimum of eight different cells.

4.6.2.3 Monitoring redox changes reversibly

In the CV experiment of AQ, its half wave potential was studied as well as the electrochemical reversibility. The CV displayed a reversible wave which shows AQ was reduced on a forward scan and then re-oxidised in a predictable way on the return scan. In the spectroelectrochemistry experiment, by controlling the potential AQ-NS was also able to be re-oxidised from a state of full reduction or re-reduced from fully oxidised. These findings both confirmed the reversibility of our nanosensors for monitoring redox changes. Thus it is reasonable to expect AQ-NS behaves the same inside the cells.

In order to investigate whether the nanosensors can monitor the intracellular redox potential in a reversible way, hypoxic cells were treated to induce oxidative stress for 30 min using 2,2'-azobis-2-methylpropanimidamide dihydrochloride (AAPH) (30 mM). AAPH is a radical-generating azo compound which is widely used to induce cellular oxidative stress by producing a variety of ROS, including peroxyl and alkoxyl radicals[125,126]. Figure 4.19 shows the structure of AAPH and the reactions to generate radicals.

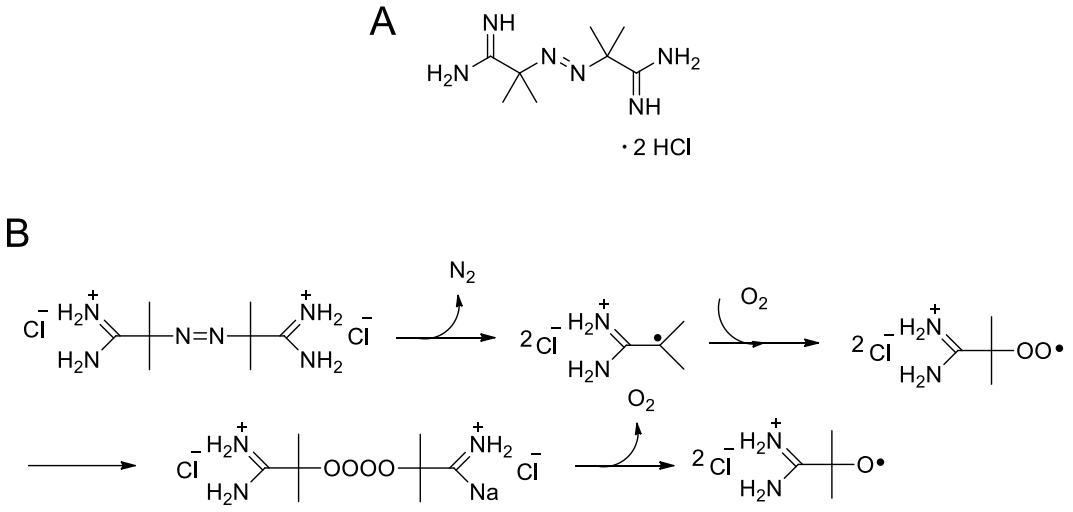

Figure 4.19 Structure of AAPH (A) and reactions to generate peroxyl and alkoxyl radicals (B)

From Figure 4.20, it can be seen that AQ-NS was fully re-oxidised, indicating a redox potential more oxidative than -240 mV *vs* NHE and demonstrating reversible recording. This ability to measure the redox potential in a reversible way is a very important and valuable property for a quantitative tool since it allows us to monitor how the intracellular redox environment changes under different redox conditions or under different metabolic regimes. In addition, with such a reversible technique, it is possible to gain an improved understanding concerning hypoxia associated diseases,

such as cardiovascular disease and cancer as well as their response to therapeutic agents and novel treatments.

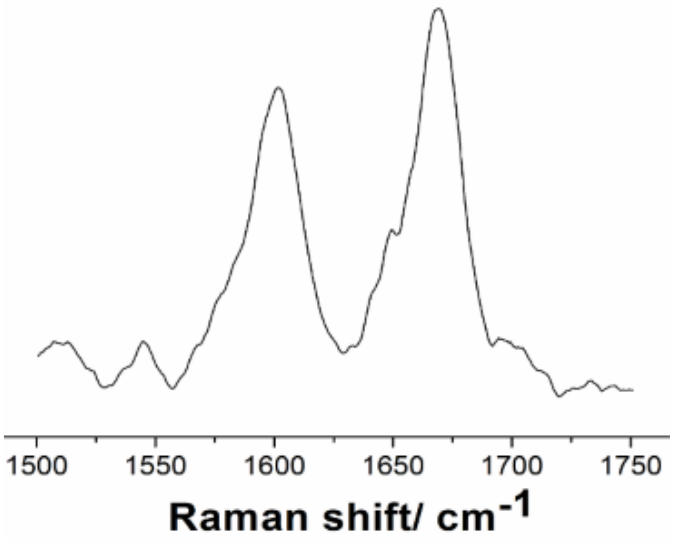

Figure 4.20 Representative spectrum of AQ-NS collected from AAPH treated cells

4.7 Fluorescent hypoxia assay

In order to compare our quantitative technique of redox potential measurements with a standard hypoxia assay and to correlate redox potential with cellular metabolism, an established hypoxia assay was used based on nitroreductase activity in cells. Nitroreductases are a family of flavin-containing enzymes which can specifically convert nitro groups to amines or hydroxylamines, using NAD(P)H as an electron source.[77,127] Since hypoxia can cause an increase in reductive stress, leading to an upregulation of nitroreductase activity, and since hypoxia results in a switch to glycolytic metabolism which produces more NAD(P)H than oxidative phosphorylation we can assay cellular hypoxia by measuring the activity of cellular nitroreductase. Cyto-ID® Hypoxia/Oxidative Stress Detection Kit is a commercially

available fluorescence hypoxia assay in which the substrate becomes fluorescent on reaction with nitroreductase (Figure 4.21). In hypoxia, the dye is reduced to an amine or a hydroxylamine with the help of nitroreductase and NAD(P)H thereby releasing the fluorescent probe. The fluorescence intensity reflects the extent of cellular hypoxia.

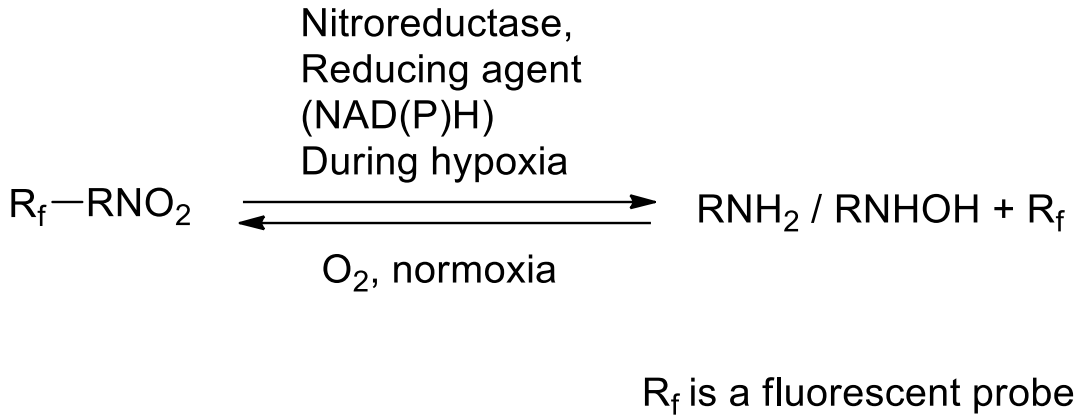

Figure 4.21 Mechanism of the nitroreductase based fluorescent assay of hypoxia.

Figure 4.22 illustrates the results of Cyto-ID® Hypoxia Assay carried out in cells treated under various conditions. It is worthwhile to note that cells treated with AQ-NS (Sample 2) didn't display any difference in fluorescence intensity from untreated cells, meaning that the introduction of AQ-NS did not cause any reductive stress in the cellular redox environment. Previous research has also demonstrated that nanosensors in cells neither induce formation of ROS nor perturb the GSH pool. Hence, taken together, these results confirm that the cellular redox state remains unchanged after addition of nanosensors.

It can be seen that treatment with cobalt chloride results in a gradual increase in fluorescence intensity. In comparison with AQ-NS measurements, it is notable that

after 3 hours there is no change in fluorescence intensity and the change in fluorescence is only detectable in cells being treated for more than 6 hours. While the general trend is the same for both the SERS nanosensors and the commercial hypoxia assay, our nanosensors detect a statistically significant and quantifiable change at an earlier time-point than the commercial assay when measured under identical experimental conditions. In Figure 4.21, the mechanism of the hypoxia assay shows that activation of the fluorescent probe is an equilibrium between the reduction of the dye by NAD(P)H and its oxidation by O_2. The data suggests that there is a threshold for fluorescent hypoxia detection which is only reached between the 3 and 6 hour time points.

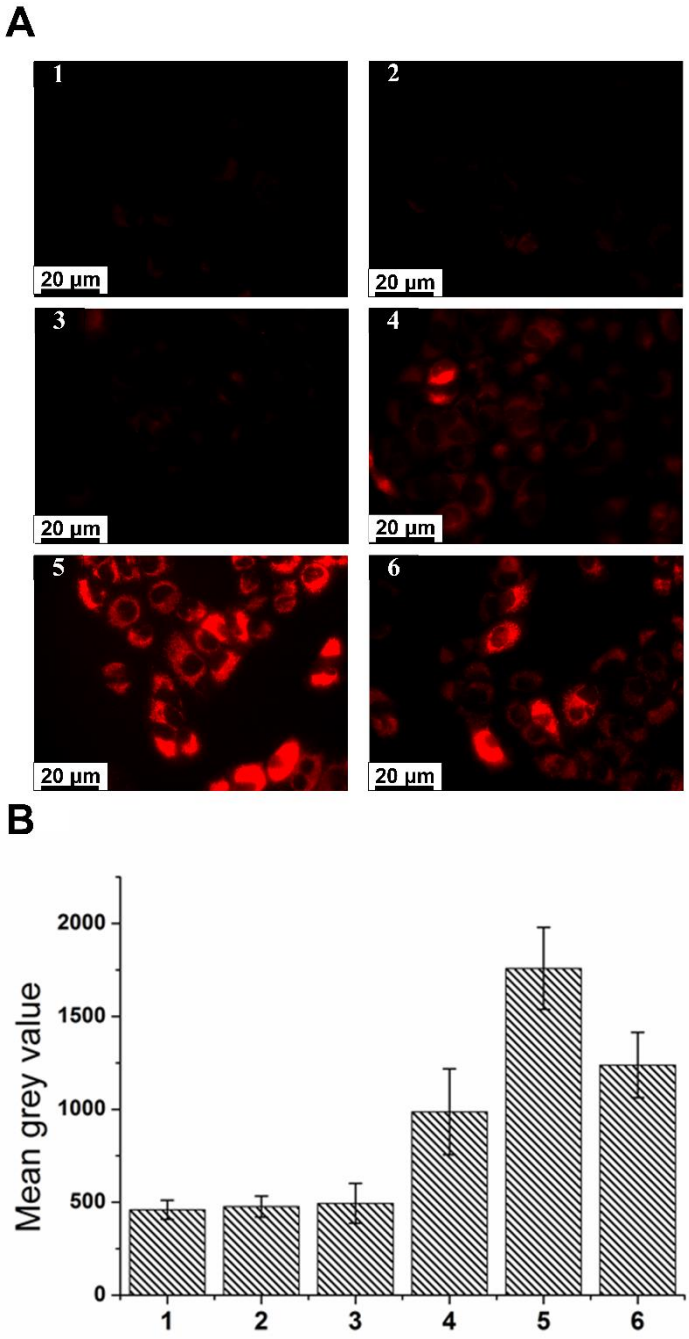

Figure 4.22 A: Fluorescence images of different cell populations. B: Mean grey values (fluorescence intensity) of different cell populations: 1. Untreated cells. 2. Cells treated with AQ-NS. 3. Cells treated with cobalt chloride for 3 hours plus AQ-NS. 4. Cells treated with cobalt chloride for 6 hours plus AQ-NS. 5. Cells treated with cobalt chloride overnight (16

hours) plus AQ-NS. 6. Cells treated with DFO for 3 hours plus AQ-NS. Error bars represent the standard deviation across six independent samples.

4.8 Conclusion

It has been demonstrated that SERS-based redox nanosensors (AQ-NS) can be taken up by the cells selectively and translocated into the cytoplasm. MTT assays also showed that the introduction of these nanosensors did not induce any toxicity to the cells. Thus these results indicate that the uptake of the nanosensors by the cells is controllable and also safe to the cells.

It is worth noting that spectra collected from cells are consistent and show no obvious contribution from other cellular constituents. This is consistent with our findings using other SERS nanosensors and may be because the nanoshell surface is fully covered with probe molecules leaving no space for the adsorption of other cellular components, and because the reporters have larger Raman cross-sections than macromolecules such as proteins and nucleic acids.

The intracellular measurements shown above have demonstrated that AQ-NS is a powerful technique to quantify redox potential in homeostatic cells and report on the redox changes occurring in hypoxic cells. In Figure 4.23, which summarises a group of normalised SERS spectra collected from various cells, it can be seen that AQ-NS indicates a good resolution of redox potentials. As cellular hypoxia intensified with treatment time, the normalised intensity of peak at 1666 cm^{-1} decreased sensitively. The ratiometric nature of our nanosensor means that the measurement of redox potential is independent of the intensity of the SERS signal – this means that we do not need to correct the absolute intensity for the number of sensors in the focal

volume or for the variation of laser power. As long as a spectrum with an acceptable Signal to Noise Ratio (SNR) is recorded, its related potential can be obtained from the calibration curve.

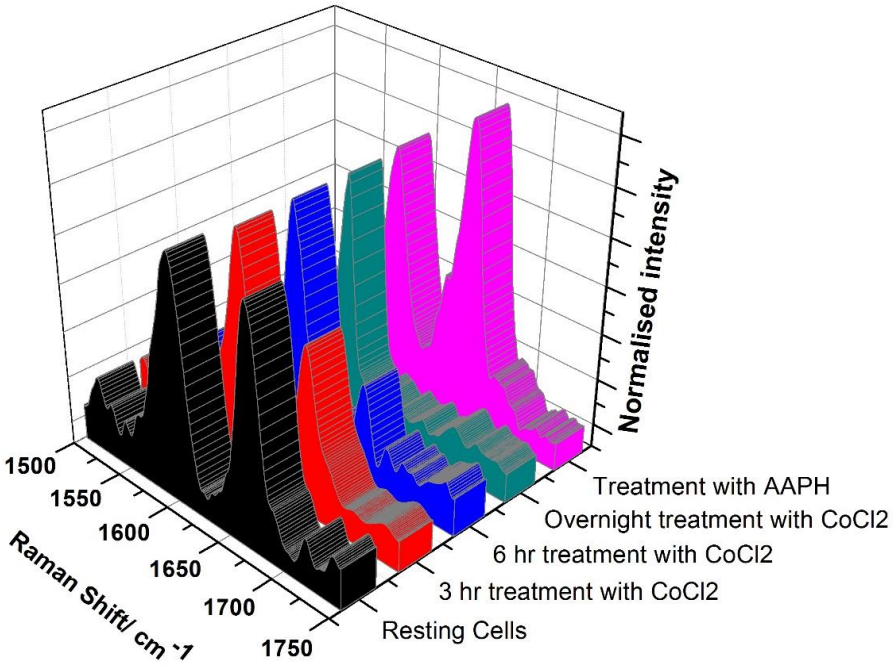

Figure 4.23 Normalised spectra of AQ-NS collected from cells under various redox conditions.

When cellular hypoxia was induced by treating the cells with cobalt chloride, the intracellular redox potential observed using AQ-NS became progressively reductive. This happens due to the metabolic switch caused by the hypoxia. Stabilised HIF initiates the upregulation of a group of genes related to pro-survival signalling and subsequently leads to a series of cellular metabolic changes responding to hypoxia, including phosphorylation to glycolysis. By diminishing mitochondrial ETC activity and cellular ATP utilisation, less NADH is supplied to the ETC for the production of

ATP in the mitochondria thereby increasing cytosolic NAD(P)H. Since NAD(P)H is the main source of electrons in the cell, this would shift the cytosolic redox balance to a more reduced state with a higher ratio of [NAD(P)H]/[NAD(P)$^+$] and the thiol pool (mainly [GSH]/[GSSG]) as demonstrated by our measurements.[11] In addition, there is literature indicating that the generation of ROS is also suppressed by decreased ETC activity during hypoxia which would further make the intracellular redox state more reductive.[15,20] Figure 4.24 illustrates the pathway activated by cobalt chloride and its downstream effects to a more reductive cytosolic redox state.

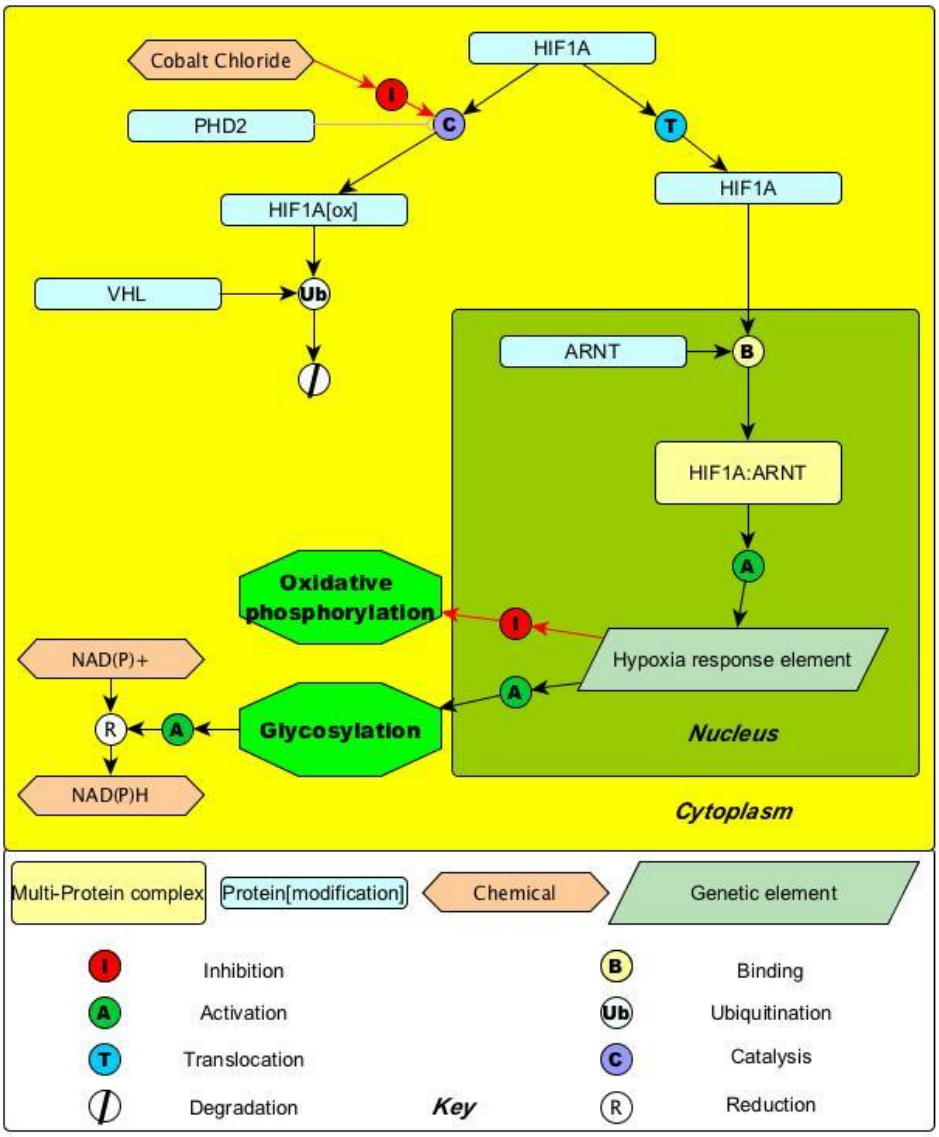

Figure 4.24 Pathway map illustrating how inhibition of PHD2 results in the production of NAD(P)H and a consequent reductive shift in cellular redox potential.

The data also demonstrate that a more sensitive and more accurate technique has been established to measure hypoxia in cells. More importantly, the technique gives a quantitative measurement of redox potential which is more easily compared across data-sets and between labs than a fluorescence assay based on intensity.

The measured redox potentials of cobalt chloride-treated cells using AQ-NS are significantly more reductive than those of resting cells, indicating that cobalt chloride-induced hypoxia has promoted generation of more cellular reductants and is in line with observations that HIF-mediated signaling causes a switch in metabolism away from oxidative phosphorylation and towards glycolysis, thus producing more of the cell's primary sources of electrons (NADH and NADPH).

Chapter 5 Mitochondrial nanosensor delivery

5.1 Introduction

Mitochondria are the main intracellular location for producing adenosine triphosphate (ATP), the fuel for the cell's activities and thus have long been known as the chemical powerplant of the cell.[128–132] ATP is generated through cellular respiration, including a series of reactions called the tricarboxylic acid (TCA) cycle that occur in mitochondria. By oxidative phosphorylation, energy is stored in the phosphate bond. When ATP is hydrolysed to adenosine diphosphate (ADP), the stored energy is then released to satisfy the demand of cellular metabolism.[128,131,132]

Mitochondria consist of two membrane systems, an outer membrane and an inner membrane, and the space between the two systems is referred to as the intermembrane space. The inner membrane is impermeable, serving as a strong barrier between the cytoplasm and the mitochondria, thereby preventing entry of small molecules and ionic species. These mitochondrial enzymes, which are necessary for the reactions taking place there, are bound in the inner membrane. The space surrounded by the inner membrane is called the mitochondrial matrix, which houses the mitochondrial DNA pool.[128,129,131,132]

The TCA cycle and the electron transport chain (ETC) contribute to the key metabolic reactions in mitochondria (Figure 5.1). In the mitochondrial matrix, NADH and succinate are produced by the TCA cycle when breaking down carbon substrates. At the mitochondrial inner membrane, electrons move from reducing equivalents, NADH and succinate, to Complex I (NADH dehydrogenase) and Complex II (succinate dehydrogenase), selectively. As an electron carrier, Coenzyme

Q passes these electrons onto Complex III (ubiquinol cytochrome c reductase) followed by Complex IV (cytochrome c oxidase), via cytochrome c. The final electron acceptor is oxygen, accepting these electrons to form water. In the meantime, coupled to the electron transfer, protons are expelled across the inner membrane into the intermembrane space. This creates an electrochemical proton gradient that drives ATP synthesis, with complexes I, III and IV working as proton pumps. Therefore, the mitochondrial environment is much more basic than the cytosol, reportedly around 7.8. The proton gradient also generates a large mitochondrial transmembrane potential, which is usually about negative 150 – 180 mV as compared to the cytoplasm.[128,129,131–134]

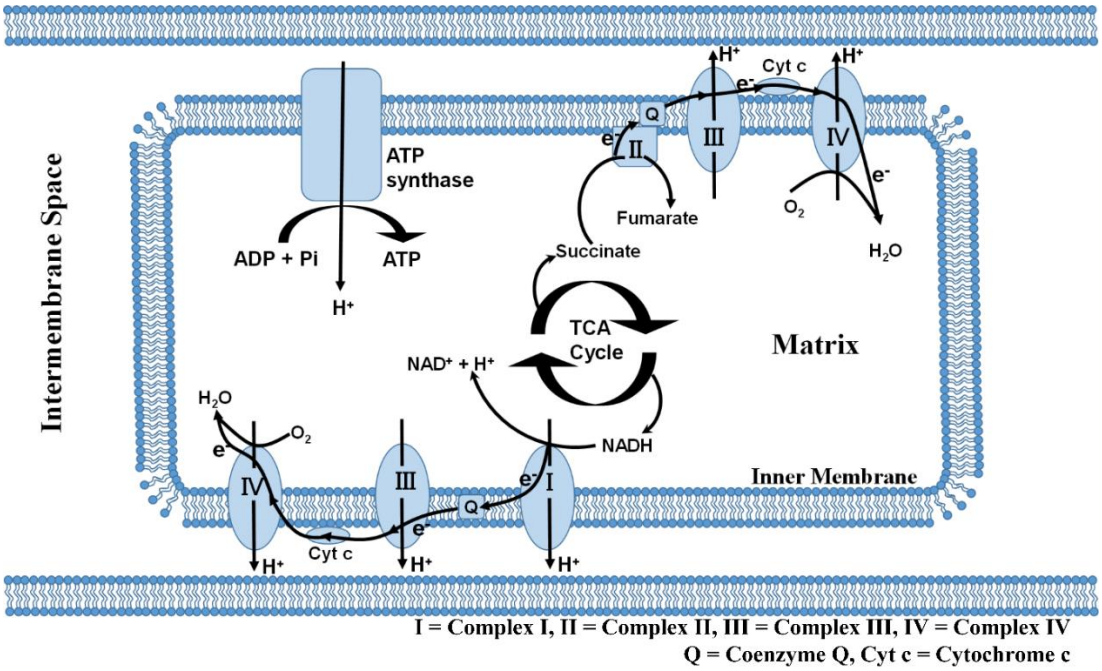

Figure 5.1 General scheme of the TCA cycle and ETC taking placing in mitochondria.

Other than the chemical power generators in cells, as stated in Chapter 1, mitochondria are the major sources of intracellular free radical species. Unpaired electrons, generated in the process of oxidative phosphorylation, can give rise to the

production of superoxide anions ($O_2^{\cdot-}$) by partially reducing the molecular oxygen. As one of the reactive oxygen species (ROS), $O_2^{\cdot-}$ is steadily converted to membrane-permeable hydrogen peroxide (H_2O_2), which then can be transferred to the cytoplasm by diffusion and subsequently converted to highly active ROS such as the hydroxyl radical ($^{\cdot}OH$).[135,136] Furthermore, mitochondrial dysfunction is also reported to be implicated in the pathology of various diseases such as diabetes, cardiovascular diseases and cancer. As a consequence, in order to expand our understanding of mitochondria and their roles in metabolism and disease initiation, there is a need to develop a tool capable of measuring the redox potentials in the mitochondrial matrix and monitoring the potential changes associated with various physiological activities.[128,130,132,135]

5.2 Triphenylphosphonium (TPP) cation

TPP cations (see Figure 5.2) are a group of lipophilic cations which can easily move through phospholipid bilayers and accumulate substantially within the mitochondria without requiring a specific uptake mechanism. The cations initially bind onto the outer surface of the membrane driven by the increase in entropy due to the hydrophobic effect. They then pass rapidly through the hydrophobic core of the membrane to the other side, followed by desorbing from the membrane.[137]

As mentioned earlier, there is a large potential around -150 mV across the mitochondrial membrane which suggests TPP cations move from a positively charged environment into a negatively charged environment. When an equilibrium of the electrochemical potential is reached between the two organelles (cytosol and mitochondria), the uptake of TPP cations ceases. At this point, the transmembrane potential has been neutralised and the ratio of the cation concentrations in the two

organelles can be determined by the Nernst equation:

$$\Delta\psi m = 59.5 log_{10}\left(\frac{[cation]_{in}}{[cation]_{out}}\right) mV \text{ at } 25\ ℃$$

From the Nernst equation, we find that approximately tenfold of the TPP cations can be accumulated within the mitochondria for every ~60 mV potential decrease. In terms of the -150 mV transmembrane potential across the mitochondrial membrane, the cation accumulation within the mitochondria can be as large as 300-fold compared to the cytosol. In addition, as the cell membrane also has a potential of ~-40 mV vs. the extracellular space, TPP cations accumulate ~5-fold in the cytosol (Figure 5.2).

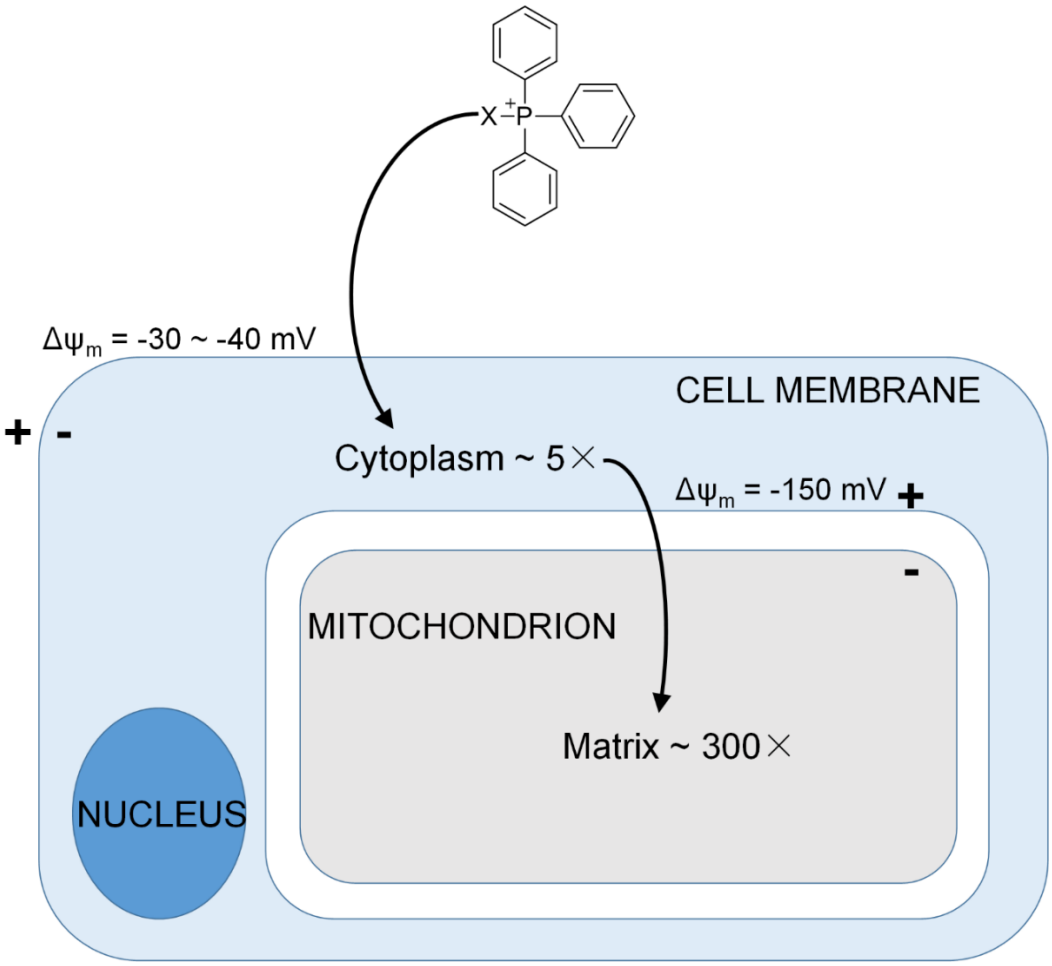

Figure 5.2 Structure of TPP and its accumulation in cells and mitochondria.

TPP cations have been demonstrated to be a powerful platform for targeting mitochondria. By conjugating various useful molecules to the cations, the use of TPP to facilitate the delivery of antioxidants is well established.[138,139] Besides, TPP based thiol probes, superoxide peroxides and GFP are also reported to be efficiently feasible and some of them have been even commercialised.

Therefore, in order to introduce our nanosensors into the mitochondria and measure the redox potentials in the matrix, a thiol moiety was grafted to the TPP, enabling the conjugation of GNP to the cations. The modified molecule (Figure 5.3) was synthesised by Patrick Thomson and it was named SBTPP. With the thiol moiety, SBTPP can be chemically adsorbed onto the GNP surface and the long carbon bridge connecting TPP to the GNP should also increase the uptake rate as well.

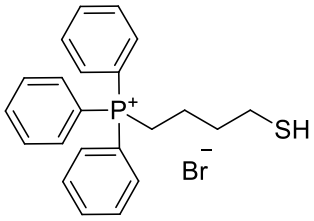

Figure 5.3 Structure of 4-sulfanylbutyltriphenylphosphanium bromide (SBTPP)

Since mitochondria only range from 500 to 1000 nm in diameter which is greatly smaller than the cells, NR with a 20 nm diameter and NC with a 30 nm diameter were used for mitochondrial delivery rather than NS (150 nm).

5.3 Intracellular mitochondrial nanosensor delivery

Since SBTPP is soluble in water, NC and NR were functionalised with 0.1 mmol/l SBTPP in PBS with 1% (W/V) CTAB for 24 hours. And then the functionalised NC

and NR were washed three times with PBS with 1% (W/V) CTAB to remove excess SBTPP. UV-Vis was recorded to demonstrate the success of functionalisation. A slight red shift was seen in the spectra which proved the successful coating of SBTPP on the surface of GNP. (Figure 5.4) Immediately before adding into the cell culture media, functionalised SBTPP were washed with PBS to remove the toxic CTAB. Following the same protocol for cytosolic nanosensor delivery, cells were incubated with SBTPP functionalised NR and NC overnight in CS-free media. TEMs showed that NR and NC were taken up by the cells (Figure 5.4). No nanosensor was spotted in the mitochondria. Besides, it is worth noting that almost all the NR and NC ended up within some structures which were not observed before. By comparing the TEM image with images of cellular compartments, these structures were believed to be lysosomes, which act as the waste disposal system of the cell by digesting unwanted materials both from outside of the cell and obsolete components inside the cell and breaking them down with lysosomal enzymes. This suggested that SBTPP-functionalised NR and NC were recognised as obsolete materials by the cell, or NR and NC were able to enter the mitochondria but killed them and were then swallowed by lysosomes, with dead mitochondria. In some TEM images, some suspicious structures similar to dead mitochondria were discovered within lysosomes.

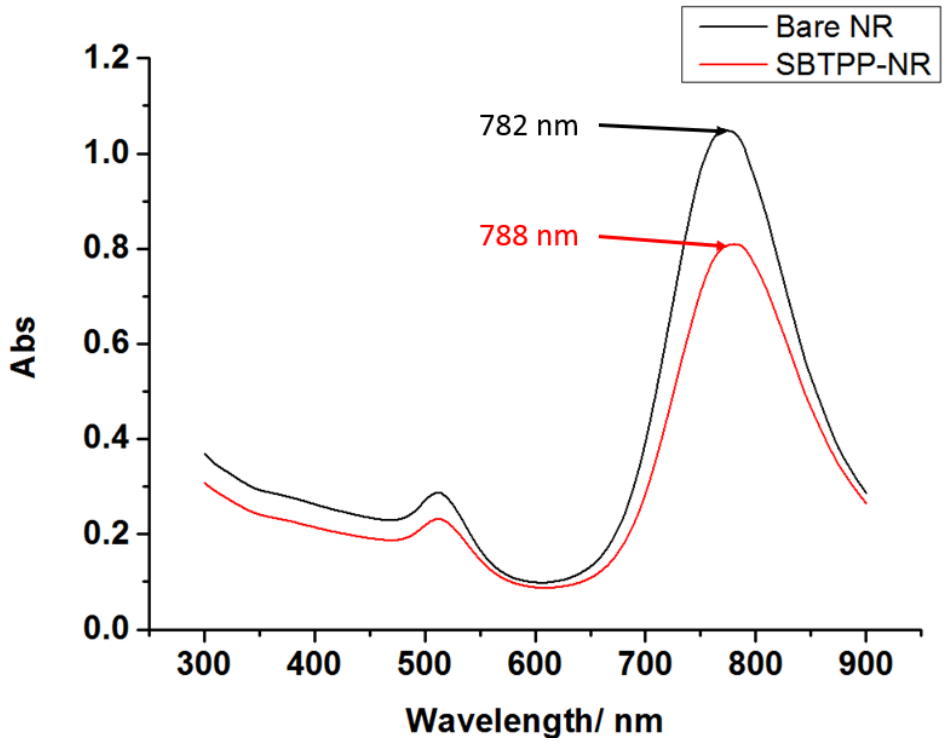

Figure 5.4 UV-Vis spectra of bare NC and functionalised SBTPP-NC

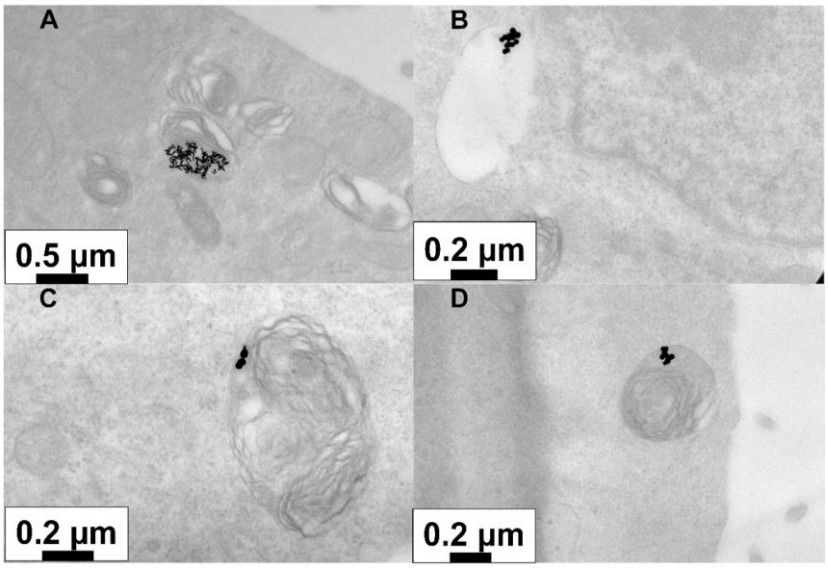

Figure 5.5 SBTPP functionalised GNP in cells. A: SBTPP functionalised NR in cells. B, C, D: SBTPP functionalised NC in cells.

Although GNP have been widely demonstrated to be able to enter cells through the plasma membrane, the mechanism is still a matter of debate, and uptake also reportedly depends on the shape, size and surface properties of the GNP as well as different cell lines. Therefore, using live cells would bring added uncertainties in targeting mitochondria as the TEM results above show. Isolated mitochondria offered an alternative for focusing the research and also avoiding extra effects introduced from living cells.

5.4 Mitochondrial isolation

Isolated mitochondria were introduced more than a half century ago by Chance & Williams (1956)[140] and have led to various crucial discoveries in mitochondrial biology, including the chemiosmotic theory of oxidative phosphorylation[141] and elucidation of the TCA cycle[142].

2×10^7 A549 cells were required to produce enough isolated mitochondria for the study of mitochondrial delivery. The mechanical method was used to rupture the cell suspension using a Dounce homogeniser, which consists of a glass pestle that is manually driven into a glass vessel. The degree of homogenisation is controlled by the clearance between the pestle and walls of the glass vessel, the rotational speed of the pestle, and the number of compression strokes made. For A549 cells, 50 strokes were enough to result in 80% lysis. The cell lysis efficiency was checked by spotting 5 µl of cell lysate onto a glass slide, adding a coverslip and viewing under the microscope. The result was compared with 5 µl of non-lysed cells. Since the localised heating occurring during the homogenisation could lead to protein denaturation and aggregation, it was essential to pre-chill the homogeniser and keep

samples on ice at all times. In addition, protease inhibitors were added to all samples prior to lysis to protect proteins from proteolysis during cells homogenisation

After the lysis of cells, differential centrifugation was applied to separate the mitochondria. Differential centrifugation comprised a two-step centrifugation carried out at low and high speeds consecutively. The low-speed centrifugation was usually carried out at 700*g* for 10 min and the subsequent high-speed centrifugation at 12,000*g* for 15 min. The low-speed centrifugation was necessary to remove intact cells, cellular debris and nuclei. The supernatant obtained from the low-speed centrifugation underwent a subsequent high-speed centrifugation to sediment intact mitochondria. Both of the centrifugation steps were performed at 4℃ to avoid localised heating which could damage the mitochondria. The resultant mitochondrial pellet was suspended in 300 µl of MAITE medium and stored on ice.

5.5 Concentration Determination (Bicinchoninic acid assay)

For downstream experiments, the concentration of isolated mitochondria must be determined. Since the number of mitochondria is not easy to count, the protein concentration of the mitochondrial suspension is instead measured. The BCA Assay is a colorimetric assay for the quantitation of total protein in a solution.[143] The total protein concentration is exhibited by a colour change of the sample solution from green to purple in proportion to protein concentration.

This method combines the well-known reduction of Cu^{2+} to Cu^{+} by proteins in an alkaline medium (the biuret reaction) with the highly sensitive and selective colorimetric detection of the cuprous cation (Cu^{+}) using a unique reagent containing

bicinchoninic acid. The purple-coloured reaction product of this assay is formed by the chelation of two molecules of BCA with one cuprous ion. This water-soluble complex exhibits a strong absorbance at 562 nm that is nearly linear with increasing protein concentrations over a broad working range (20-2,000 μg/ml). The BCA method is not a true end-point method; that is, the final colour continues to develop. However, following incubation, the rate of continued colour development is sufficiently slow to allow large numbers of samples to be assayed together.

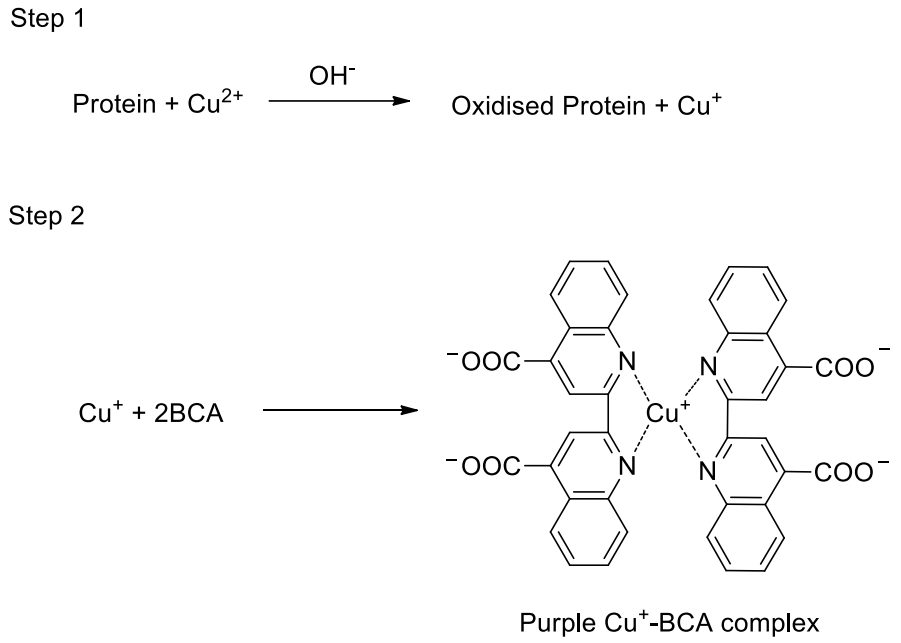

Figure 5.6 The formation of purple-coloured Cu^{+1} complex of BCA assay

Bovine serum albumin (BSA) was used as a standard to generate the standard curve. A set of BSA solutions, spanning 0 to 2000 μg/ml, were prepared and reacted with BCA assay reagent. After 30 min of incubation at 37 ℃, the absorbance of the resultant purple solutions were measured at 562 nm on a plate reader. By plotting the absorbance values against their corresponding BSA concentrations, the standard curve was generated for the quantification of the concentration of isolated

mitochondria. Figure 5.7 shows a standard curve of the BCA assay. The absorbance of the isolated mitochondria, processed along with these standard BSA solutions, was 0.184. Thus, based on that curve, the protein concentration of the mitochondria was 406 μg/ml.

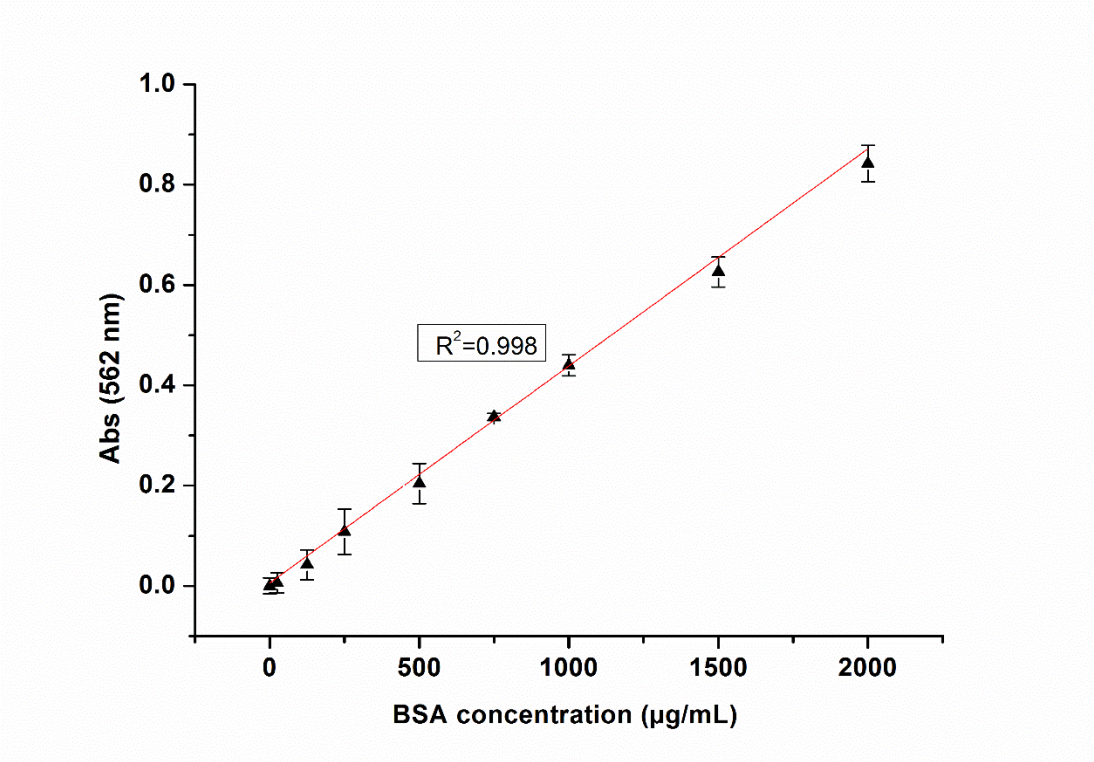

Figure 5.7 Standard curve of the BCA assay. Error bars represent the standard deviation of 3 replicates.

5.6 Viability assay of isolated mitochondria

The MTT assay is one of the most commonly used assays to measure cellular viability in living cells. It is based on the reduction of MTT by active mitochondria. In order to find the optimal conditions for storing the isolated mitochondria and also to screen for the potential toxicity of nanoparticles to mitochondria, the MTT assay for isolated mitochondria was developed.

Unlike in living cells, which can provide sufficient substrates for the reduction of MTT, isolated mitochondria are in a solution without reducing equivalents. Hence, succinate was added to the mitochondria suspension as a substrate to support the MTT reduction. After trials with a set of mitochondrial samples with different concentrations, 50 μg/ml was found to be enough to produce strong signals. Before incubating on ice for two hours, MTT was added into the solution at a final concentration of 1 mg/ml. Figure 5.8 shows the results of the MTT assay on isolated mitochondria under different experimental conditions.

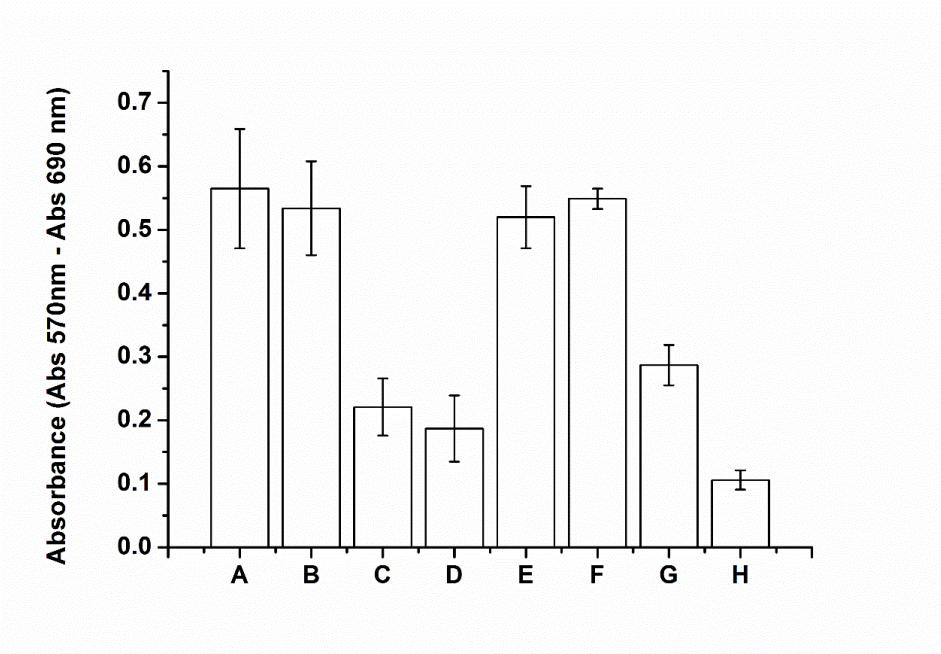

Figure 5.8 MTT assay results of isolated mitochondria under different experimental conditions. A: Untreated isolated mitochondria; B: Isolated mitochondria stored in MAITE medium on ice for 16 h; C: Isolated mitochondria stored in MAITE medium at r.t. for 16 h; D: Isolated mitochondria stored in MAITE medium in a humidified incubator of 5% CO_2 at 37 ℃ for 16 h; E: Isolated mitochondria treated with 100 fM SBTPP-NC on ice for 12 h; F: Isolated mitochondria treated with 100 fM SBTPP-NR on ice for 12 h; G: Untreated cells as a control; H: Lysed isolated mitochondria.

From Figure 5.8, it can be seen that isolated mitochondria kept on ice for over 16 hours did not show any difference in absorbance compared to the control sample, which was subject to the MTT assay immediately after being isolated. The MTT assay results also indicate that both storing the isolated mitochondria at r.t. or in the incubator with 5% CO_2 at 37 ℃ could lead to a significant decrease in their viability. Therefore, in order to remain healthy and active, the mitochondria must be kept on ice immediately after isolation from cells. In addition, it is worth noting that incubating the isolated mitochondria with 100 fM SBTPP-functionalised NR or NC for 12 hours on ice was demonstrated to be non-toxic and the lysed mitochondria only showed a very weak MTT response.

5.7 TEM

Since the ultimate goal was to target the mitochondria using SBTPP-functionalised NR or NC, TEM was employed to investigate the delivery of nanoparticles. However, the membrane structure of isolated mitochondria is very fragile without the protection of the cytoplasm membrane. Almost all the mitochondria ruptured during the sample preparation process and only mitochondrial debris was found in these TEM images. As such, other less destructive techniques are required for the research of isolated mitochondria.

5.8 Conclusion

In this chapter, although the attempt to target mitochondria requires more investigation, it is very exciting to see that a protocol for isolating mitochondria and keeping them healthy has been generated.

Chapter 6 Conclusions and future works

The overall aims of my project were to:

- Synthesise and characterise potential sensitive molecules to cover a range spanning from cellular hypoxia through oxidative stress
- Apply suitable nanosensors to quantify intracellular hypoxia in a reversible way and measure the potential value as a function of intracellular pH.

A novel approach to monitoring IRP has been presented in this thesis. Comparing to most widely used techniques, for example, Tietze's assay and roGFPs, it offers superior advantages on accuracy as well as ease of use. Although Tietze's assay is cheap and simple to perform, the requirement of cell lysis limits its use in live cells. It is also prone to inaccuracy causing by the oxidation of GSH to GSSG by air. Even the cutting edge technique, roGFPs, has some significant drawbacks. roGFPs must be subcloned into the cells of interest, which is cumbersome and very time-consuming. This technique also operates in a very limited window and has very little scope of expansion.

In this project, a set of small molecule probes have been synthesised and characterised. The SERS-based nanosensor shows oxidation state dependent changes in the Raman fingerprint since the vibrational modes of the oxidized and reduced species are distinct. These changes can be quantifiably linked with the local redox potentials to generate the calibration curve, determined by SERS spectroelectrochemistry. The ratiometric nature of our nanosensor means that the measurement of redox potential is independent of the intensity of the SERS signal – this means that there is no need to correct for the number of sensors in the focal volume or for the laser power. The mid-point potentials of these curves also showed

to correlate well with their half-wave potentials, obtained independently with CV. And the calibration curves indicated that these probes joined to cover a window ranging from hypoxia to cellular oxidative stress.

TEM demonstrated that nanosensors can be selectively taken up by the cells and translocated to the cytoplasm under the right conditions. Since intracellular redox potential is pH dependent, the intracellular pH was first measured and used to correct the potential. Intracellular redox potential measurements of resting cells using both AQ-NS and our previously reported NQ-NS are in good agreement, demonstrating that the measurements based on the practical calibration curve are reliable. When AQ-NS was used to monitor the redox potential of cells in which hypoxia was induced by cobalt chloride it was observed that the redox potential became progressively more reductive – this agrees with the observation that hypoxia induces a metabolic switch which leads to an increase in the production of NADH and NADPH (the primary electron donors of the cell).

In general, the aims of this work have been achieved and a novel quantitative approach to probe the intracellular hypoxia in a reversible way and also in real time. It provides a reliable and effective method to enable researchers to develop a better understanding of how the dysregulation of cellular redox potential plays a role in hypoxia and hypoxia-associated diseases. In addition, the unprecedented potential window covered by this technique can further the understanding of the multitude of redox systems in cells and how they interact with each other.

There are still many possibilities to explore. For example:

1) Measure the redox state of the nucleus, mitochondria or even other cellular compartments.
2) Quantify the normal 'low-oxygen' hypoxia and compare the obtained redox potential with that of chemically induced hypoxia.

3) In terms of the significant role of the hypoxia in tumour progression, this measuring system can be applied to quantitatively investigate the effect of drugs which can be used to tune the hypoxia.

4) Relate the redox potential range to the different phases in cellular cycle.

5) Combine different probe molecules to form omnipotent nanosensors which are capable of reporting on the intracellular potential from hypoxia to oxidative stress at the same time.

6) In order to improve the accuracy of SERS nanosensors, it is necessary to record the SERS spectra of each nanosensor at different pHs.

7) The surface charge of functionalised nanosensors should also be investigated.

References

1 D. Trachootham, W. Lu, M. a Ogasawara, R.-D. V. Nilsa and P. Huang, *Antioxid. Redox Signal.*, 2008, **10**, 1343–74.

2 J. Nakamura, H. Nakamura, K. Yodoi, *Annu. Rev. …*, 1997, **15**, 351–369.

3 H. Kamata and H. Hirata, *Cell. Signal.*, 1999, **11**, 1–14.

4 S. G. Menon and P. C. Goswami, *Oncogene*, 2007, **26**, 1101–9.

5 C. E. Paulsen and K. S. Carroll, *ACS Chem. Biol.*, 2010, **5**, 47–62.

6 V. Mallikarjun, D. J. Clarke and C. J. Campbell, *Free Radic. Biol. Med.*, 2012, **53**, 280–8.

7 J. Smith, E. Ladi, M. Mayer-Proschel and M. Noble, *Proc. Natl. Acad. Sci. U. S. A.*, 2000, **97**, 10032–7.

8 E. H. Sarsour, M. G. Kumar, L. Chaudhuri, A. L. Kalen and P. C. Goswami, *Antioxid. Redox Signal.*, 2009, **11**, 2985–3011.

9 Y. L. Siow, L. Sarna and K. O, *Food Res. Int.*, 2011, **44**, 2409–2417.

10 Y.-M. Go and D. P. Jones, *Free Radic. Biol. Med.*, 2011, **50**, 495–509.

11 F. Q. Schafer and G. R. Buettner, *Free Radic. Biol. Med.*, 2001, **30**, 1191–212.

12 W. R. Wilson and M. P. Hay, *Nat. Rev. Cancer*, 2011, **11**, 393–410.

13 M. Kunz and S. M. Ibrahim, *Mol. Cancer*, 2003, **2**, 23.

14 P. Vaupel and A. Mayer, *Cancer Metastasis Rev.*, 2007, **26**, 225–39.

15 T. L. Clanton, *J. Appl. Physiol.*, 2007, **102**, 2379–88.

16 M. Bhatia and T. Karlenius, *Carcinog. …*, 2013.

17 J. F. Garvey, C. T. Taylor and W. T. McNicholas, *Eur. Respir. J. Off. J. Eur. Soc. Clin. Respir. Physiol.*, 2009, **33**, 1195–205.

18 Q. Gao and M. Wolin, *Am. J. Physiol. …*, 2008, **10595**, 978–989.

19 T. D. Oberley, J. L. Schultz, N. Li and L. W. Oberley, *Free Radic. Biol. Med.*, 1995, **19**, 53–65.

20 G. B. Waypa, J. D. Marks, R. Guzy, P. T. Mungai, J. Schriewer, D. Dokic and P. T. Schumacker, *Circ. Res.*, 2010, **106**, 526–35.

21 W. W. Wheaton and N. S. Chandel, *Am. J. Physiol. Cell Physiol.*, 2011, **300**, C385–93.

22 Q. Ke and M. Costa, *Mol. Pharmacol.*, 2006, **70**, 1469–1480.

23 J. E. Ziello, I. S. Jovin and Y. Huang, *Yale J. Biol. Med.*, 2007, **80**, 51–60.

24 P. H. Maxwell, *Exp. Physiol.*, 2005, **90**, 791–7.

25 J. Pouysségur and F. Mechta-Grigoriou, *Biol. Chem.*, 2006, **387**, 1337–46.

26 R. Connett and C. Honig, *J Appl …*, 1990, **68**, 833–842.

27 K. Gilany and M. Vafakhah, *J. Paramed. Sci.*, 2010, **1**, 43–60.

28 A. J. Giaccia, M. C. Simon and R. Johnson, *Genes Dev.*, 2004, **18**, 2183–94.

29 G. B. Waypa and P. T. Schumacker, *J. Appl. Physiol.*, 2005, **98**, 404–14.

30 J. Fan, H. Cai, S. Yang, L. Yan and W. Tan, *Comp. Biochem. Physiol. B. Biochem. Mol. Biol.*, 2008, **151**, 153–8.

31 C. Oh, Y. Dong, C. Harman, H. E. Mighty, J. Kopelman and L. P. Thompson, *Early Hum. Dev.*, 2008, **84**, 121–7.

32 S. C. Rogers, A. Said, D. Corcuera, D. McLaughlin, P. Kell and A. Doctor, *FASEB J.*, 2009, **23**, 3159–70.

33 K. D. Mansfield, M. C. Simon and B. Keith, *J. Appl. Physiol.*, 2004, **97**, 1358–66.

34 K. Ruan, G. Song and G. Ouyang, *J. Cell. Biochem.*, 2009, **107**, 1053–62.

35 J. S. Fang, R. D. Gillies and R. a Gatenby, *Semin. Cancer Biol.*, 2008, **18**, 330–7.

36 R. a Gatenby, K. Smallbone, P. K. Maini, F. Rose, J. Averill, R. B. Nagle, L. Worrall and R. J. Gillies, *Br. J. Cancer*, 2007, **97**, 646–53.

37 J. Kim, P. Gao and C. V Dang, *Cancer Metastasis Rev.*, 2007, **26**, 291–8.

38 G. L. Semenza, *N. Engl. J. Med.*, 2011, **365**, 537–47.

39 N. Masson and P. J. Ratcliffe, *Cancer Metab.*, 2014, **2**, 3.

40 J. M. Brown, *Methods Enzymol.*, 2007, **435**, 297–321.

41 J. E. Conour, W. V Graham and H. R. Gaskins, *Physiol. Genomics*, 2004, **18**, 196–205.

42 M. Frisard and E. Ravussin, *Endocrine*, 2006, **29**, 27–32.

43 B. Halliwell, *Free radicals and other reactive species in disease*, 2005, vol. 27.

44 I. Fridovich, *Annu. Rev. Biochem.*, 1995, **64**, 97–112.

45 M. Giorgio, M. Trinei, E. Migliaccio and P. G. Pelicci, *Nat. Rev. Mol. Cell Biol.*, 2007, **8**, 722–8.

46 B. Halliwell and J. M. C. Gutteridgeb, *FEBS*, 1992, **307**, 108–112.

47 C. B äärnhielm, I. Sk ånberg and K. Borg, *Xenobiotica*, 1984.

48 V. J. Thannickal and B. L. Fanburg, *Am. J. Physiol. Lung Cell. Mol. Physiol.*, 2000, **279**, L1005–28.

49 B. Babior, *Blood*, 1999, **93**, 1464–1476.

50 M. C. Mart ínez and R. Andriantsitohaina, *Antioxid. Redox Signal.*, 2009, **11**, 669–702.

51 P. Klatt, E. P. Molina, M. Garci, J. A. Ba, C. A. Padilla, E. Marti and S. Lamas, *FASEB J*, 1999, **13**, 1481–1490.

52 W. C. Barrett, J. P. DeGnore, Y.-F. Keng, Z.-Y. Zhang, M. B. Yim and P. B. Chock, *J. Biol. Chem.*, 1999, **274**, 34543–34546.

53 D. Lando, *J. Biol. Chem.*, 2000, **275**, 4618–4627.

54 K. Hirota, M. Murata, Y. Sachi, H. Nakamura, J. Takeuchi, K. Mori and J. Yodoi, *J. Biol. Chem.*, 1999, **274**, 27891–27897.

55 K. Iwai, S. K. Drake, N. B. Wehr, a M. Weissman, T. LaVaute, N. Minato, R. D. Klausner, R. L. Levine and T. a Rouault, *Proc. Natl. Acad. Sci. U. S. A.*, 1998, **95**, 4924–8.

56 D. a Dickinson and H. J. Forman, *Biochem. Pharmacol.*, 2002, **64**, 1019–26.

57 H. L. Martin and P. Teismann, *FASEB J.*, 2009, **23**, 3263–72.

58 A. Meister, *J Biol Chem*, 1988, **263**, 17205–17208.

59 A. Pastore, G. Federici, E. Bertini and F. Piemonte, *Clin. Chim. Acta*, 2003, **333**, 19–39.

60 J. Nordberg and E. Arnér, *Free Radic. Biol. Med.*, 2001, **31**, 1287–1312.

61 J.-F. Collet and J. Messens, *Antioxid. Redox Signal.*, 2010, **13**, 1205–16.

62 a Holmgren, *Structure*, 1995, **3**, 239–43.

63 E. S. Arnér and a Holmgren, *Eur. J. Biochem.*, 2000, **267**, 6102–9.

64 F. Wientjes and A. Segal, *Semin. Cell Biol.*, 1995, **6**, 357–365.

65 S. Li, T. Yan, J. Yang, T. Oberley and L. Oberley, *Cancer Res.*, 2000, 3927–3939.

66 C. G. Fraga, P. a Motchnik, M. K. Shigenaga, H. J. Helbock, R. a Jacob and B. N. Ames, *Proc. Natl. Acad. Sci. U. S. A.*, 1991, **88**, 11003–6.

67 R. E. Beyer, *J. Bioenerg. Biomembr.*, 1994, **26**, 349–58.

68 M. Traber and L. Packer, *Am. J. Clin. Nutr.*, 1995, **62**, 1510S–9S.

69 F. Tietze, *Anal. Biochem.*, 1969, **27**, 502–522.

70 C. T. Dooley, T. M. Dore, G. T. Hanson, W. C. Jackson, S. J. Remington and R. Y. Tsien, *J. Biol. Chem.*, 2004, **279**, 22284–93.

71 G. T. Hanson, R. Aggeler, D. Oglesbee, M. Cannon, R. a Capaldi, R. Y. Tsien and S. J. Remington, *J. Biol. Chem.*, 2004, **279**, 13044–53.

72 A. Gomes, E. Fernandes and J. L. F. C. Lima, *J. Biochem. Biophys. Methods*, 2005, **65**, 45–80.

73 O. Myhre, J. M. Andersen, H. Aarnes and F. Fonnum, *Biochem. Pharmacol.*, 2003, **65**, 1575–1582.

74 K. a Krohn, J. M. Link and R. P. Mason, *J. Nucl. Med.*, 2008, **49 Suppl 2**, 129S–48S.

75 I. Rahman, A. Kode and S. K. Biswas, *Nat. Protoc.*, 2006, **1**, 3159–65.

76 R. Y. Tsien, *Annu. Rev. Biochem.*, 1998, **67**, 509–44.

77 K. a Krohn, J. M. Link and R. P. Mason, *J. Nucl. Med.*, 2008, **49 Suppl 2**, 129S–48S.

78 C. a R. Auchinvole, P. Richardson, C. McGuinnes, V. Mallikarjun, K. Donaldson, H. McNab and C. J. Campbell, *ACS Nano*, 2012, **6**, 888–96.

79 C. Raman and K. Krishnan, *Nature*, 1928, **121**, 501–502.

80 J. Ferraro, *Introductory raman spectroscopy*, Elsevier, 1994.

81 J. Ferraro, K. Nakamoto and C. W. Brown, *Introductory Raman Spectroscopy*, Elsevier, Second Edi., 2003.

82 M. Fleischmann, P. J. Hendra and A. J. McQuillan, *Chem. Phys. Lett.*, 1974, **26**, 163–166.

83 J. a. Dieringer, A. D. McFarland, N. C. Shah, D. a. Stuart, A. V. Whitney, C. R. Yonzon, M. a. Young, X. Zhang and R. P. Van Duyne, *Faraday Discuss.*, 2006, **132**, 9.

84 P. L. Stiles, J. a Dieringer, N. C. Shah and R. P. Van Duyne, *Annu. Rev. Anal. Chem. (Palo Alto. Calif).*, 2008, **1**, 601–26.

85 S. Schlücker, *Angew. Chem. Int. Ed. Engl.*, 2014, **53**, 4756–95.

86 W. Stöber, A. Fink and E. Bohn, *J. Colloid Interface Sci.*, 1968, **26**, 62–69.

87 S. Kalele, S. W. Gosavi, J. Urban and S. K. Kulkarni, *Curr. Sci.*, 2006, **91**, 1038–1052.

88 R. Shukla, V. Bansal, M. Chaudhary, A. Basu, R. R. Bhonde and M. Sastry, *Langmuir*, 2005, **21**, 10644–10654.

89 J. Kneipp, H. Kneipp, A. Rajadurai, R. W. Redmond and K. Kneipp, *J. Raman Spectrosc.*, 2009, **40**, 1–5.

90 W. Cai, T. Gao, H. Hong and J. Sun, *Nanotechnol. Sci. Appl.*, 2008, **2008**, 17–32.

91 M. Nagata, M. Kondo, Y. Suemori, T. Ochiai, T. Dewa, T. Ohtsuka and M. Nango, *Colloids Surf. B. Biointerfaces*, 2008, **64**, 16–21.

92 M. Amblard, J.-A. Fehrentz, J. Martinez and G. Subra, *Mol. Biotechnol.*, 2006, **33**, 239–54.

93 J. Heinze, *Angew. Chem. Int. Ed. Engl.*, 1984, **23**, 831–918.

94 J. L. Stickney, M. P. Soriaga, A. T. Hubbard and S. E. Anderson, *J. Electroanal. Chem. Interfacial Electrochem.*, 1981, **125**, 73–88.

95 K. G. Symms and M. R. Juchau, *Biochem. Pharmacol.*, 1972, **21**, 2519–27.

96 W. Sun, Q. Dai, J. G. Worden and Q. Huo, *J. Phys. Chem. B*, 2005, **109**, 20854–7.

97 P. Ghosh, G. Han, M. De, C. K. Kim and V. M. Rotello, *Adv. Drug Deliv. Rev.*, 2008, **60**, 1307–15.

98 X. Huang and M. a. El-Sayed, *J. Adv. Res.*, 2010, **1**, 13–28.

99 P. C. Chen, S. C. Mwakwari and A. K. Oyelere, *Nanotechnol. Sci. Appl.*, 2008, **1**, 45–65.

100 L. Dykman and N. Khlebtsov, *Chem. Soc. Rev.*, 2012, **41**, 2256–82.

101 N. Li, P. Zhao and D. Astruc, *Angew. Chem. Int. Ed. Engl.*, 2014, **53**, 1756–89.

102 A. M. Alkilany, P. K. Nagaria, C. R. Hexel, T. J. Shaw, C. J. Murphy and M. D. Wyatt, *Small*, 2009, **5**, 701–8.

103 A. M. Alkilany and C. J. Murphy, *J. Nanopart. Res.*, 2010, **12**, 2313–2333.

104 W. Sigle, *Annu. Rev. Mater. Res.*, 2005, **35**, 239–314.

105 T. Mosmann, *J. Immunol. Methods*, 1983, **65**, 55–63.

106 S. W. Bishnoi, C. J. Rozell, C. S. Levin, M. K. Gheith, B. R. Johnson, D. H. Johnson and N. J. Halas, *Nano Lett.*, 2006, **6**, 1687–92.

107 J. Kneipp, H. Kneipp, B. Wittig and K. Kneipp, *Nano Lett.*, 2007, **7**, 2819–23.

108 M. Kneen, J. Farinas, Y. Li and a S. Verkman, *Biophys. J.*, 1998, **74**, 1591–9.

109 J. Han and K. Burgess, *Chem. Rev.*, 2010, **110**, 2709–28.

110 P. Ozkan and R. Mutharasan, *Biochim. Biophys. Acta*, 2002, **1572**, 143–8.

111 H. Schwartz, I. Tauber and T. William, 1988, **186**, 183–186.

112 S. Olsnes, T. I. Tønnessen and K. Sandvig, *J. Cell Biol.*, 1986, **102**, 967–71.

113 I. H. Madshus, *Biochem. J.*, 1988, **250**, 1–8.

114 W. F. Boron, *Adv. Physiol. Educ.*, 2004, **28**, 160–79.

115 J. R. Casey, S. Grinstein and J. Orlowski, *Nat. Rev. Mol. Cell Biol.*, 2010, **11**, 50–61.

116 J. Yuen and N. Shah, *Anal. …*, 2010, **82**, 8382–8385.

117 K. Ma, J. Yuen and N. Shah, *Anal. …*, 2011, **83**, 9146–9152.

118 D. Craig, S. McAughtrie and J. Simpson, *Anal. …*, 2014, **86**, 4775–4782.

119 S. Shanmukh, L. Jones, J. Driskell, Y. Zhao, R. Dluhy and R. a Tripp, *Nano Lett.*, 2006, **6**, 2630–6.

120 K. S. Kim, V. Rajagopal, C. Gonsalves, C. Johnson and V. K. Kalra, *J. Immunol.*, 2006, **177**, 7211–7224.

121 Y. Yuan, G. Hilliard, T. Ferguson and D. E. Millhorn, *J. Biol. Chem.*, 2003, **278**, 15911–6.

122 a Vengellur and J. J. LaPres, *Toxicol. Sci.*, 2004, **82**, 638–46.

123 K. Salnikow, T. Davidson and M. Costa, *Environ. Health Perspect.*, 2002, **110 Suppl** , 831–4.

124 M. Guo, L.-P. Song, Y. Jiang, W. Liu, Y. Yu and G.-Q. Chen, *Apoptosis*, 2006, **11**, 67–77.

125 S. Betigeri, A. Thakur and K. Raghavan, *Pharm. Res.*, 2005, **22**, 310–317.

126 Y. Sato, S. Kamo, T. Takahashi and Y. Suzuki, *Biochemistry*, 1995, **34**, 8940–9.

127 Z. Li, X. Li, X. Gao, Y. Zhang and W. Shi, *Anal. Chem.*, 2013, **85**, 3926–3932.

128 J. Kang and S. Pervaiz, *Biochem. Res. Int.*, 2012, **2012**, 896751.

129 P. a Kramer, S. Ravi, B. Chacko, M. S. Johnson and V. M. Darley-Usmar, *Redox Biol.*, 2014, **2**, 206–10.

130 D. C. Wallace, *Nat. Rev. Cancer*, 2012, **12**, 685–98.

131 L. Ernster and G. Schatz, *J. Cell Biol.*, 1981, **91**, 227s–255s.

132 D. D. Newmeyer and S. Ferguson-Miller, *Cell*, 2003, **112**, 481–90.

133 J. Hu, L. Dong and C. E. Outten, *J. Biol. Chem.*, 2008, **283**, 29126–34.

134 A. Bratic and N. Larsson, *J. Clin. Invest.*, 2013, **123**, 951–57.

135 L. a Sena and N. S. Chandel, *Mol. Cell*, 2012, **48**, 158–67.

136 M. P. Murphy, *Biochem. J.*, 2009, **417**, 1–13.

137 M. P. Murphy and R. a J. Smith, *Annu. Rev. Pharmacol. Toxicol.*, 2007, **47**, 629–56.

138 G. F. Kelso, C. M. Porteous, C. V Coulter, G. Hughes, W. K. Porteous, E. C. Ledgerwood, R. a Smith and M. P. Murphy, *J. Biol. Chem.*, 2001, **276**, 4588–96.

139 R. a J. Smith and M. P. Murphy, *Discov. Med.*, 2011, **11**, 106–14.

140 B. Chance and G. Williams, *J. Biol. Chem.*, 1956, **221**, 477–490.

141 P. Mitchell, *Nature*, 1961, **191**, 144–148.

142 G. R. Williams, *Can. J. Biochem.*, 1965, **43**, 603–15.

143 P. K. Smith, R. I. Krohn, G. T. Hermanson, a. K. Mallia, F. H. Gartner, M. D. Provenzano, E. K. Fujimoto, N. M. Goeke, B. J. Olson and D. C. Klenk, *Anal. Biochem.*, 1985, **150**, 76–85.